2013

KINETICS OF WEDGE-TEE JOINT FORMATION DURING BRAZING OF AN ALUMINUM ALLOY UNDER CONTROLLED ATMOSPHERE

Fangxiao Dong
University of Kentucky, fdo223@g.uky.edu

STUDENT AGREEMENT:

I represent that my thesis or dissertation and abstract are my original work. Proper attribution has been given to all outside sources. I understand that I am solely responsible for obtaining any needed copyright permissions. I have obtained and attached hereto needed written permission statements(s) from the owner(s) of each third-party copyrighted matter to be included in my work, allowing electronic distribution (if such use is not permitted by the fair use doctrine).

I hereby grant to The University of Kentucky and its agents the non-exclusive license to archive and make accessible my work in whole or in part in all forms of media, now or hereafter known. I agree that the document mentioned above may be made available immediately for worldwide access unless a preapproved embargo applies.

I retain all other ownership rights to the copyright of my work. I also retain the right to use in future works (such as articles or books) all or part of my work. I understand that I am free to register the copyright to my work.

REVIEW, APPROVAL AND ACCEPTANCE

The document mentioned above has been reviewed and accepted by the student's advisor, on behalf of the advisory committee, and by the Director of Graduate Studies (DGS), on behalf of the program; we verify that this is the final, approved version of the student's dissertation including all changes required by the advisory committee. The undersigned agree to abide by the statements above.

Fangxiao Dong, Student

Dr. Dusan P. Sekulic, Major Professor

Dr. James McDonough, Director of Graduate Studies

KINETICS OF WEDGE-TEE JOINT FORMATION DURING BRAZING OF AN ALUMINUM ALLOY UNDER CONTROLLED ATMOSPHERE

THESIS

A thesis submitted in partial fulfillment of the requirements for the degree of Master of Science in Mechanical Engineering in the College of Engineering at the University of Kentucky

By

Fangxiao Dong

Lexington, Kentucky

Director: Dr. Dusan P. Sekulic, Professor

Department of Mechanical Engineering

Lexington, Kentucky

2013

ABSTRACT OF THESIS

KINETICS OF WEDGE-TEE JOINT FORMATION DURING BRAZING OF AN ALUMINUM ALLOY UNDER CONTROLLED ATMOSPHERE

This work involves investigation of the kinetics data of a joint formation during aluminum alloy brazing. Data was generated by several groups of experiments conducted under conditions of a controlled oxygen level of the background brazing atmosphere. Generated data are examined to identify the phases of the joint formation and the time frame of its evolution. Specifically, the triple line kinetics data are analyzed to verify whether a power law between (1) the triple line of the molten metal preceding joint formation and (2) the formation time can be established for each formation phase. In addition, both initial and residual clad thicknesses on brazing sheets are studied to check phenomenologically an impact of silicon diffusion on joint formation. Formation shapes are also inspected in order to study if a 2-D configuration of joint formation is present. The kinetics data from different sets of experiments under adverse atmosphere conditions are compared to understand the impact of oxygen level on joint formation. This study is not necessarily aimed at building a mathematical model for T-Joint formation during brazing process, but intends to understand possible influential parameters on the development of the formation.

KEYWORDS: Aluminum Brazing, Kinetics, T-Joint, Background Atmosphere, Capillary Flow.

Fangxiao Dong

April 22, 2013

KINETICS OF WEDGE-TEE JOINT FORMATION DURING BRAZING OF AN ALUMINUM ALLOY UNDER CONTROLLED ATMOSPHERE

By

Fangxiao Dong

Dr. Dusan P. Sekulic
Director of Thesis

Dr. James M. McDonough
Director of Graduate Studies

April 22, 2013

DEDICATION

I DEDICATE MY THESIS TO MY FAMILY

.

ACKNOWLEDGEMENTS

First of all, I want to take this opportunity to sincerely thank my academic advisor Professor Dusan P. Sekulic for his guidance for my graduate study. Without his support, this research work would never have been completed.

In addition, I am grateful to my committee members: Drs. Kozo Saito and Haluk Karaca. I would like to thank all of you for your time and advice during the defense process.

I also want to thank all the members of the Department of Mechanical Engineering for the assistantship to support my study and living in the United States.

Last but not least, gratitude is also given to all my team members in our laboratory for their precious suggestions and help.

Table of Contents

LIST OF TABLES

LIST OF FIGURES

CHAPTER 1: INTRODUCTION

1.1 Background and Motivation

Aluminum alloys brazing has been playing a significantly important role in numerous applications for a long time, such as in aircraft applications and compact heat exchanger manufacturing.[1, 2] Key physics phenomenon involved in Aluminum brazing is a surface tension/capillary driven flow of microlayers of molten metal around the interface of two mating metals.[3] The liquid phase metal wets the surfaces of bonding metals and spreads on them due to capillary action and finally becomes solidified to form the joint. The detailed reviews of spreading phenomena and the dynamic aspects of capillary flow are avilable.[4- 6] In ref. 6, a theoretical model of a power law type, spreading distance ~ $t^{1/2}$, is proposed to describe the triple line location dependence on time. This relationship has been derived by balancing the capillary and viscous forces only.

Kinetics study of this flow family is crucial in manufacturing industry. For example, in the field of heat exchanger manufacturing, both the final shape and dimension of joint formation and the duration of the heating sequence of fin tubes being brazed in the furnace on a moving belt are the two of deciding parameters to determine the quality of joints and reduce probability of poor thermal contact resistance between fins and substrate surfaces. To ensure better mechanical integrity of a heat exchanger, all the joints must have well formed fillets. In recent years, a lot of attention has been given to kinetics phenomena during brazing, such as a study of a sessile drop molten metal spreading over complex substrates and capillary rise of liquids.[7, 8] However, most of the research of the so called T-Joint formation is mainly focused on its equilibrium state, not its evolution. Reference 9 offers a study of joint formation of a traditional and a novel fluxless brazing sheet under different background atmospheres.

This thesis summarizes the characteristics of T-Joint kinetics based on an experimental work involving molten aluminum alloy spreading over aluminum substrate.

1.2 Objectives

Objectives of the study summarized in this thesis are as follows:

- To conduct a literature review of related topics that are of importance to this thesis and to summarize the existing knowledge
- To present five groups of kinetics data of T-Joint formation from a fluxless substrate and over a non-clad vertical aluminum alloy mating surface under the wide range of oxygen levels including: 70ppm, 200ppm, 500ppm, 2,000ppm and 200,000ppm Oxygen, respectively
- To verify whether a power law exists between the joint triple line location and time
- To identify the distinct phases of a joint formation and the time frame of each so identified phase
- To validate if a 2D configuration of joint formation can be secured under given background atmosphere conditions
- To examine whether silicon diffusion has a sizable presence and/or an impact on joint formation in each group

In the subsequent chapters, these objectives will be further expanded.

This work has been conducted within a scope of the project titled “Reactive and non-reactive wetting of liquid metals on rough surfaces. Experiments and modeling”, Principal Investigator Prof. D.P. Sekulic, NSF – CBET Grant # 1235759.

1.3 Literature Review

To better understand the existing depth of knowledge about the kinetics of a wedge T-Joint formation (spreading into a "corner") during aluminum brazing over, in general, a reactive substrate, an extensive literature review has been performed. The remaining content of this chapter offers the review divided into several sections depending on the related topic.

1.3.1 Capillary Driven Wetting and Kinetics

Capillary action is the driving force in applications of a process involving wicking phenomena over rough/porous surfaces. In the study of Bico et al. concerning wicking of silicone oil over a micro-structured surface with regular micron-sized topographic alterations of a substrate formed by spikes composed of a silicon wafer and a sol-gel silicate coating[10], a Washburn type kinetics[6] model was well established except that an empirical parameter is required for executing a modeling. The same phenomenon was studied by Hay et al.[11] Wicking was treated as spreading over a surface featuring parallel channels. Washburn type kinetics results were also obtained. Ishino et al.[12] confirmed that wicking kinetics in a network of regularly distributed micropillars was strongly correlated to the ratio of pillar height to the pitch of the network. The work from Chen et al.[13] involved numerous structured surfaces with a series of uniformly distributed patterns of regular geometric shapes such as star and square pattern surfaces. Its kinetics results conformed to Washburn type kinetics model. In Ref.8, the wicking kinetics of five organic liquids with different surface tension to viscosity ratios[14] were studied during spreading over an intermetallic surface with locally non-uniform surface structure but homogeneously distributed over a vertical substrate. Since the Bond number associated with selected liquids was very small ($O(10^{-9})$), the influence of gravity was neglected in the subsequent model building. This modeling was focused on the rise of a liquid driven by the capillary force.

Assumptions were made for theoretically building the kinetics model. The influence of evaporation of the organic liquids is neglected due to the fact that the saturated liquid vapor atmosphere was in contact with the liquid phase. An infinitely large liquid source is assumed (compared to the liquid phase climbing through the roughness features of the surface). By invoking Darcy's law and the definition of velocity, an equation that correlates the rising triple line location of the liquid to (i) permeability, (ii) tortuosity, and (iii) dynamic viscosity of the rough surface is devised. A particular triangular cross section area of the V-shaped groove is assumed. Using the expressions[15] for cross section and capillary force for a V shaped groove and introducing the definition of the filling factor[7], the relationship relating moving front to time was derived. It was noted that the capillary rise of liquid over the studied complex surface follows a Washburn type model. Scaling time with the surface tension to viscosity ratios collapses data around a narrow domain. This means that the scaling of the time eliminates the fluid type effect on wicking, implying that all considered liquids penetrate the porous surface following the same governing law. This was associated with a constant filling factor.

Capillary action is also the dominant force for the molten metal clad spreading on the substrate and subsequent joining of the materials that are to be bonded. However, there is a significant difference between a low temperature and a high temperature capillary phenomena.[16] For example, molten filler metal spreading over substrate may interact with a substrate what may not be the case with silicon oil on a non-reactive substrate. This difference may also lead to a different time scale for kinetics[17]. In Ref.7, Wen et al. studied the capillary driven flow of molten Sn-Pb eutectic of a sessile drop over a Cu-Sn-based complex substrate that has microscallop-grain topography. The mathematical model for this spreading during a soldering process has been built. Relationship between spreading front and the evolution time has been performed. The kinetics data clearly indicate that the process of spreading can be divided into three stages:

1) The initial stage dominated by inertial forces which lasts very short [O(10^{-1} s)] for spreading over a flat nonreactive surface[18, 19].

2) The power-law stage. This is the main stage which covers a great portion of the spreading time [O(10^{0}-10^{1} s)].

3) Asymptotic stage featuring a diminishing slope due to a diminishing liquid source.

The model was built for power-law type of spreading stage, controlled by surface tension and viscosity. The complex scallop shaped surface was simplified and represented as a collection of hexagonal elements which formed a surface roughness with triangular-shaped grooves and merging zones. Several assumptions were made before building the theoretical model, including constant liquid phase properties and negligible gravity impact. Also, chemical reactions during spreading were considered as negligible. Using the continuity equation and the Darcy's law for a differential control volume[20, 21] gives a relation between the location of triple line and the spreading time. The relationship is of a Washburn type. The instantaneous locations of the spreading front are directly proportional to the square root of the spreading time. This model agrees well with the empirical data, with a deviation in the range of 5-15%.

Sekulic[22] used scaling analysis on governing equations for reactive filler metal micro layer flow in a sessile drop configuration before the formation of an equilibrium membrane of the free surface during aluminum brazing to find a series of dimensionless parameters that control this process. Five governing equations are identified for this analytical model, involving 3-D configuration. These equations include: (i) continuity (ii) momentum (iii) energy (iv) concentration of a single species, and (v) entropy. These equations are further simplified based on empirical evidence (i.e., two-dimensional features, constant thermo physical properties, no gravity influence etc.) After that, boundary and initial conditions were imposed on those simplified governing equations including temperature and velocity at top of the substrate (bottom of the clad) and the involvement of balancing normal and tangential stress components[23] at the free surface. Subsequently, a number of relevant scales are selected for length, velocity and time. Finally, rewriting the simplified governing equations with selected associated scales resulted in an extraction of the prominent dimensionless numbers for the process. These include Reynolds number, Prandtl number, Schmidt number, Bond number, Capillary number and Reaction number. [Ref. 22]

Many industrial processes are based on the control of the flow and spreading of high temperature liquids[24-26]. However, high-temperature spreading is a complex phenomena[27]. So, this research has to contribute to an insight into the physics of the process, capillary evolution of the liquid metal interface.

The difficulty in modeling of this process lies in the phenomena that take place at nano or atomic scale in the vicinity of the triple junction with macroscopic phenomena such as the movement of the liquid front[27]. Atomic theory and experimental research along with computer simulation is clearly benefiting from analysis and experiments conducted at the macro scale. Hence, a connection can be established to identify the similarities while pointing out the fundamental differences. A key aspect of the analysis is to divide the process into constituent steps and understand the relative kinetics of the movement of the liquid front and the accompanying phenomena such as adsorption, ridging, dissolution and compound formation in order to define the instantaneous structure of the triple junction. By doing this, a general theory can be modeled concerning spreading kinetics under high temperature condition[27]. The goal is to formulate a united theory for both high and low temperature spreading.

1.3.2 Background Atmosphere Impact on Joint Formation

Controlled Atmosphere Brazing (CAB) is an advanced technology in aluminum brazing process for manufacturing. During brazing, flux on aluminum surface is required to destabilize and destroy native oxide film so that the molten clad can flow freely[28].

Atmosphere quality is one of the most significant variables in the brazing processes. However, in practical industrial applications, it may be overlooked and poorly controlled[29]. And lack of attention has profound impact on the process outcome.

In the case of brazing in Vacuum furnace, discoloration of the brazed part is associated with leak during the heating cycle prior to reaching brazing temperature[29]. This can be attributed to abnormal partial pressure of oxygen in the furnace, which is the primary controlling factor deciding the proper wetting of molten filler metal on the substrate and flow into the joint clearance.

A classic indication of a leak in the CAB furnace atmosphere is an increase in the dew point reading during a brazing process. This is because of the large concentration difference of constituents, such as nitrogen, oxygen and water, between in-furnace atmosphere and out-furnace atmosphere so that the oxygen and moisture will infiltrate into the system if the leaks are present. In order to ensure a good background atmosphere for the furnace brazing, the dew point temperature must be monitored to maintain low humidity.

Measuring the dew point of the gas atmosphere at brazing temperatures by using a continuous-recording dew point instrument is mandatory.

Both the effect of the oxygen level and the humidity magnitude was studied recently experimentally in our laboratory by using the hot stage microscopy and a controlled atmosphere brazing furnace, with samples featuring variable clearance along the interface of bonding metals[9]. It was found that for traditional brazing sheets, where the external fluxes must be used (the sheets consist of an Al alloy substrate and an Al-Si alloy clad), different oxygen level conditions do impact the joint formation and modify the uniform spreading in particular if the oxygen level is above 200 ppm. When the oxygen level reached 500 ppm, non-uniform spreading of molten metal over the substrate was often noticed. Increasing the oxygen level to 2000 ppm results in an increasingly inconsistent and ultimately poor joint formation and in some samples, molten clad failed to spread. When the furnace chamber was filled with air, it was noted that there was no bonding for all samples. As to the influence of humidity, high humidity had a negative impact on the joint formation which can be observed by measuring the joint length along the variable clearance direction, as will be elaborated in detail later.

1.3.3 Topography of Joints and Silicon Diffusion into the substrate

Aluminum brazing plays a major role in the field of heat exchanger manufacturing. A superior material selection such as an AA3003 aluminum alloy bears the merits of high thermal conductivity, low cost and good resistance to corrosion. Industry utilizes empirical methods to control the brazing process. However, these methods do not always work properly due to the lack of thorough understanding of brazing mechanisms. Hence, studies have been conducted in the field of Aluminum brazing including topography of joints and silicon diffusion into the substrate.

Formation of brazed joints is influenced by many variables which directly or indirectly determine the quality of joints such as assembly configuration, the gap between the bonded parts and the volume of the joints. For example, if the gap is too large compared to the available clad volume, the joint may not occur because capillary flow of the melting metal is not capable of bridging the metals to be joined[30]. However, if the gap is too small, the effluents formed at the peak brazing temperature may result in the gas entrapment within the clearance gap which can bring about the generation of voids that severely reduce the strength of the joints[31]. The influence of joint topology on the 2D and 3D formations of brazed joints was discussed[32, 33] with respect to configurations that are similar to the ones found in the field of compact heat exchanger manufacturing. In this study, joint topology is characterized by the following variables: 1) the geometry of the bonding surfaces; 2) the gap between bonding alloys; 3) gravity influence on the joint orientation; 4) the volume of the joint. Several dimensionless parameters were used to define these variables. The finite element method employed is based on minimizing the potential energy of the free surface prior to the onset of solidification. This is facilitated numerically, through a numerical method developed.[34,35] Minimizing the overall energy of the surface results in an equilibrium joint topography shape. The results then were studied to identify the influences of topographical parameters on the spreading length along the bonding surfaces. It is demonstrated[36] that if the mass of the filler metal forming the joint is accurately predicted, topology of joint formation can be determined by using a numerical method proposed. Experimental results have shown that the mass flow rate of the molten filler metal was related to[37]: 1) Si-content; 2) cladding ratio; 3) ramp-up rate; 4) peak brazing temperature; 5) flux converge. However, it is difficult to simulate the dynamics of the clad flow due to the complexity of non-linear, transient, and spatially distributed transport processes[38]. Moreover, it is not possible to directly (without an empirical input) determine the clad mass that forms the brazed joint. In Ref. 37, prediction of the molten clad mass at the onset of solidification was based on the main hypothesis that joint mass is equal to the clad mass difference between initial clad mass and the residual mass. Several other assumptions were also made to solve this problem: 1) Constant densities of all phases; 2) The clad alloy phase change takes place under either equilibrium or non-equilibrium conditions; 3) The solid phase from the mushy zone is distributed evenly and separated from liquid after molten metal flows to the joint area; 4) Mechanical deformation and its influence on clad layer are ignored; 5) The erosion effect on the substrate alloy will not influence the final equilibrium membrane shape at the free surface at the onset of joint solidification. By adopting an approach to minimize the potential energy, the finite element method was implemented and the numerical results were compared to empirical data (the wedge-T and header-tube joints). It was concluded that the main mass balance assumption was proven to be valid. 3D joint topology can also be predicated with an acceptable error (if erosion and 3D effects are not influential and if the residual formation is known). In addition, non-equilibrium Si-diffusion controlled melting process must be considered to predict the brazed fillet size. In order to predict the clad mass flow into the joint, an essential part for this modeling lies in obtaining the mass of the residual clad on the substrate. It was noticed[39] that the residual clad layer formed over the whole substrate consists of primarily α-Al phase[40] and had a uniform topography. With this observation, the volume of the residual clad metal can be calculated by measuring the uniform residual clad thickness, which will assist in predicting the mass of the residual clad assuming constant density of the clad/filler for all phases. The residual mass obtained was subsequently utilized to determine the clad mass flow into the joints prior to the onset of solidification. All previous discussions about joint topography are based on the hypothesis[41] that the controlled atmosphere brazed aluminum joint shape is defined by the shape of the molten metal equilibrium membrane at the onset of solidification. This is confirmed in the study[42] which also revealed that the joint formations are dominated by surface tension, with less influential parameters such as gravity, dissolution phenomena and subsequent solidification.

Brazed joints are formed by a spreading of liquid phase of the filler metal, hence wetting the substrate that is to be joined to another aluminum alloy mating surface is important. The volume of the liquid formed is critical for good brazeability and has an influence on the formation of a sound metallurgical attachment in order to guarantee a proper bond (and an ultimate function of the device featuring this bond) [43]. That amount is also dependent on the clad composition, the peak brazing temperature and clad/core interactions due to silicon diffusion. Insufficient liquid formations, as well as an excess liquid bring both negative impacts on the joining process, such as incomplete bonds and an increased local core dissolution[44]. During brazing, Si diffusion from the clad into the core has been observed and well researched. Si diffusion is due to the relative richness of a solute in the clad[45]. For example, solid-state interdiffusion prior to melting leads to a suppression of the liquid formation due to Si depletion within the clad[46]. Differential scanning calorimetry (DSC) method was used by Turriff et al.[47] to measure the amount of liquid fractions for the case of aluminum brazing sheet with AA3003 Si-lean core and AA4343 Si-rich clad. It was noticed that during heat-up stage, the initial amount of liquid formed is not significantly decreased as a consequence of the clad/core interactions. But the liquid fraction is gradually decreased and can be totally removed by diffusional solidification. Furthermore, a prolonged soak time at elevated temperature (>1 h at 500 °C) does not contribute to a suppress mechanism reducing availability of the initial amount of liquid formed. However, it was found[47] that the presence of the liquid phase above the Al-Si eutectic temperature appears to improve Si absorption by the core and speeding the rate of decrease of molten clad during the brazing cycle.

Based on the fact that a solid state Si diffusion before melting modifies alloy's composition on both sides of the clad-core interface of the brazing sheet and that Si diffusion in the clad subsequently dominates the melting process, a mathematical model through non-equilibrium diffusion-controlled melting was proposed[48]. This was done to evaluate the residue thickness after brazing on the substrate. The sum of the spatial domains caused by the solid phase diffusion prior to melting[49] and that of diffusion controlled melting leads to the total residue thickness. The model was then solved numerically in terms of Si concentration distribution for a moving boundary case. The numerical results were then compared to experimental data of AA4343/AA3003 brazing sheet, demonstrating a good agreement. In addition, it was indicated that the residue formation is strongly dependent on the grain size of the Aluminum clad composite matrix. Gao et al.[50] demonstrated the importance of the determination of the Si diffusion coefficient for modeling joint formation, in particular during the heating segment[32, 33]. In the study, diffusion coefficients of Si were determined in both the joint and residue area in order to analyze silicon migration across the clad-core interface of an Aluminum brazing sheet. It was found that the local variations of diffusion coefficient are noticeable. Subsequently, these coefficients were used to evaluate the joint formation and the predictions were compared to empirical data with a satisfactory agreement.

1.3.4 Summary of Literature Review

Spreading of molten metal clad that forms the joint formation is a phenomena driven by capillary action / surface tension. Several models that govern the surface tension dominated regime have been raised which conform to Washburn type model. In addition, the formation topology in the equilibrium state and silicon diffusion in the clad was well researched and numerical methods to predict the topology and residual thickness were proposed. Besides, it is demonstrated that In a Controlled Atmosphere Brazing furnace, the oxygen concentration and humidity are two influential factors that determine the quality of brazed joints.

However, the kinetics of joint formation of aluminum brazing in a wedge-Tee configuration on a more or less reactive substrate has not been generally studied. These joints are typical in the field of compact heat exchanger manufacturing. Hence, a study such as this thesis work focusing on such phenomena is imperative.

CHAPTER 2: EXPERIMENTAL EQUIPMENT DESCRIPTIONS

Brazing tests (sample configuration given in Figure 2.1) were performed in Optical Contact Angle (OCA) Measuring System. To control the atmosphere in the chamber, nitrogen or compressed air has been supplied to the chamber for a certain amount of time before starting the heating procedure. During the test, the OCA frame panel and hot zone windows were cooled by water at room temperature. The exhaust temperature was controlled before rejecting the effluents to the atmosphere.

2.1 Optical Contact Angle (OCA) Measuring System

The traditional Optical Contact Angle measuring system (OCA 15 plus), manufactured by DATA PHYSICS[51], has been modified for controlled atmosphere operation. It is capable of measuring both static and dynamic contact angle[4] during liquid spreading over the surface at both room and elevated temperatures. In order to study a high temperature wetting and spreading phenomena of molten metal, such as soldering and brazing, the traditional OCA 15 plus system has been modified to OCA 15LHT plus by adding a High Temperature furnace (HTFQ 1200). To accommodate our need for a controlled atmosphere, the hot zone chamber has been modified radically. The original glass tube has been replaced with a thermally conductive ceramics tube which has better thermal conductivity than glass (K_g = 1.4 W/m·K[52], K_c = 25W/m·K at 300 K[53]) and is capable of enduring high temperature (T_{cm}≈1800 °C [52]). The OCA 15LHT plus unit, as seen in Figure 2.2, can sustain up to 1500 °C in the central zone of the hot chamber of the ceramic tube. Special de-coupling inlet and outlet windows, cooled with circulating coolant fluid (water) to keep the temperature of transparent quartz windows not too high, are designed specifically for the experimental program of the NSF sponsored project of which this Thesis work is a preliminary research effort.

The thermal condition of the furnace can either be controlled manually, by specifying a desirable temperature from the panel of a dedicated control unit (see Figure 2.3) or by a temperature program. This program is created in SCA20, a graphical user interface operating software for the unit installed on the dedicated computer. Two temperature values of the heater are displayed on the panel and:

$$|T_{H1} - T_{H2}| \leq 3°\text{C}$$

during the experiment.

A typical operating software interface of SCA20 for this work is shown in Figure 2.4. Since attention must be given to information displayed on the computer screen throughout the experiment, software temperature control is used in this work. Experimental sample is positioned at the center of the ceramics tube to maximize the uniformity of the hot zone temperature field and the corresponding heat transfer rate. There is one additional built-in thermocouple at the center of the tube. However, its position in the tube is below the axis of cylindrical tube (no direct contact between sample and this thermocouple), Figure 2.1. The temperature measured from this thermocouple is the temperature representing hot zone atmosphere temperature at the given location. In view of this, an additional external K-Type OMEGA thermocouple (Part No. KMQXL – 020U-12) for measuring the sample temperature is installed. This thermocouple is attached to the bottom face of the substrate (See Chapter 3 for details) and is connected to the data acquisition system of National Instruments Cdaq-9172 module connected to the dedicated computer. The external thermocouple reading is displayed on the computer through a program created by LabView. For the brazing experiments of AA3003 alloy in the furnace, the sample temperature during brazing cycle is adjusted so that the clad will be exposed to a temperature that corresponds to alloy melting in the range of 569°C-579°C and a dwell time of ~15 minutes. After the joint formation starts, temperature will rise slowly with the average rate of 4°C per minute and finally the temperature reaches 595±5 °C. (See Chapter 3 for details)

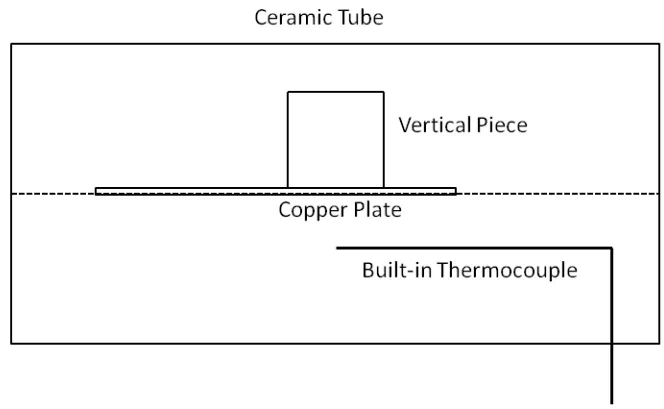

Figure 2. 1 Built-in thermocouple location in the chamber

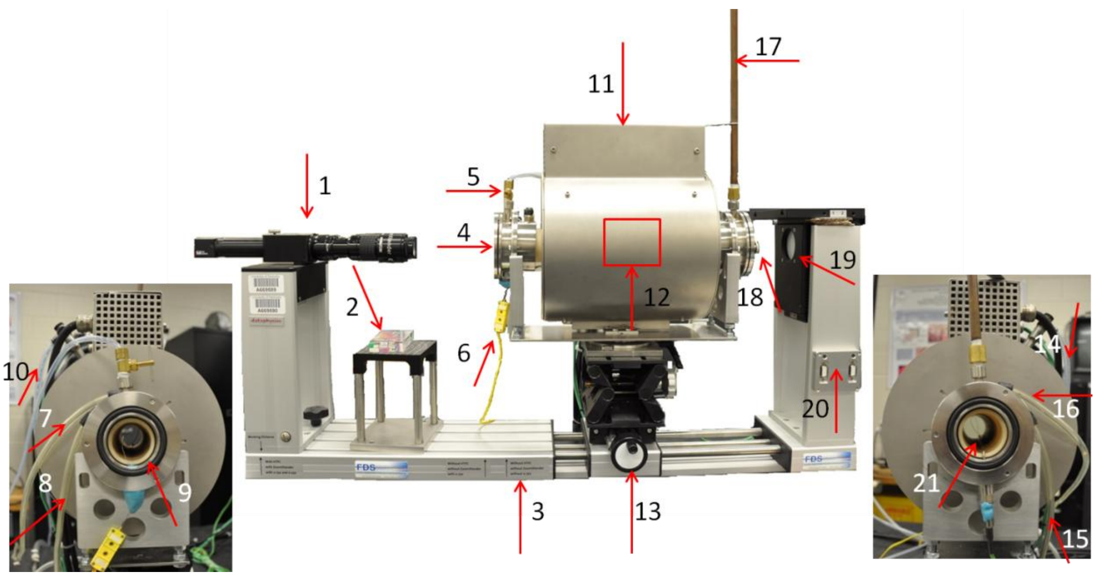

Figure 2. 2 Optical Contact Angle measuring device unit in Brazing laboratory

1 — CCD camera 2 — Bubble level 3 — Frame 4 — Quartz glass window (Left) 5 — Purging gas inlet valve 6 — Sample thermocouple 7 — Flange water cooling inlet (Left) 8 — Flange water cooling outlet (Left) 9 — Thermally conductive ceramics tube 10 — Furnace top cover water cooling outlet 11 — Furnace 12 — Hot zone/Sample location (Inside) 13 — Furnace rotation knob 14 — Furnace top cover water cooling inlet 15 — Flange water cooling outlet (Right) 16 — Flange water cooling inlet (Right) 17 — Exhaust gas outlet pipe 18 — Quartz glass window (Right) 19 — Halogen light 20 — External USB ports 21 — Built-in thermocouple

Figure 2. 3 Furnace controlling unit

1 — Heater temperature display 1 (T_{H1}) 2 — Program controlled heater temperature 3 — Heater temperature display 2 (T_{H2}) 4 — Heating off button 5 — Heating on button 6 — Main Power on/off lever

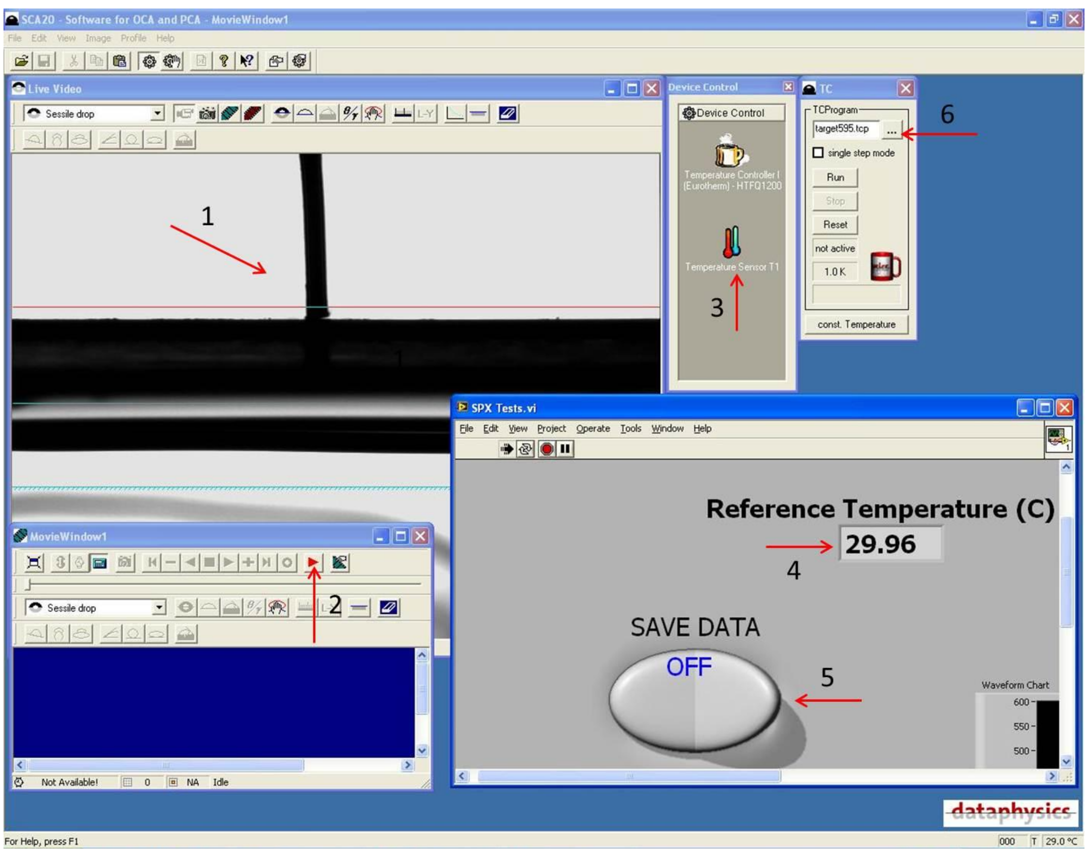

Figure 2. 4 SCA20 software interface

1 — Real time sample recording in the furnace hot zone 2 — Video recording button 3 — Built-in thermocouple reading access 4 — Sample thermocouple

reading   5 — Temperature recording button   6 — Temperature profile selection button

The background of the ceramic tube's free cross-section area is illuminated by a Halogen diffuse light. The appearances of the cross-section (and any objects within it) were recorded by a CCD camera aligned with the axial axis along the hot zone so that spreading kinetics can be observed on the computer screen using SCA20. The relative position of the height of the tube hot zone and the camera-telescope assembly central axis can be adjusted to ensure that the camera, furnace chamber and light source are all aligned in the axial direction. The hot zone can also be rotated in the horizontal plane so that the tube opening can face the operator for manipulating the sample.

2.2 Purging System

Purging system is employed to eliminate residue gas from the furnace chamber and achieve controlled low oxygen level (i.e., a desirable atmosphere in the chamber). A precisely controlled oxygen concentration of the fluid stream at the inlet port allows studying the effects of oxygen level on the kinetics of joint formation. The gas control system includes calibrated composition gas sources, associated regulators, a flow meter and the connecting tubing that links gas sources with OCA 15LHT. See Figure 2.5 for details. The sources are coming from five pressure vessels delivered by Scott-Gross Co. containing Nitrogen or compressed air with 5 different oxygen level (O_2) concentrations: 2 ppm, 210 ppm, 501 ppm, 2003 ppm and ~200,000 ppm. Please note that the actual oxygen concentrations of purging gases for furnace chamber are continuously monitored in an oxygen analyzer that is connected to the exhaust gas outlet of OCA 15LHT unit (See 2.8)

The gage pressure for the gas at the vessel outlet is controlled to be 210 kPa read from the regulator keeping the chamber purged to desirable atmosphere within a reasonable time. For experiments using Nitrogen as purging gas, the furnace chamber was purged for 2 hours with a flow rate of 500 ± 2 ccm, that is, $\frac{5}{6} \times 10^{-5} \pm \frac{1}{30} \times 10^{-6} m^3/s$. The inner diameter of the ceramic tube hot zone is 40 mm with a length of 330 mm. Thus, with the constant flow rate, in a 2-hour time frame, the air volume in the ceramic tube can be replaced for about 145 times to ensure that a desirable atmosphere under controlled purging source is reached.

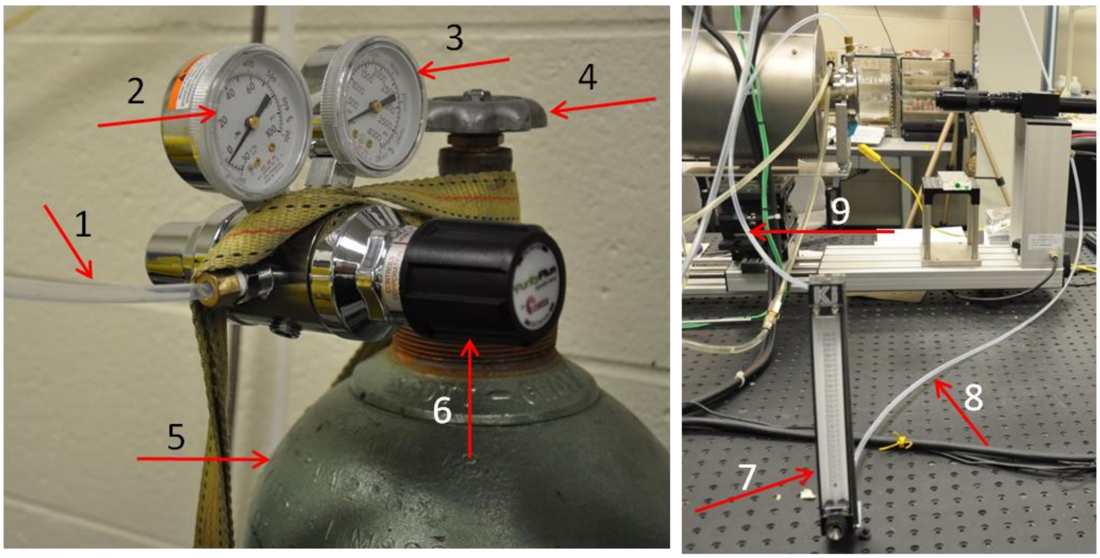

Figure 2. 5 Purging system components

1 — Pressure vessel outlet tubing 2 — Outlet pressure reading 3 — Vessel internal pressure 4 — Open valve 5 — Pressure vessel 6 — Outlet pressure adjusting knob 7 — Flow meter 8 — Flow meter gas inlet tubing 9 — OCA chamber inlet tubing

2.3 Cooling System

For the proper operation of the transparent windows at the two end ports of the hot zone, as well as for safety of the operating personnel and extended service life of equipment, a cooling system is installed for the OCA furnace unit. The cooling system is composed of two sub-systems: (1) Exhaust gas cooling and (2) Flange and frame water cooling

The objective of the exhaust gas cooling is to secure the exhaust temperature of the gas at the exit port to get close to the surrounding room temperature before it is rejected to the outside atmosphere. This objective can be easily accommodated with a simple metal pipe exposed to free convection in a vertical orientation. A corresponding heat transfer calculation model has been devised to predict whether the task will be achieved with the pre-defined length of the copper tubing. A 45cm long copper pipe, as seen in Figure 2.2, is used to connect the hot exhaust gas outlet to a polyethylene tube which is then connected to laboratory roof for releasing exhaust. Based on convective and radiation heat transfer calculation, it is inferred that the copper pipe selected is capable of reducing gas temperature of the low mass flow rate stream under OCA unit's maximum operating temperature. For practical consideration and to secure additional safety margin, a 45cm long copper pipe is installed.

The water cooling system, as seen in Figure 2.6, consists of a water pump manufactured by EHEIM, a tank filed with 14L water from laboratory and associated tubing. The pump takes the cooling water from the tank and delivers it to the flange at either side of the furnace as well as to the furnace frame for cooling. The heated water subsequently returns to the tank and it is mixed with the surrounding water. At any instant, the thermal capacity of the water stream reduces the furnace mantel temperature significantly. Thus, the heat delivered to the tank from the returning water is small and temperature of water in the tank can be assumed to be virtually constant at the room temperature of 26 °C as seen in Figure2.7. The water cycle is shown in Figure 2.9.

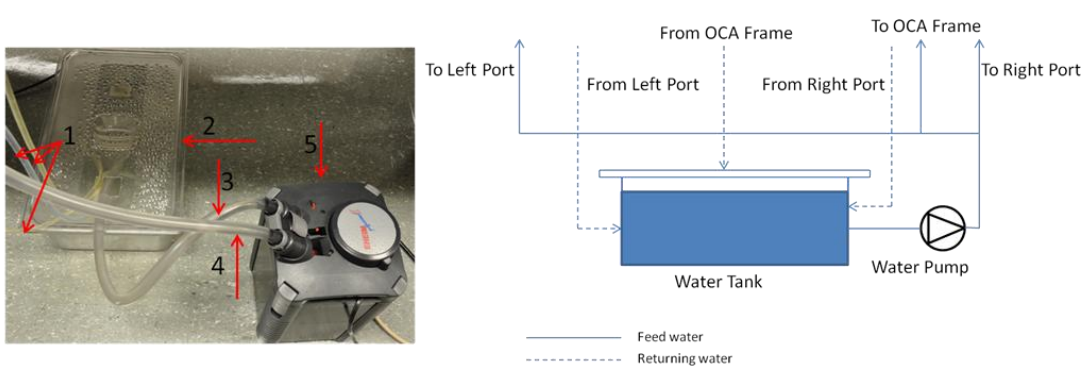

Figure 2. 6 Water cooling system

1 — Returning tubing   2 — Water tank   3 — Pump inlet tube   4 — Pump outlet tube   5 — Pump

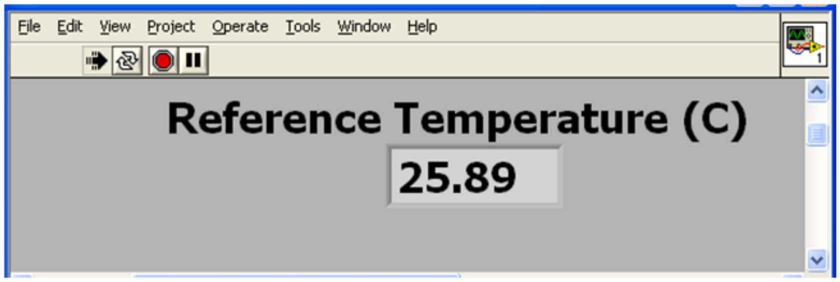

Figure 2. 7 Temperature of water in the tank

2.4 Exhaust Gas Oxygen Level Monitoring System

In order to ensure that the furnace atmosphere is under a prescribed and controlled oxygen level, the exhaust gas outlet PVC tube is connected to a trace oxygen analyzer manufactured by Teledyne Analytical Instruments (316RA) as seen in Figure 2.8. The oxygen level history was recorded at desirable time interval. The analyzer is not suited for measuring the oxygen level of the compressed air[54]. To protect the instrument from potential harm, the compressed air runs are not monitored by the analyzer. Instead, the oxygen level in the compressed air is assumed as for the atmosphere air, i.e., 200000 ppm, as specified by the gas provider (Scott-Gross Co.)[55]. The connecting line schematic is shown in Figure 2.9.

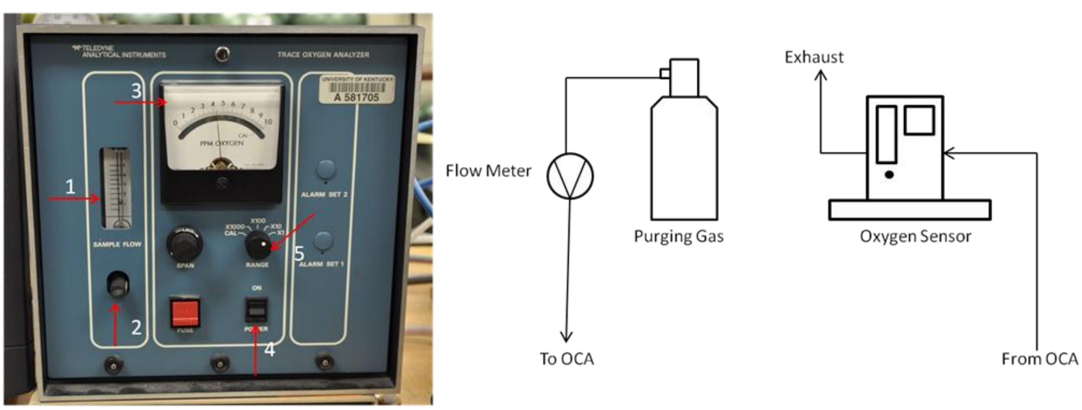

Figure 2. 8 Trace oxygen analyzer

1 — Sample flow rate level   2 — Sample flow rate adjusting knob   3 — Oxygen level reading   4 — Analyzer on/off button   5 — Oxygen level reading multiplier knob

2.5 Experimental System Schematic

The OCA units, the controlling units, the flow meter and the dedicated computer are positioned on an optical table manufactured by MELLES GRIOT (Part # OTTR-305-1219-2438-M6) with controlled vibration system.

Figure 2.9 shows the system schematic for the experimental work.

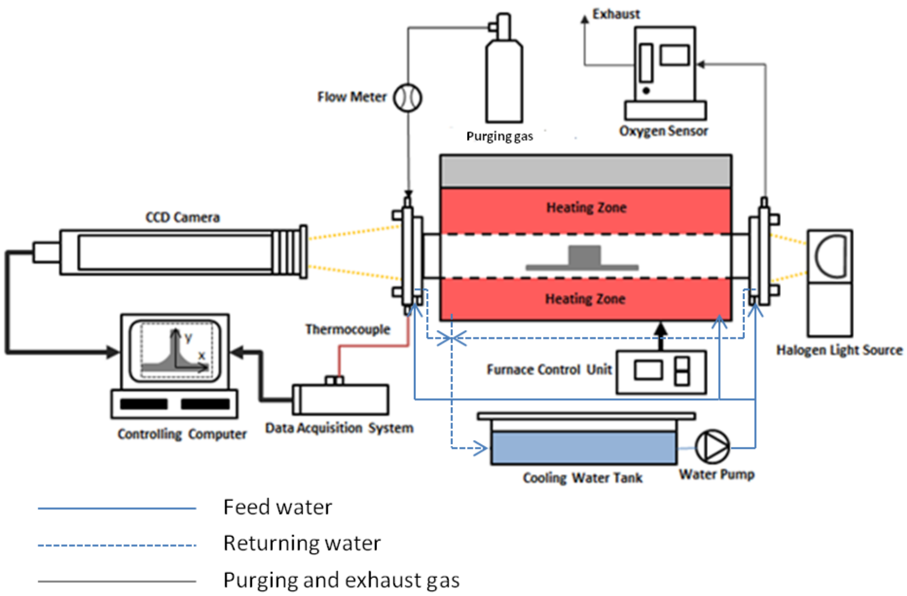

Figure 2. 9 Experiment system schematic

CHAPTER 3: MATERIAL PREPARATION AND EXPERIMENTAL PROCEDURES

The sample joint formation configuration is monitored under controlled atmosphere conditions. The procedure includes test sample making involving clad thickness inspection, oxygen level and temperature recording during joint formation tests, data analysis and post-test sample examination.

The test designations and conditions associated with each test can be referred in Appendix 2.

3.1 Sample Preparation

3.1.1 Sample Configuration

The isometric and top views of the sample are shown in Figure 3.1 and Figure 3.2, respectively.

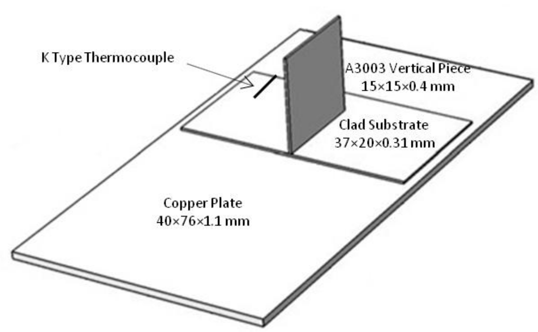

Figure 3. 1 Isometric view of sample configuration

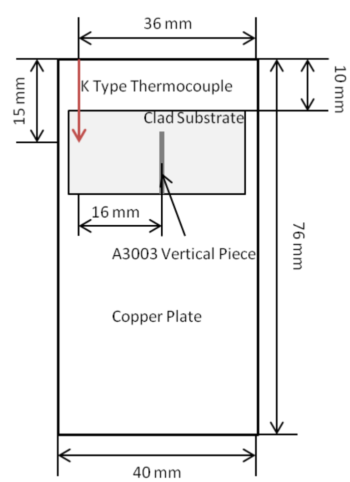

Figure 3. 2 Top view of sample configuration

The sample assembly is mainly composed of three rectangular parts:

(1) One 40×76×1.1 mm copper plate for holding T-joint samples. The plate is inserted at the center of the ceramic tube of the hot zone (see Figure 2.2 for the configuration). The plate is positioned freely in the tube, horizontally to ensure that the substrate is located at the centerline position within the hot zone.

(2) One 37×20×0.31mm clad substrate (brazing sheet) is positioned on the copper plate (see Figure 3.2). The substrate is made of Al-5%Si clad with an A3003 core[9]. No flux is required for brazing in the furnace.

(3) One 15×15×0.4 mm vertical A3003 piece represents the mating surface (see Figure 3.1). This piece is fixed on the substrate by two stainless steel wires with a diameter of 0.4mm wrapping the bottom of the copper plate to the top edge of the vertical piece.

All raw materials were first manually cleaned with 95% ethanol and then ultrasonically cleaned with 95% ethanol for ~ 2 minutes in order to eliminate any oil or chemical residues. The materials were dried in air for subsequent use.

The K type external thermocouple mentioned in 2.1 is placed at the left side of bottom face of the substrate as shown in Figure 3.2. Its tip is intentionally bended lightly upward to guarantee it is in intimate contact with the brazing sheet. This thermocouple is capable of measuring temperature in the range of 0 °C ~ 1335 °C and with measuring deviation ± 1.5 °C at 590 °C[56, 57].

The sample is positioned in the chamber horizontally with a deviation from horizontality of 1.5° maximum. The small deviation limit imposed is assumed to have a negligible impact on the joint formation. The angle between vertical piece and the substrate is measured by Image-Pro software as shown in Figure 3.3 in order to control the angle between the mating surfaces within the range of 90° ± 1.5°.

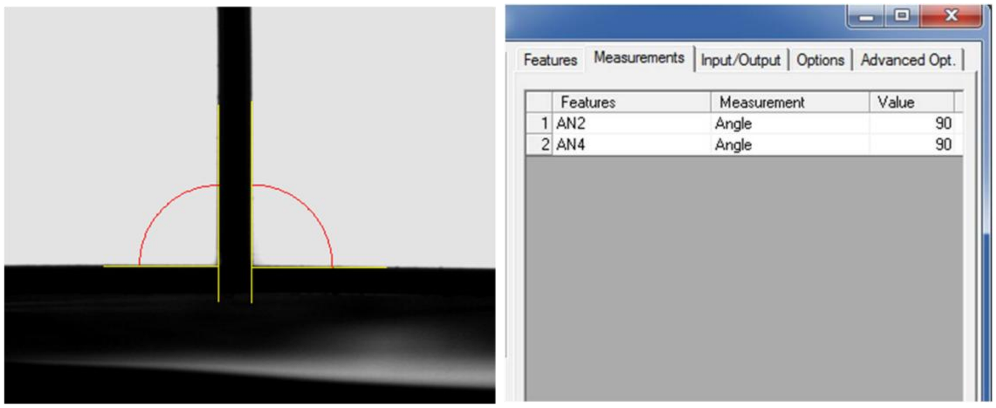

Figure 3. 3 Measurement of angel between vertical piece and substrate

3.1.2 Clad Thickness Uniformity

All the clad sheets in this work were taken from the same piece of an original clad sheet material. However, these sheets were manufactured by hot rolling under laboratory conditions and there is a possibility that some samples may feature a variable clad thickness, primarily within the edge zone orthogonal to the longitudinal direction of observation. Hence, before analyzing kinetics data, a clad thickness study must be conducted to verify whether a uniform thickness of the clad exists, and to ensure that all the brazed samples have the same initial conditions.

Three test samples and three test edges are randomly chosen, extracted from the 40×60 mm original clad sheet materials as shown in Figure 3.4. The attention was paid in particular to the edge zones. A uniform clad thickness has been established at the center along the longitudinal sheet direction, what may in principle not be the case with the lateral locations.

These test samples are partitioned, resin mounted, polished at edges and the cross-section were etched. They are ultimately observed by using a Nikon EPIPHOT 300 microscope and recorded by using a dedicated the computer to measure in situ the clad thickness before brazing. *Image-Pro* software is used to measure the thickness at a left, a left-center, a center, a right-center and a right position for each edge locations. For each location, three measurements were recorded in the order starting with the center, left and right, respectively (Table 3.1). Figure 3.5 shows the clad thickness measurements for test sample 1. The pixel numbers are measured and then converted to actual dimension in the unit of µm as indicated on a linear scale on the top left corner of each figure. Since the measurements were taken on the screen using accessory software, the error resulted from the number of pixels the operator selected to represent the thickness. In this uniformity study, the uncertainty of measurement at each location is determined as being the standard deviation of three measurements.

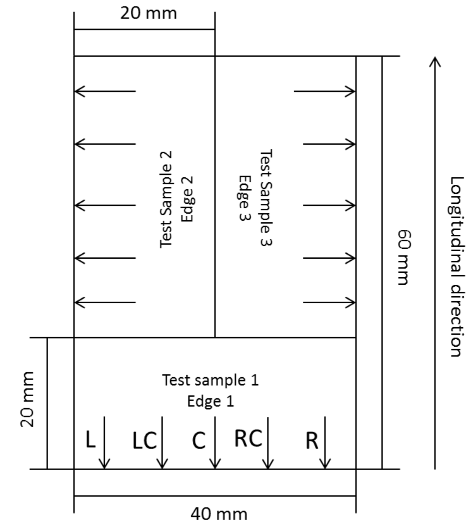

Figure 3. 4 Test samples and edges of the measurement of clad uniformity on a sheet

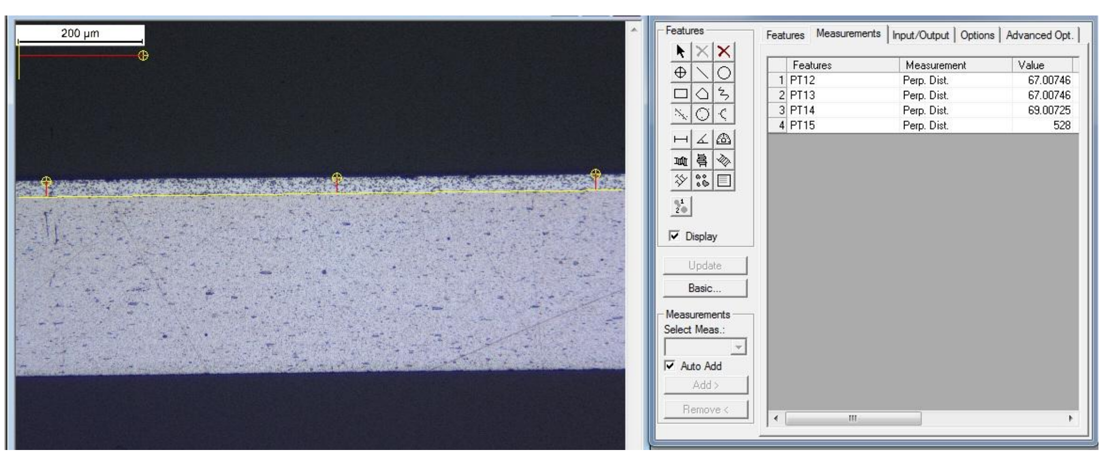

(a) Left

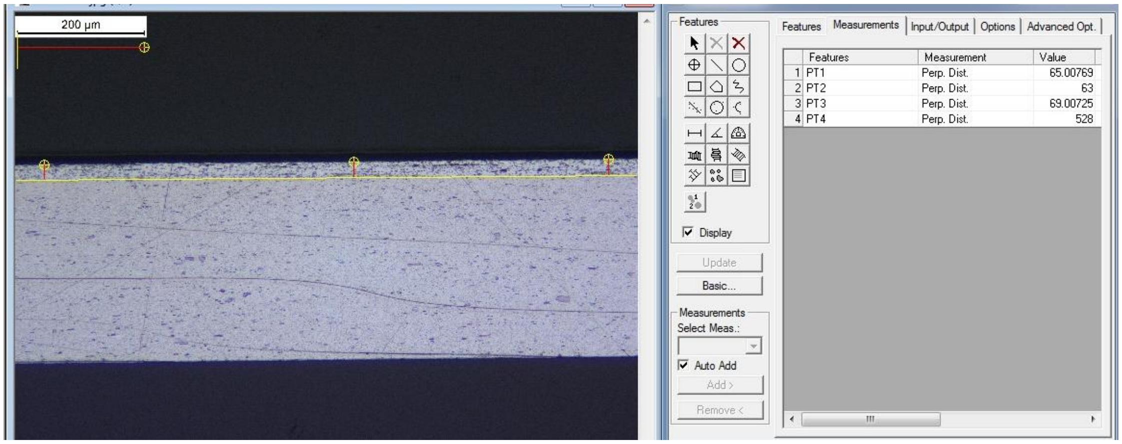

(b) Left-Center

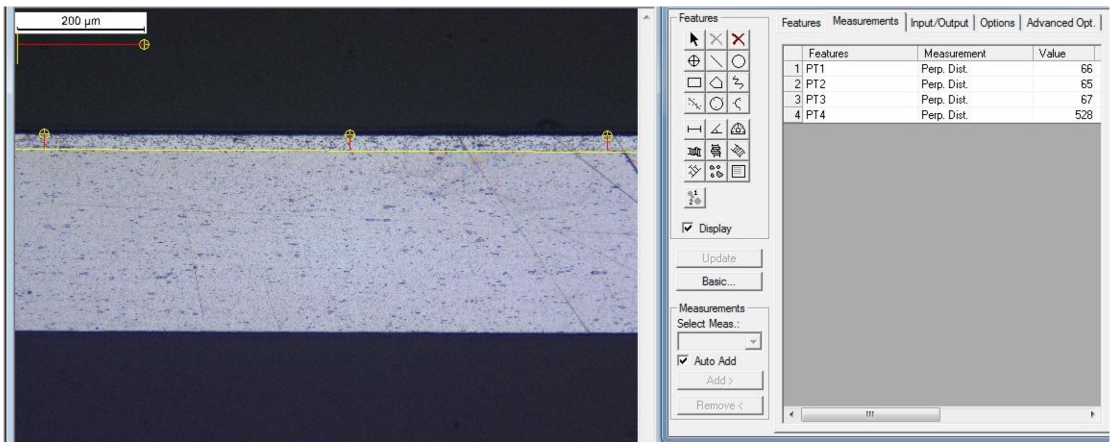

(c) Center

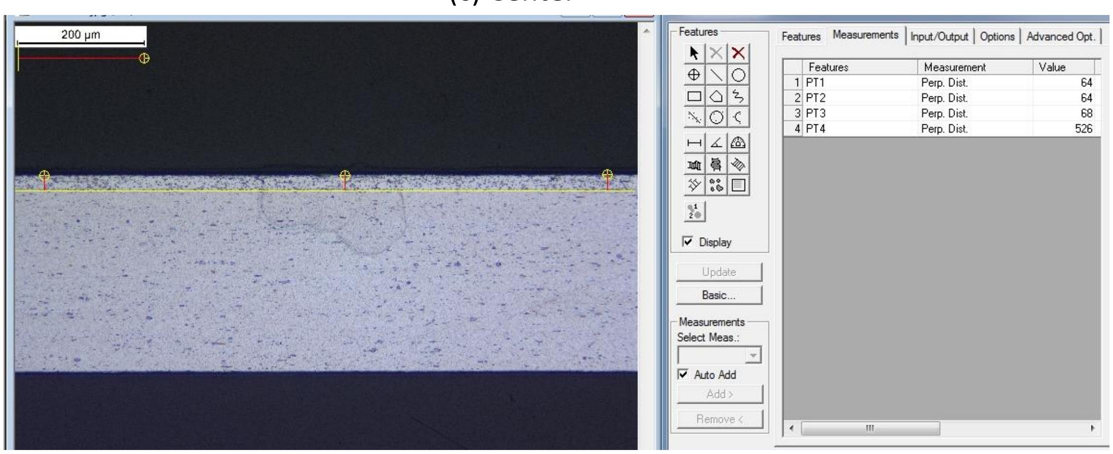

(d) Right-Center

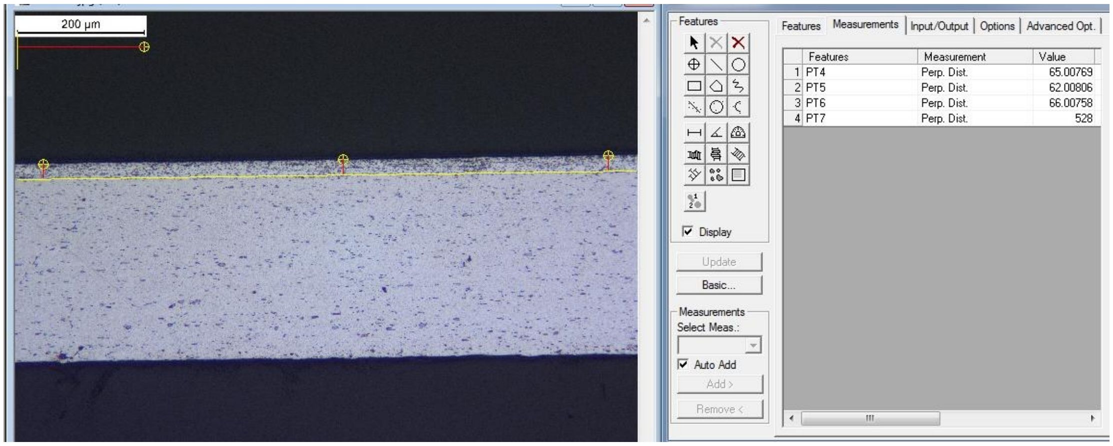

(e) Right

Figure 3. 5 Clad thickness measurements for Test sample 1. (a) Left (b) Left-Center (c) Center (d) Right-Center (e) Right

Table 3.1 summarizes the measurements of clad thickness for all the test samples. The average of three thickness measurements at each of the five locations is provided.

From Table 3.1, it can be concluded that no significant thickness difference exists for all test samples. That is, all the samples indicate very uniform distribution of the clad layer thickness before brazing. Therefore, each tested sample from the same sheet will be well represented as having identical mass of clad available to form the joint for a given, precisely tailored test samples. In the subsequent study, the clad thickness is treated to be a constant, which is equal to the average clad thickness for all the test samples,

$$\delta_{clad} = 25 \pm 1\ \mu m$$

Table 3.1 Clad thickness measurements for all pre-brazed test samples (μm)

	Test Sample 1	Test Sample 2	Test Sample 3
Center (L)	25	27	25
Left (L)	25	26	24
Right (L)	26	26	24
Average Left (L)	26	26	24
Left Std (L)	0	0	0
Center (LC)	25	25	26
Left (LC)	24	24	26
Right (LC)	26	26	26
Average Left-Center (LC)	25	25	26
Left-Center Std (LC)	1	1	0
Center (C)	25	26	25
Left (C)	25	24	26
Right (C)	25	26	26
Average Center (C)	25	25	26
Center Std (C)	0	1	0
Center (RC)	24	24	26
Left (RC)	24	25	24
Right (RC)	26	25	26
Average Right-Center (RC)	25	25	25
Right-Center Std (RC)	1	1	1
Center (R)	25	23	26
Left (R)	23	24	25
Right (R)	25	25	25
Average Right (R)	24	24	26
Right Std (R)	1	1	1
Average Thickness of Sample	25	25	25
Standard Deviation	1	1	1

3.2 Experimental Procedures

3.2.1 Chamber Atmosphere

In order to study the kinetics of the clad spreading and joint formation during a brazing process under conditions of a Controlled Atmosphere Brazing, the OCA chamber atmosphere must be well defined. One of the essential factors of the atmosphere on the brazing process is the oxygen level in the chamber. As mentioned in Chapter 2, the purging gas sources include Nitrogen with specified content of oxygen, i.e., 2±2 ppm, 210±4 ppm, 501±10 ppm, 2003±40 ppm Nitrogen and 195000 - 235000 ppm air. For the convenience, all the oxygen levels are rounded to their nearest hundredth (200 ppm, 500 ppm, 2000 ppm and 200,000 ppm) for concentrations within the hot zone except for the 2 ppm case in which a 70 ppm is used due to the fact that the chamber condition can only offer 70±10 ppm in a 2 hours time frame. The certified specifications of gas sources are provided in Appendix 1.

The oxygen level history for 70 ppm, 200 ppm, 500 ppm and 2000 ppm Nitrogen gases were recorded throughout the duration of each test as shown in Figure 3.6. The recording of the Oxygen level data starts at the time when the temperature reading is initiated (typically at ~ 30 °C). The data include oxygen level corresponding to temperature history between ~ 577 °C and the peak brazing temperature (heating segment), and from peak temperature to 550°C (cooling segment), see Figure 3.7. Therefore, the oxygen level history in the chamber during the whole brazing time is documented. From Figure 3.6, it can be identified that during the whole joint evolution time (the region between Start line and End line, see Figure 3.6 and Figure 3.7) the oxygen level in the chamber is under its controlled condition.

In this work, it is assumed that a 2 hour purging time is sufficient to eliminate H_2O in the chamber up to the point of minimal H_2O vapor impact. Therefore, the humidity in the chamber is not measured. The certified moisture level in high purity (99.999%) Nitrogen and compressed air is <3 ppm and <8 ppm, respectively provided in Appendix 1. In addition, the difference of oxygen concentration (ΔO_2) between specified in Appendix 1 and measured from Figure 3.6 for 200 ppm, 500 ppm and 2000 ppm dry high purity Nitrogen tests at the start of spreading is 10 ppm, 41 ppm and 3 ppm, respectively. Since the difference in oxygen level is marginal, it can be concluded that the difference in moisture level are marginal as well. The typical dew point of air for brazing test in our lab is -54 °F after three hours purging[63].

The recorded oxygen concentration data for all tests are offered in Appendix 3.

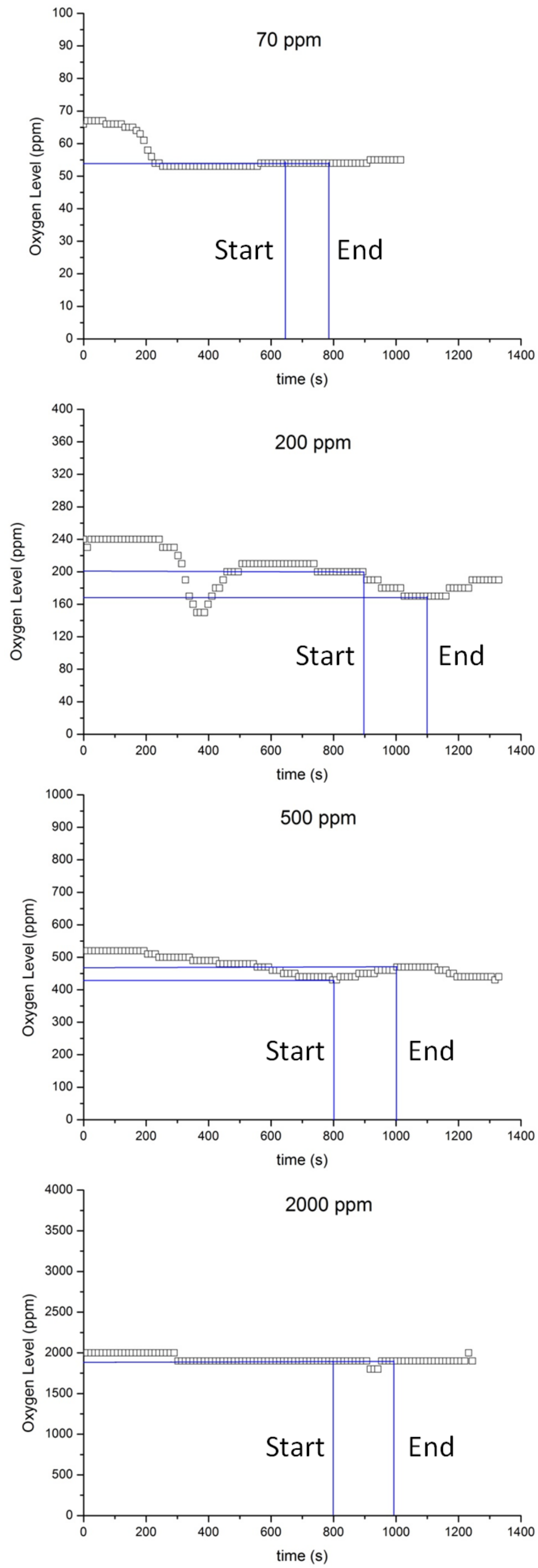

Figure 3. 6 Oxygen level history of one test from each group (Test5_70, Test2_200, Test1_500, Test9_2000)

3.2.2 Temperature Profile and History

There were three temperature profiles associated with each experiment: (1) The computer program controls the heater target (setup) temperature and indicates the desired heater temperature; (2) Average two heater temperatures displayed on the controlling unit (see Figure 2.3) and; (3) External K type thermocouple temperature measurements of the substrate. These temperature profiles may be different from each other as can be clearly seen in Figure 3.7 which shows the three temperature profiles in one plot. In this study, the heater maximum target temperature is set to be 655 °C to establish a desired hot zone temperature (featuring a significant temperature delay) and to prevent the external thermocouple temperature from rising beyond 595 ± 5 °C (established by a trial-and-error). The computer program is set to increases the heater temperature from 30 °C to 655 °C in 5 minutes and after that the heater keeps that temperature for a specifically defined time until the heater off button is activated. However, the actual heater coil temperature displayed on the controlling unit initially rises quite lagging behind the computer program heater temperature due to inertia but after ~200 seconds the two profiles are on top of each other (see Figure 3.7). The external thermocouple temperature profile is the one that is registering the sample temperature. This temperature was recorded during heating segment from ~ 30 °C to ~ 595°C and during cooling segment from 595 °C to 300 °C. The video recording was triggered once the external thermocouple temperature reaches 568 °C. The joining process starts in the external thermocouple temperature range of 570 °C and 580 °C. The joining processes take less than 120 seconds (or alternately 180 seconds for the higher oxygen concentrations) and once the external thermocouple temperature reaches 595 °C, the heating program was terminated. The external thermocouple temperature rises very slowly between 595 °C and 600 °C. It is ensured that at least 4 minutes long video can be recorded before the temperature decreases to below melting temperature.

The theoretical melting temperature of clad layer (Al-Si binary alloy) is known (577 °C), solidus temperature. However, melting was observed from the external thermocouple readings in the range of temperatures, i.e., between 570 °C ~ 580 °C. We were aware that the joining process is not isothermal (Figure 3.7), but the temperature deviation from the onset temperature of formation evolution is within the range of 10 ± 5°C. It was assumed that this non-isothermal process has only little influence on the change of the joint formation. This may be most likely due to the fact that melting temperature of the clad alloy is not the same as for a typical Al-Si binary alloy, but also because the temperature non-uniformity of the clad layer may be present. It is assumed that the external thermocouple's measuring uncertainty is significantly smaller than the previous two reasons. The thermocouple touches the bottom of the substrate and there is some 16mm distance between the thermocouple location and the joining zone as seen in Figure 3.2. Nevertheless, since the clad substrate is very thin (0.31 mm) and aluminum alloy has a good thermal conductivity, it can be argued that the temperature distribution on the substrate should be more or less uniform. In order to verify this, a thermal Finite Element Analysis is performed using ANSYS 12.1 (Refer to Appendix 4 for details).

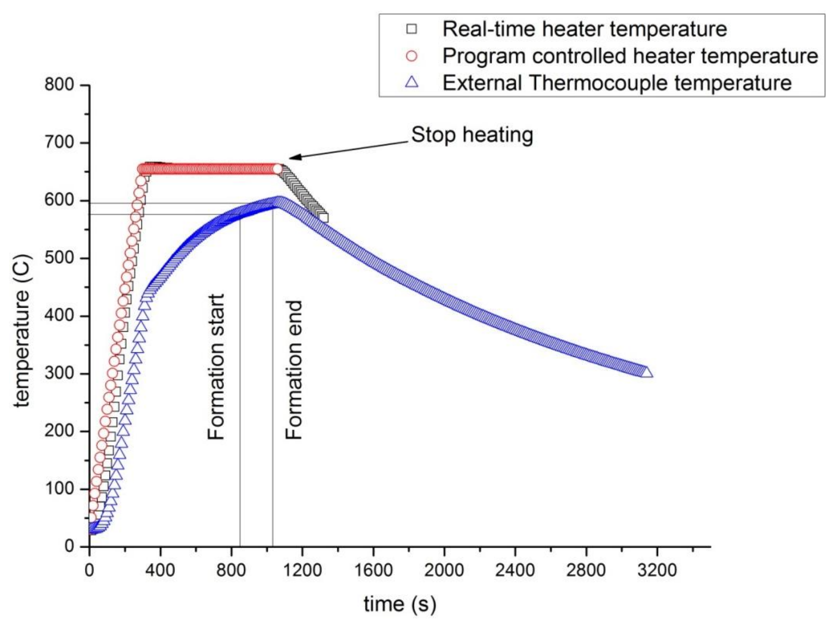

Figure 3. 7 Typical temperature histories for one experiment (Test11_2000)

The recorded external thermocouple temperature data for all tests are arranged in Appendix 5.

3.3 Post Experiment Processing

3.3.1 Data Processing

The domain of interest is not the entire sample configuration. Rather, the domain of interest is the area shown in Figure 3.8 which covers the entire joint molten clad domain.

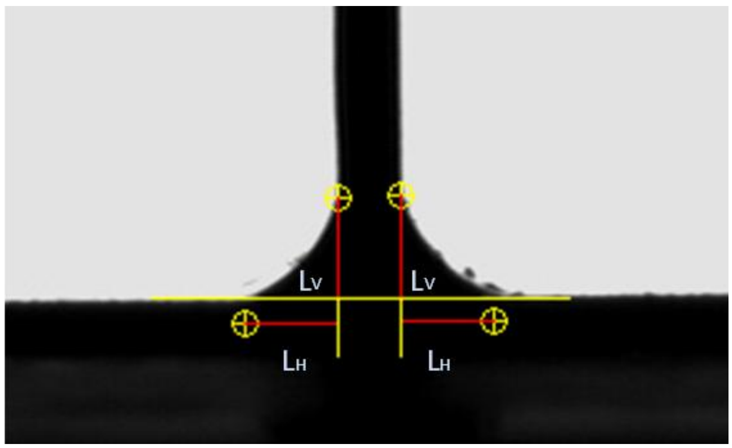

Figure 3. 8 Joint domain (Test5_70)

The horizontal and vertical lengths of the joint formation are represented by L_H and L_V, respectively (Figure 3.8). Both dimensions at left side and right side were measured.

The videos begin to be recorded at 565 ± 5 °C of external thermocouple reading. The whole brazing process was recorded for more than 120 seconds for the 70ppm group and for more than 180 seconds for the 200ppm, 500ppm and 2000ppm groups to ensure that spreading ends before the recorded time was terminated. The recorded video file format type (.seq) is the one that is uniquely associated with SCA20 operating software and has 25 frames per second (FPS). The original video file was converted into an avi-type file and 120 or 180 images are extracted from that file at the rate of one image per second using Virtualdub software[58]. Figure 3.9 shows a sequence of joint formation images extracted from the video at different times through the whole process. Appendix 6 offers a summary of a procedure for uncertainty of kinetics data evaluation. One sequence of extracted images for each test group can be referred to Appendix 7. The vertical and horizontal lengths are measured using the Image-Pro[59] as follows:

(1) 0 ~ 30s: Formations measured at every second

(2) 30 ~ 60s: Formations measured at every other second

(3) 60 ~ 90s: Formations measured at every 3 second

(4) 90 ~ 120/180s: Formations measured at every 5 second

Before each measurement, the images were calibrated by measuring the numbers of pixels of the known vertical piece thickness (0.4 mm) in Image-Pro. This allows calculating M, the length per pixel, for continuing measurement. By measuring the number of pixels of the vertical (N_V) and horizontal (N_H) location of the triple-line, the actual dimension can be obtained through the following equations:

$$L_V = N_V \times M$$

And,

$$L_H = N_H \times M$$

The thickness of the vertical piece was re-measured to confirm the calibration. If the re-measured thickness has a deviation of 0.01 mm from known thickness 0.4 mm, then a new M will be calculated to repeat the above procedures until convergence is reached.

A typical joint formation measurement can be seen in Figure 3.10

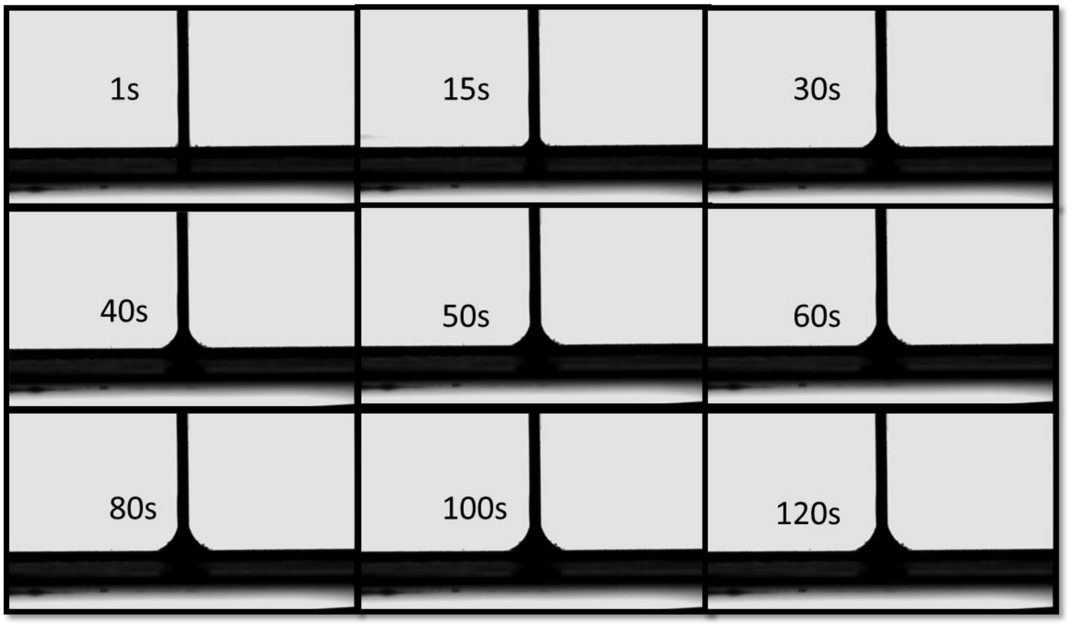

Figure 3. 9 Joint formation evolution. Images extracted from a video (Test5_70)

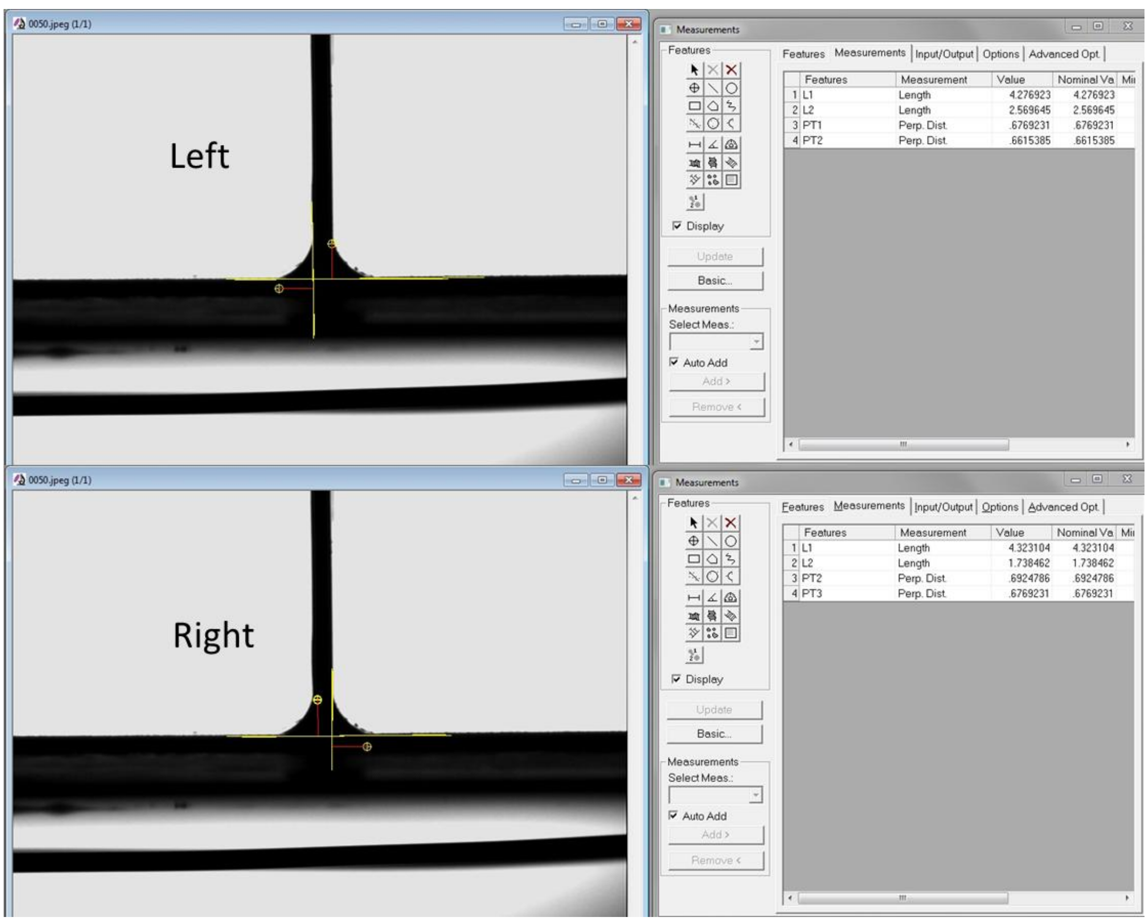

Figure 3. 10 Measurement of joint formation of Test5_70 at 30s

3.3.2 Post Processing of Brazed Samples

One of the brazed samples from each experiment's group is randomly selected for a metallurgical study that includes primarily the inspection of the metallurgical cross section, presence of voids and/or irregularities of the cross section of a joint. Cold mounting method is used to make the samples available for subsequent cutting and polishing. Each sample was grinded with a sequence of polishing grits (#220, #500, #800 and #1200) and then polished using polishing runner (9 μm, 3 μm and OPU) with associated suspension and lubricant. This was followed by an etching procedure using HF + 3 ml HCl + 5 ml HNO_3 + 190 ml H_2O. Final formation shape study was conducted with the help of Nikon EPIPHOT 300 microscopy with appropriate magnification and measurements examined using Image-Pro Software. These values are used to compare with those measured from OCA units. All the cut and polished samples are kept for the use in the subsequent study (see chapter 4).

CHAPTER 4: RESULTS AND DISCUSSIONS

In this chapter, the results are divided into five groups in terms of oxygen concentration and plots of each test group are presented to identify the evolution phases. Subsequently, a topology study has been presented discussing clad residue and its influence on joint formation. The cross-sections profiles are examined to verify whether a 2D or 3D configuration of joint formation is present.

Refer to Appendix 8 for kinetics data for all tests from all groups.

4.1 70 ppm Test Group Results

Seven tests in this test group were successfully conducted with the same atmosphere conditions (70 ppm oxygen level in the chamber with 2 hour purging duration and wedge-tee sample configurations in the hot zone of the OCA units), Figure 3.1 and Figure 3.2. Figure 4.1 shows the kinetics curves of Test5_70 and Figure 4.2 offers the average values for all the seven tests with associated error bars[60] (Appendix 6) in linear coordinates at both original time interval (refer to 3.3.1) and intervals of every 10 second.

Figure 4.1 and Figure 4.2 clearly indicate that both joint vertical growth (L_V) and horizontal growth (L_H) (Figure 3.8) reach their maximum values in ~100 seconds for 70 ppm test group. Under the term "growth" we define the maximum reach (at an instant of time) of the triple line along the spreading direction over a respective (vertical or horizontal) surface. The triple line is, as emphasized earlier, the locus of points at which all three phases meet (1) liquid metal, (2) substrate over which the spreading takes place, and (3) gas atmosphere in contact with the previous two. This means that the whole kinetics of the spreading process takes less than 2 minutes to be fully developed.

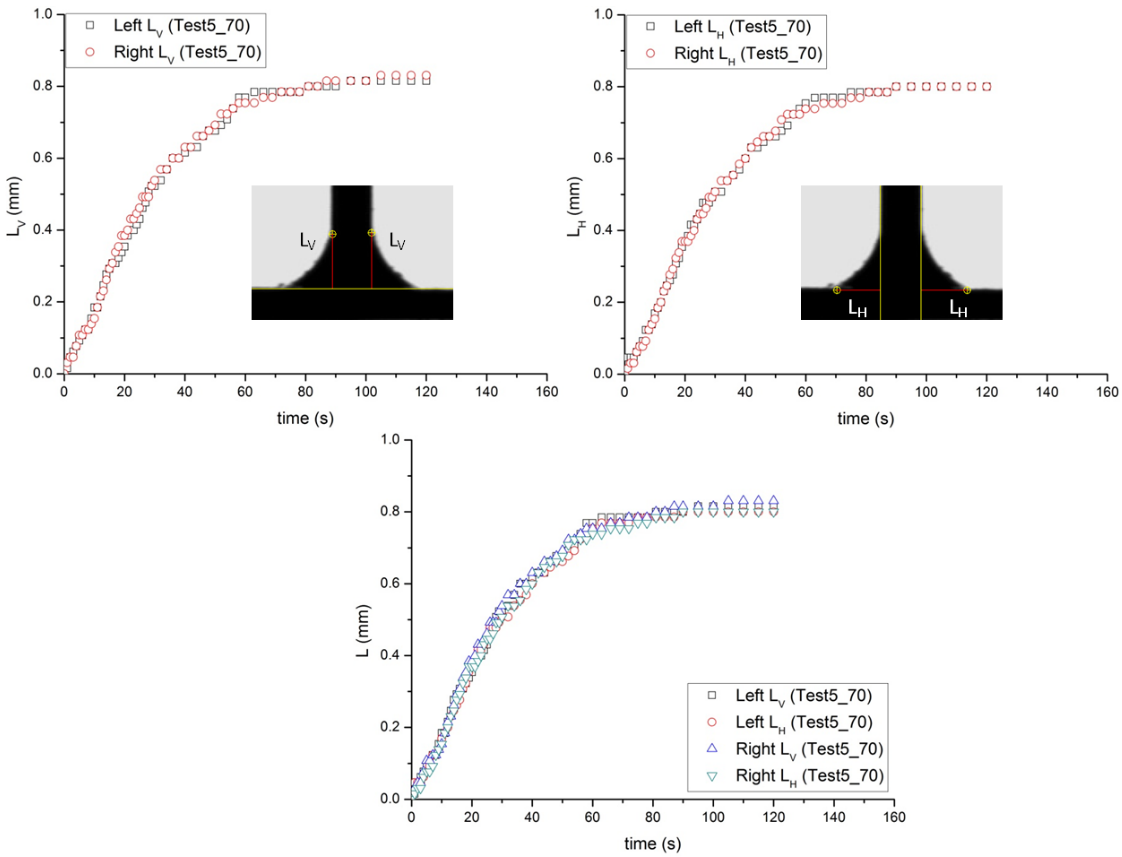

Figure 4. 1 Kinetic curves for Test5_70 of 70 ppm test group

In addition, the vertical and horizontal movements are processed in a similar way, reaching average maximum values at about 0.8 mm in both cases. Gravity has been assumed to make the triple line movement in the vertical direction, against the gravity action, smaller than in the horizontal direction. However, as one can easily conclude from Figure 4.1, there is no significant difference between L_V and L_H curves, implying that the dominant force driving the flow is surface tension in both directions and thus the impact on vertical flow from gravity can be neglected (for the given joint filet size considered). Moreover, it is apparent that the kinetics is symmetric since the left and right curves are on top of each other from these figures. That implies that the sample symmetry, as well as clad uniformity (discussed in 3.1.2, see Table 3.1) are clearly preserving surface tension flow of the same liquid masses on both sides of the joint zone. One should note that spreading condition on horizontal and vertical surfaces are not the same. Molten metal "climbs" vertical surface originally solid and is exposed to possible dissolution/interaction at the liquid/solid interface only after liquid spreads over it. Horizontal surface provides liquid phase from originally solid clad that is hypoeutectic, hence melting passing through mushy zone. Still, no significant difference was identified.

No obvious difference between vertical and horizontal spreading is noted for averaged values in Figure 4.2. This clearly implies that gravity has negligible impact on the formation regardless of the increasing size of the liquid fillet.

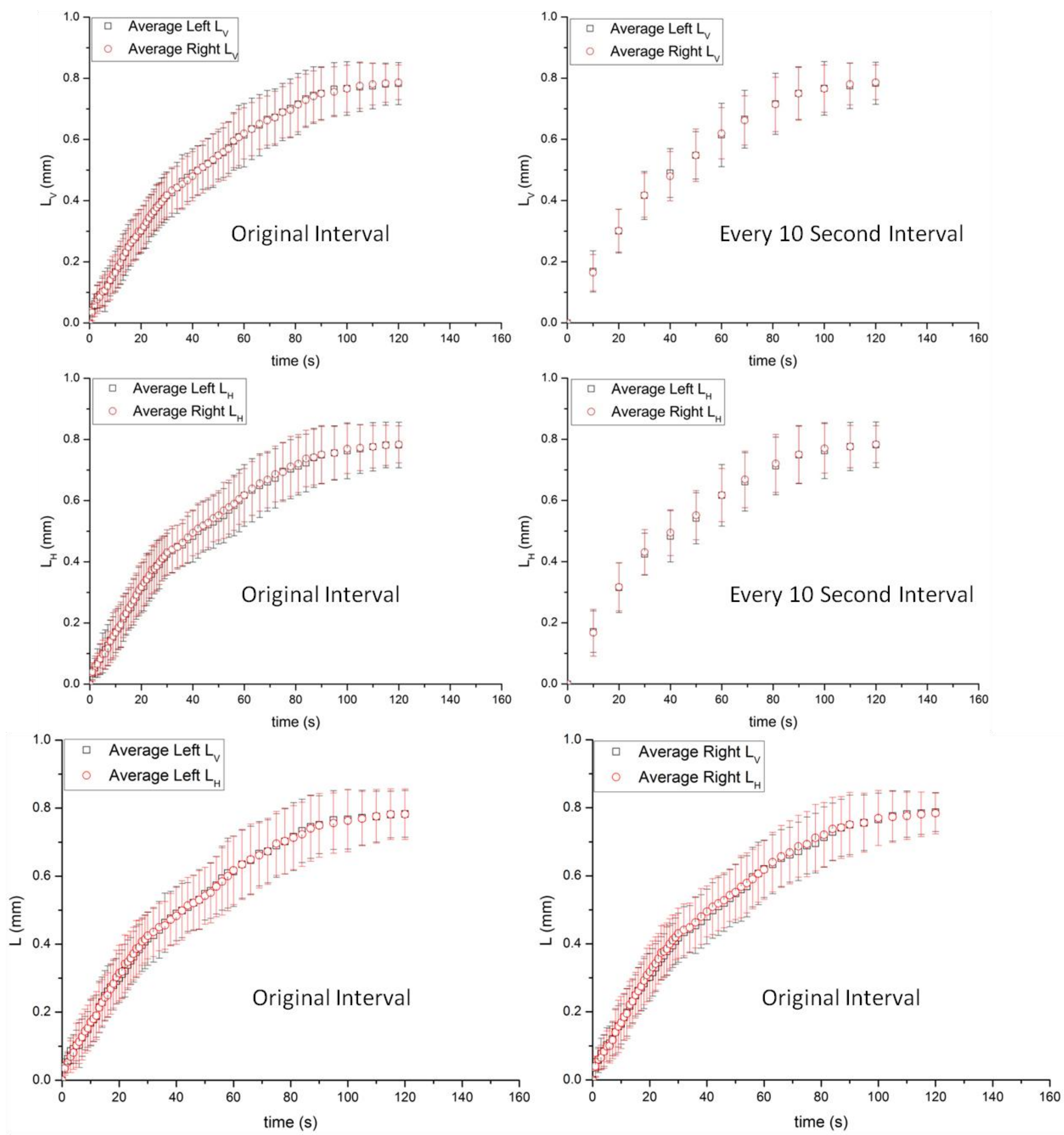

Figure 4. 2 Average kinetic data of Test1_70 through Test7_70 (Test4_70 included)

The trend of these curves appears to be similar to that of a power law curve. That is, the triple line movement appears to obey the power law relationship vs. time (L ~ t^n, n<1). In order to verify if a power law relationship exists between joint growth (that is, the triple line movement) and the spreading time, these curves are examined in logarithmic coordinates. If the power law is to be confirmed, the correlation must correspond to a linear data distribution in a log-log coordinate system. Figure 4.3 shows the linear curve fit for Test3_70.

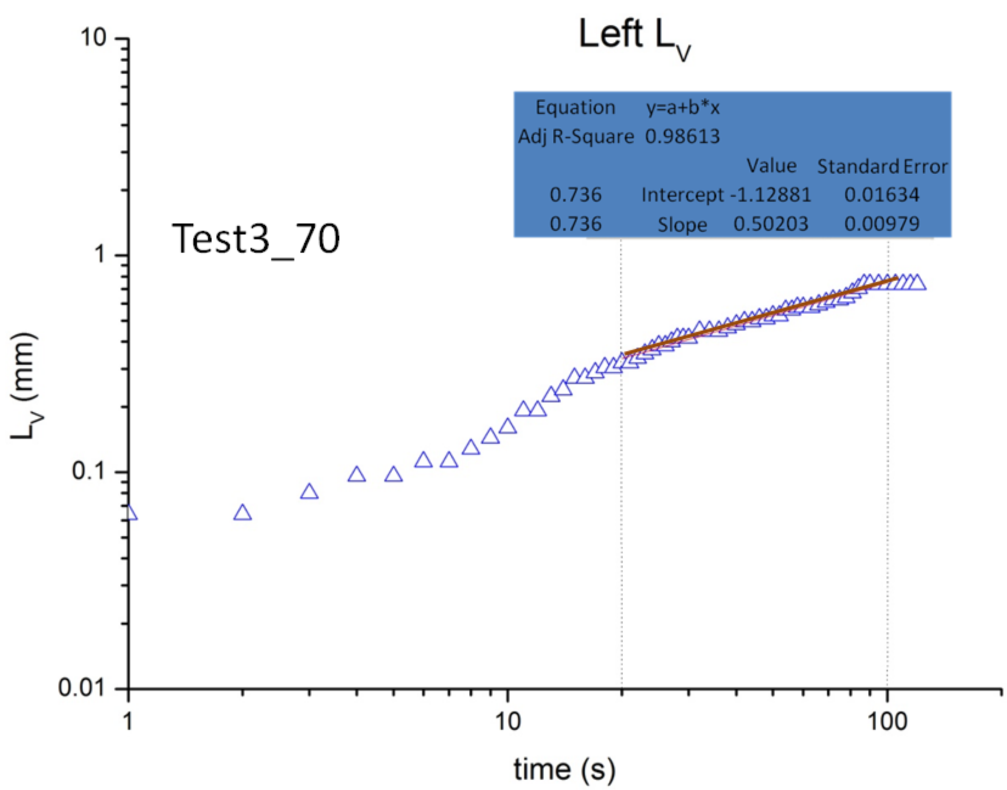

(a)

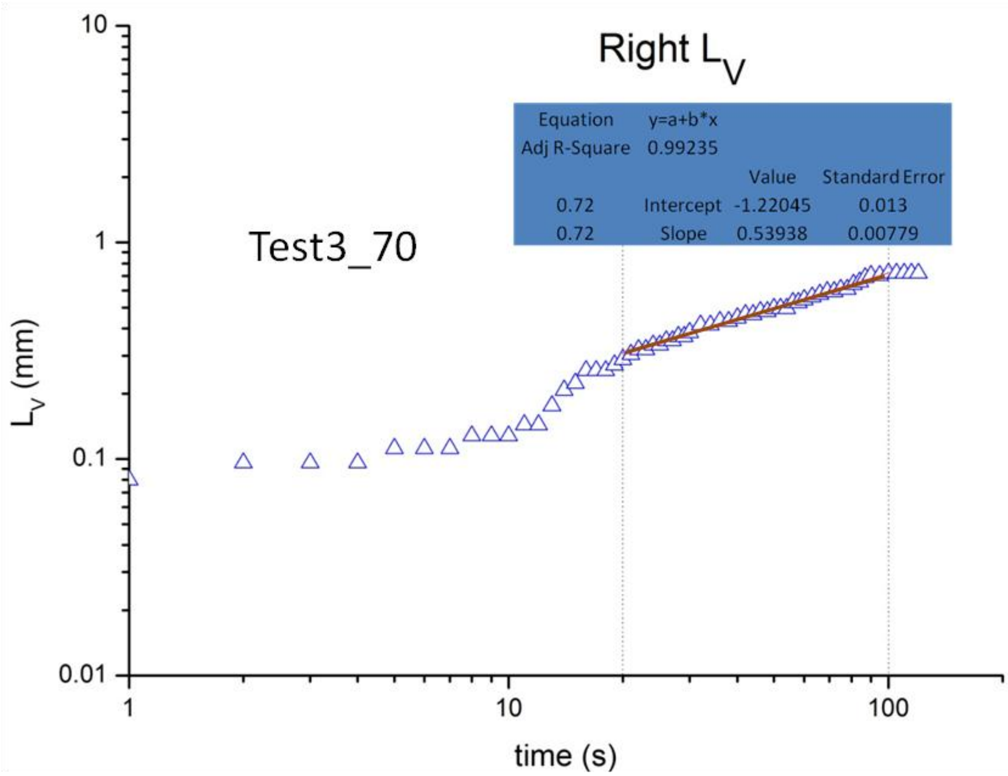

Right L_V
Equation y=a+b*x
Adj R-Square 0.99235
Value Standard Error
0.72 Intercept -1.22045 0.013
0.72 Slope 0.53938 0.00779
Test3_70
L_V (mm)
time (s)
10
1
0.1
0.01
1
10
100

(b)

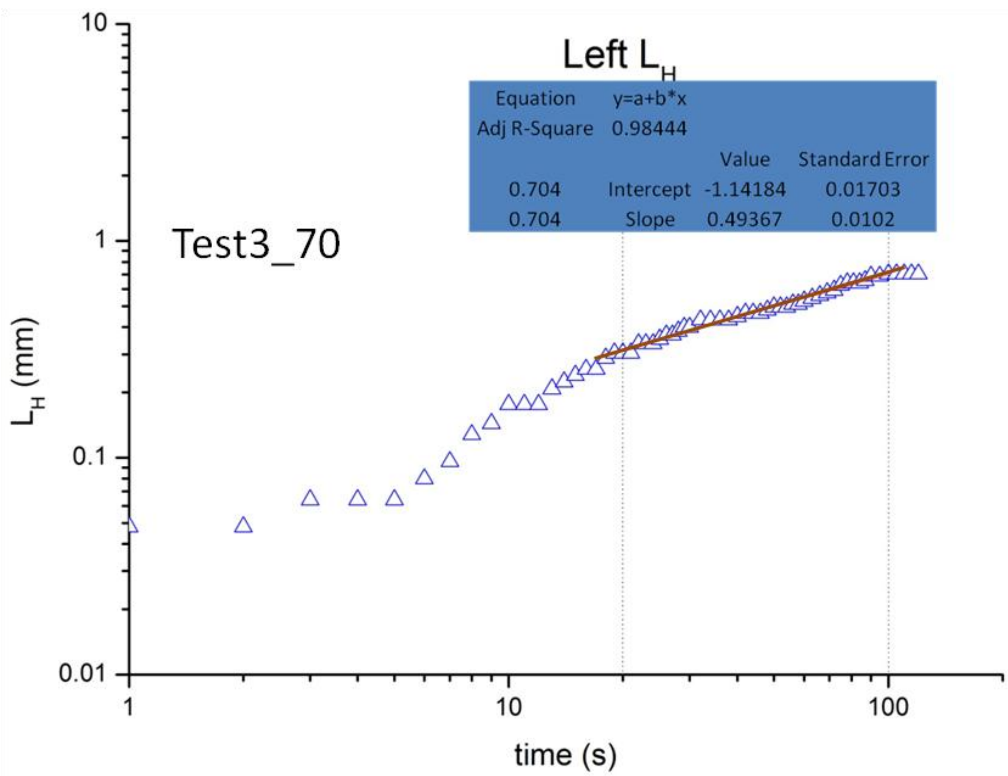

Left L_H
Equation y=a+b*x
Adj R-Square 0.98444
Value Standard Error
0.704 Intercept -1.14184 0.01703
0.704 Slope 0.49367 0.0102
Test3_70
L_H (mm)
time (s)
10
1
0.1
0.01
1
10
100

(c)

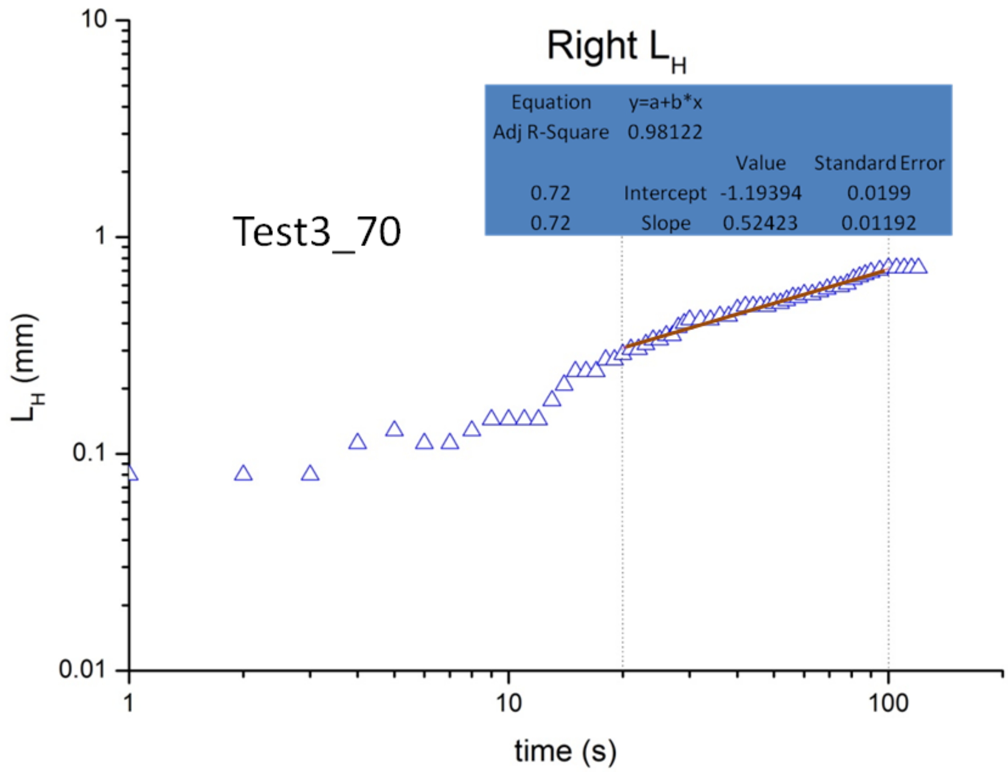

(d)

Figure 4. 3 Linear curve fit for Test3_70. (a) Left L_V (b) Right L_V (c) Left L_H (d) Right L_H

Figure 4.4 shows joint formation of all tests in logarithmic coordinates and Figure 4.5 presents the average joint formation of these tests in logarithmic coordinates. The power values (n) for all tests in 70 ppm test group are summarized in Table 4.1. (The uncertainty for each column is the sum of system uncertainty (STD) using ORIGINPRO 8[61] and standard deviation resulting from number of tests in the test group.)

Table 4.1 Summarized power values in 70 ppm test group

Note: LL_V = Left L_V, RL_V = Right L_V, LL_H = Left L_H, RL_H = Right L_H

70 ppm LL_V	n (20s - 100s)	70 ppm RL_V	n (20s - 100s)	70 ppm LL_H	n (20s - 100s)	70 ppm RL_H	n (20s - 100s)
Test1_70	0.501	Test1_70	0.513	Test1_70	0.449	Test1_70	0.427
STD	0.008	STD	0.009	STD	0.007	STD	0.009
Test2_70	0.571	Test2_70	0.611	Test2_70	0.598	Test2_70	0.607
STD	0.012	STD	0.009	STD	0.014	STD	0.014
Test3_70	0.502	Test3_70	0.539	Test3_70	0.494	Test3_70	0.524
STD	0.010	STD	0.008	STD	0.010	STD	0.012
Test4_70	0.888	Test4_70	0.909	Test4_70	0.841	Test4_70	0.829
STD	0.018	STD	0.020	STD	0.018	STD	0.014
Test5_70	0.508	Test5_70	0.467	Test5_70	0.492	Test5_70	0.501
STD	0.023	STD	0.019	STD	0.018	STD	0.021
Test6_70	0.618	Test6_70	0.568	Test6_70	0.581	Test6_70	0.571
STD	0.015	STD	0.011	STD	0.013	STD	0.010
Test7_70	0.562	Test7_70	0.463	Test7_70	0.495	Test7_70	0.445
STD	0.016	STD	0.014	STD	0.011	STD	0.007
Average	0.593	Average	0.582	Average	0.564	Average	0.558
Uncertainty	0.152	Uncertainty	0.167	Uncertainty	0.146	Uncertainty	0.148
Total Average Power	0.574 Including the outlier, Test4_70 0.525 Excluding Test4_70						
Uncertainty	0.167 Including the outlier, Test4_70 0.082 Excluding Test4_70						

From these figures, the development of formation can be divided into 3 phases:

(1) Initial Phase from 0 to 20s:

This phase indicates a larger scatter in the logarithmic representation. This is due to primarily:

a) the nature of the logarithmic coordinates that lead to the fine data density at first few seconds presented over large domain;

b) most likely inertia influence, as indicated in Ref. 7 (Note: an impact of gravity most likely would not be present because at initial stages the Bond number, a dimensionless number that decides the importance of surface tension force compared to gravity force. Assuming the density and surface tension of molten clad keep constant regardless of spreading time, at the start of joining process, the Bond number is small due to small joint area and later the number becomes larger due to the increase of joint. The Bond number that is associated with the equilibrium state is estimated to be 0.006 knowing that the surface tension, density of clad and joint cross section area being 849.1mN/m, 2407.2kg/m^3 and 0.2146 mm^2, respectively[64]. However, it is shown that gravity can be neglected on vertical evolution of joint formation and the smaller Bo number indicates less influence of the gravity.

c) measurement uncertainty results from a very small pixel changes and difficult to identify between two subsequent frames;

d) the presence of an initial small but not necessarily negligible clearance between vertical piece and substrate.

(2) 0.525 Power Law Phase from 20 to 100s:

This stage is dominated by capillary force which drives the spreading in both vertical and horizontal directions and a less dominant impact of viscous force. Joint formation in this stage is directly proportional to 0.525 (an average excluding the outlier, Test4_70, see Table 4.1) power of spreading time. The relationship between formation and spreading time is close to the Washburn type ($L \sim t^{1/2}$).[6] Note that surface of the sample is assumed to be smooth enough that the roughness was not considered in this study although we are aware of the impact from surface roughness on the interfacial energy between solid phase and liquid phase (not dominant).

(3) Asymptotic Phase from 100 to 120s:

The kinetics curves become flat and no significant joint evolution development is noticed beyond ~100s indicating the balance between all acting forces including the viscous force.

To eliminate the influence of individual test joint lengths so the trend can be further evaluated, both vertical and horizontal lengths are scaled by their respective maximum length, the corresponding vertical or horizontal length at the end of tests, maximum values from test to test, see Appendix 8, such that:

$$0 \leq L_V/L_{VM} \leq 1 \text{ and,}$$
$$0 \leq L_H/L_{HM} \leq 1$$

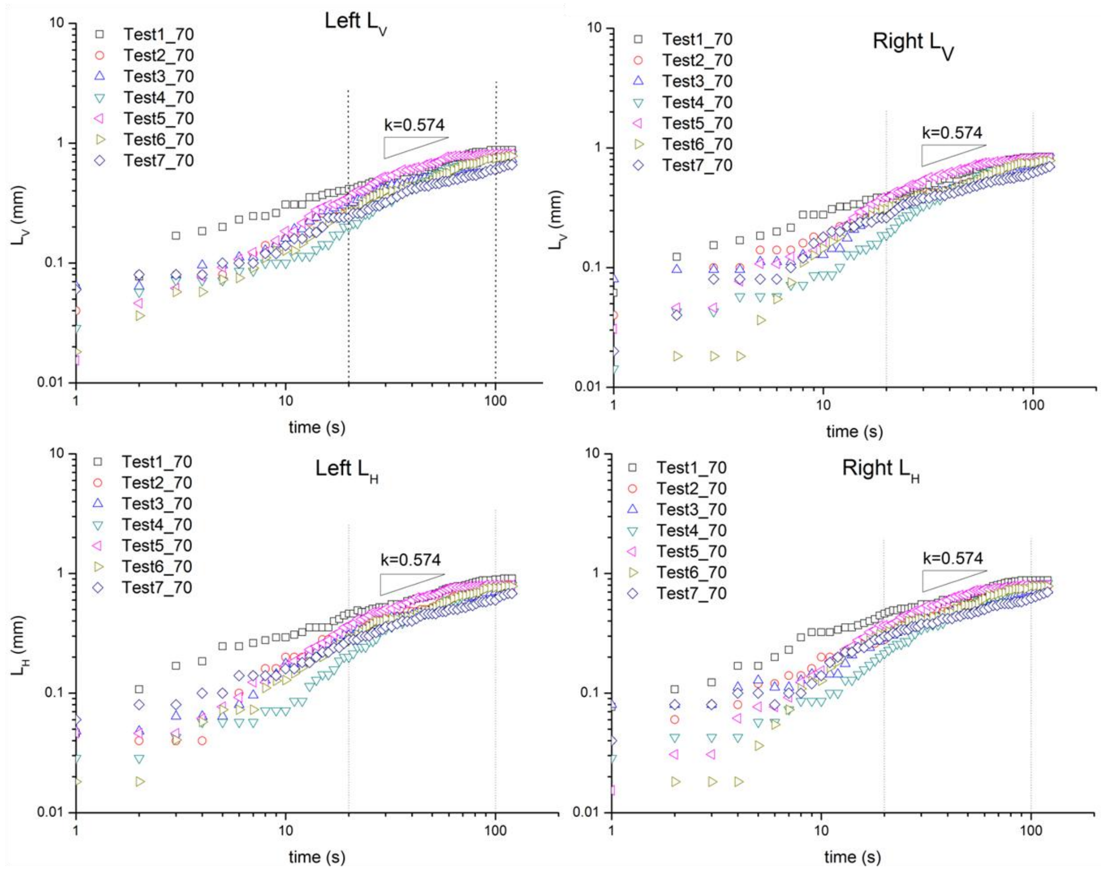

Figure 4. 4 Joint formation of Test1_70 to Test7_70 in Logarithmic Coordinates

Figure 4.6 shows normalized formations for all tests and Figure 4.7 shows average normalized length in logarithmic coordinates. The three stages of joint development can be identified. It is hypothesized that the discrepancies between tests are probably influenced by a slight initial condition difference, such as atmosphere condition and sample location within the hot zone. Nevertheless, the kinetic mechanism can be represented by unique model.

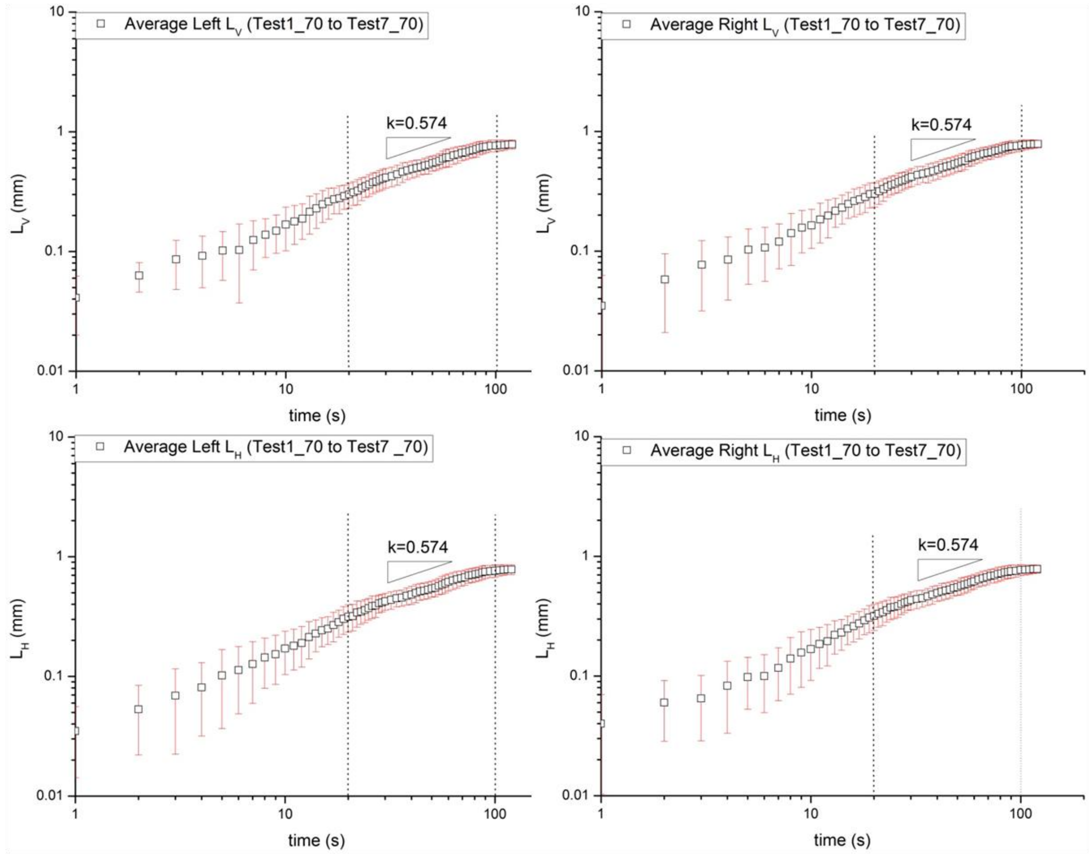

Figure 4. 5 Average joint formation kinetics curves of Test1_70 to Test7_70 in Logarithmic Coordinates

From Figure 4.4 and Figure 4.6, all the tests data agree well as far as the power law validity is concerned in Phase 2 and 3 except Test4_70, regardless the normalization. From Table 4.1, it is noted that the evolution rate of Test4_70 is faster than others. The reason is not known and must be investigated; still we decided to include this data set as an artifact of measurement. The overall slope representing joint evolution in phase 2 without the influence of Test4_40 is 0.525 ± 0.082.

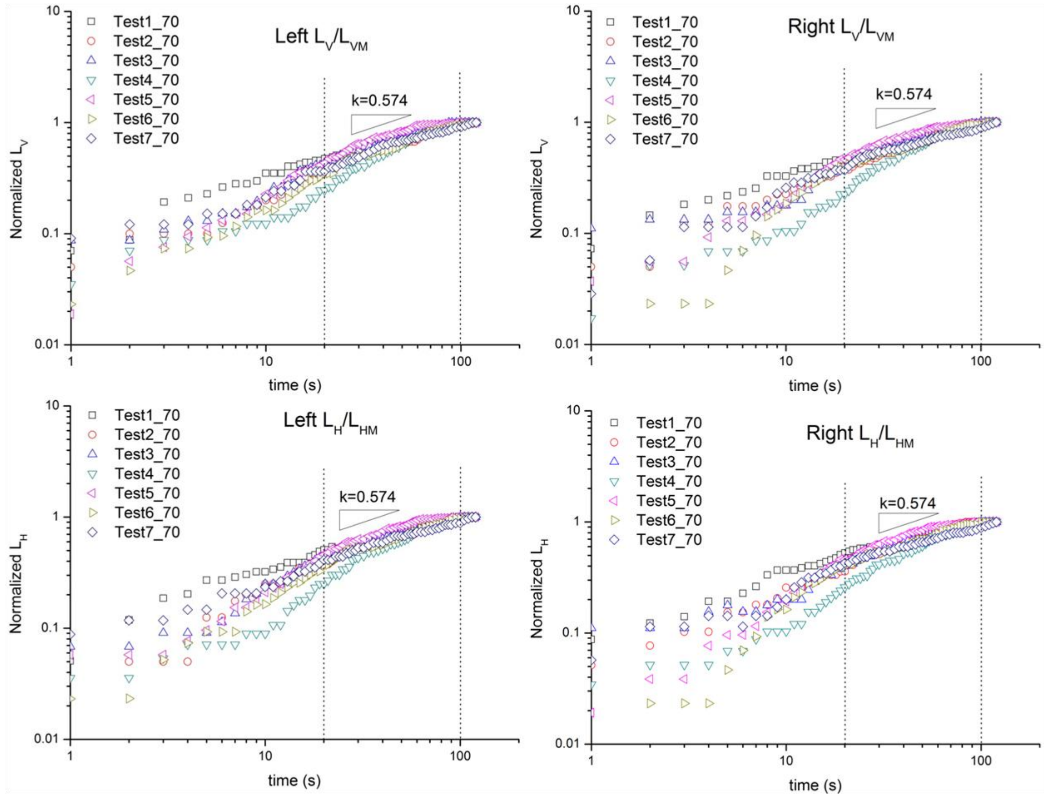

Figure 4. 6 Normalized joint formations in logarithmic coordinates

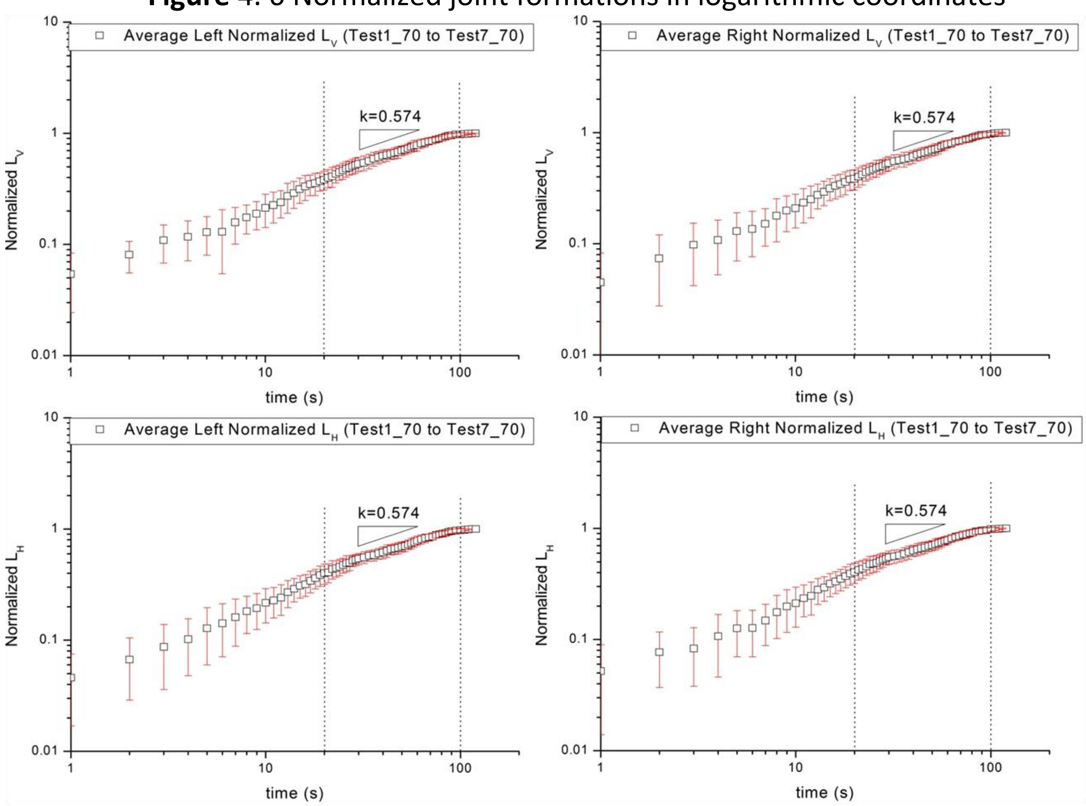

Figure 4. 7 Average normalized joint formations in logarithmic coordinates

A brazed sample from Test5_70 was randomly selected for further joint cross-section analysis. The distance between the brazing sheet lower surface and the clad/core interface is investigated for both pre-brazed and brazed samples to identify the by the liquid penetration caused movement of the interface (a partial aluminum core erosion during brazing[50,62]). Due to the nature of the brazing joining process, brazing with a brazing sheet (a horizontal mating surface in our tests) leads to clad melting in situ and surface tension driven flow of the formed liquid into the joint, leaving a residual clad. Any remaining liquid clad is re-solidified in situ, see the previous work of the UK Brazing laboratory.[50] The residual clad thickness is examined by using Image-Pro in order to establish the amount of clad that forms the joint. The measurement of the residue thickness is executed as follows: [for a more detailed discussion of this issue, see Reference 36.]

(1) The distance between the brazing sheet lower surface and the interface in the pre-brazed sample is measured, $\delta_{c,pb}$.

(2) The distance between the brazing sheet lower surface and the interface in the brazed sample is measured, $\delta_{c,b}$.

(3) The comparison between the value determined in (1) with that determined in (2) is performed to examine whether the core/clad interface has shifted.

$$\delta_{c,pb} > or < \ \delta_{c,b}$$

(4) The thickness of a brazed sample is measured, δ_b.

(5) The difference between the values in (4) and (2), $\delta_r = \delta_b - \delta_{c,b}$, leads to the clad residue thickness [if there is no significant difference between the value in (2) and (1)].

(6) The difference between the verified uniform clad thickness, δ_{clad}, in 3.1.2 (Table 3.1) and the value in (5) leads to the clad thickness that is available to form the joint.

$$\delta_{joint} = \delta_{clad} - \delta_r$$

Figure 4.8 shows the characteristic layers designations of pre-brazed and brazed sample.

The distances between the brazing sheet lower surface and interface from the clad uniformity test sample 1 (Table 3.1) and that from Test5_70 can be seen in Figure 4.9.

All the results are based on the measured pixel number. See the top left corner of the pictures for the linear physical scale.

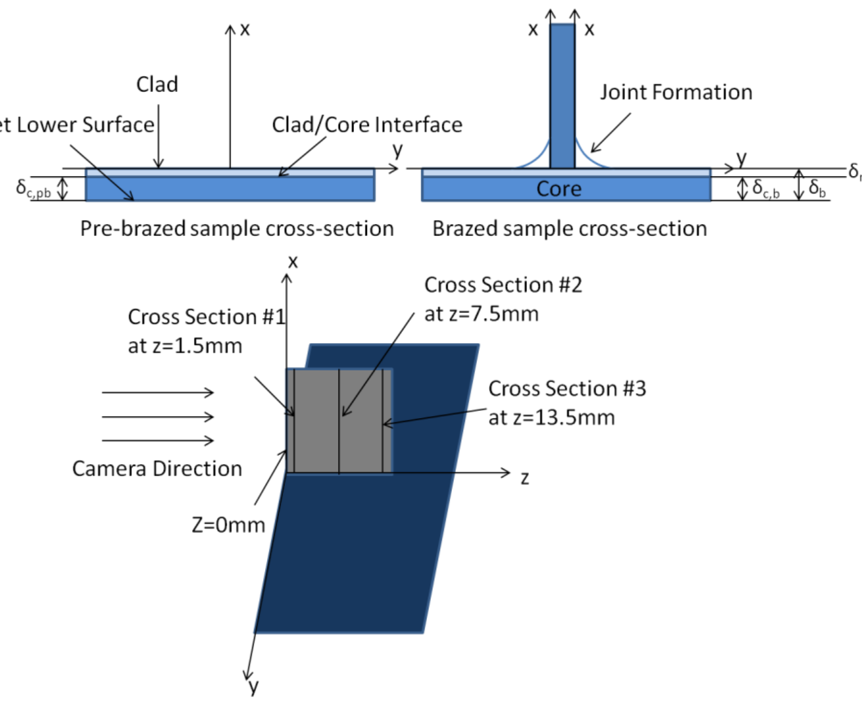

Figure 4. 8 Designation of brazing sample

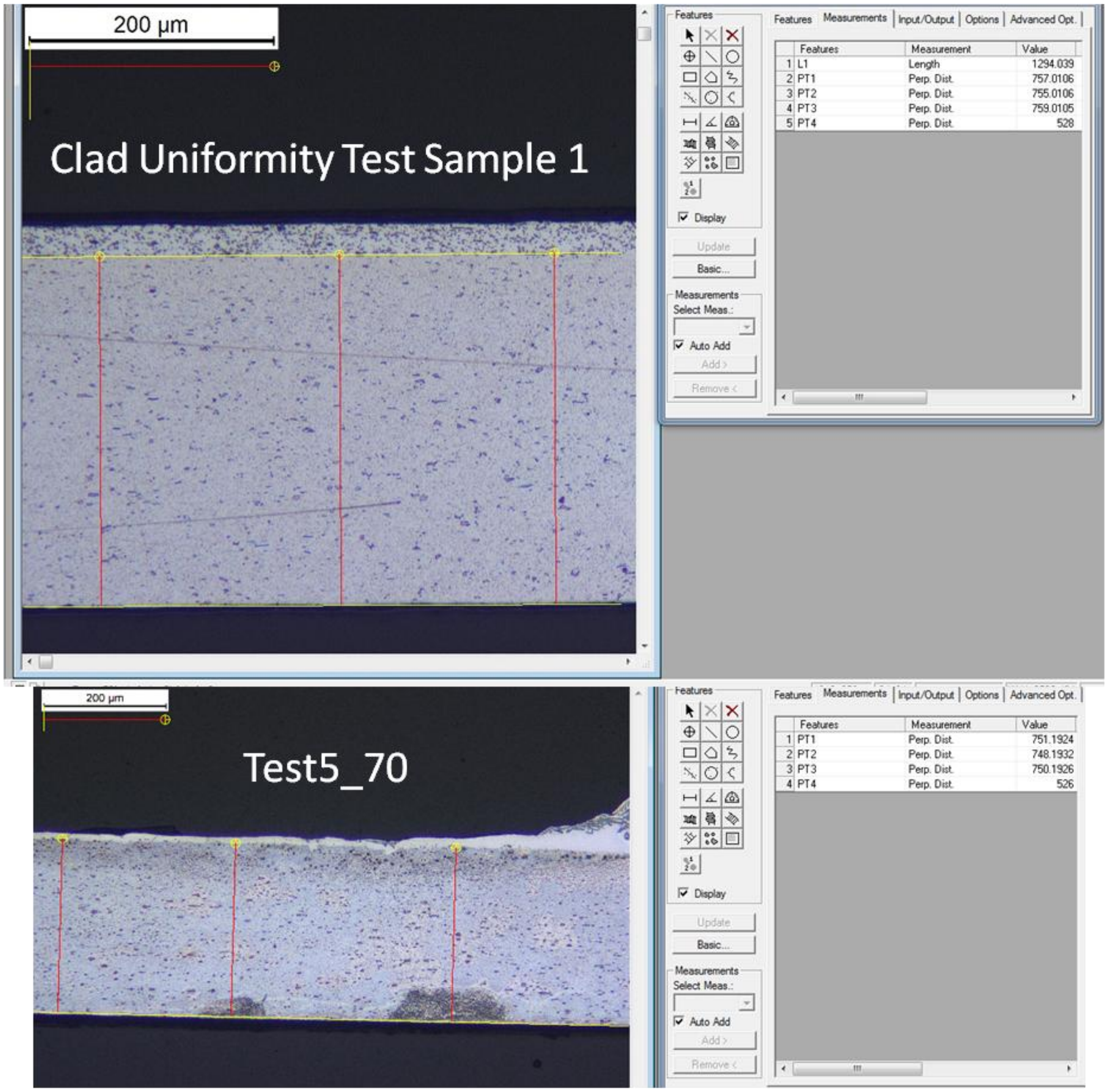

Figure 4. 9 Measurement of the distance between the brazing sheet lower surface and the interface in a pre-brazed and brazed samples near a joint

The average distance for a pre-brazed and 70 ppm tests brazed sample is 287 ± 1 µm and 285 ± 1 µm based on three measurements for each sample as can be seen in Figure 4.9, respectively. The difference is 2 µm with the uncertainty of ± 2 µm. Hence, it may be stated that there is in average no significant movement of interface. Therefore, the interface is assumed to be not significantly altered.

The brazed substrate cross-section (including the clad layer) is presented again in Figure 4.10, with markings indicating measurements of the substrate thickness.

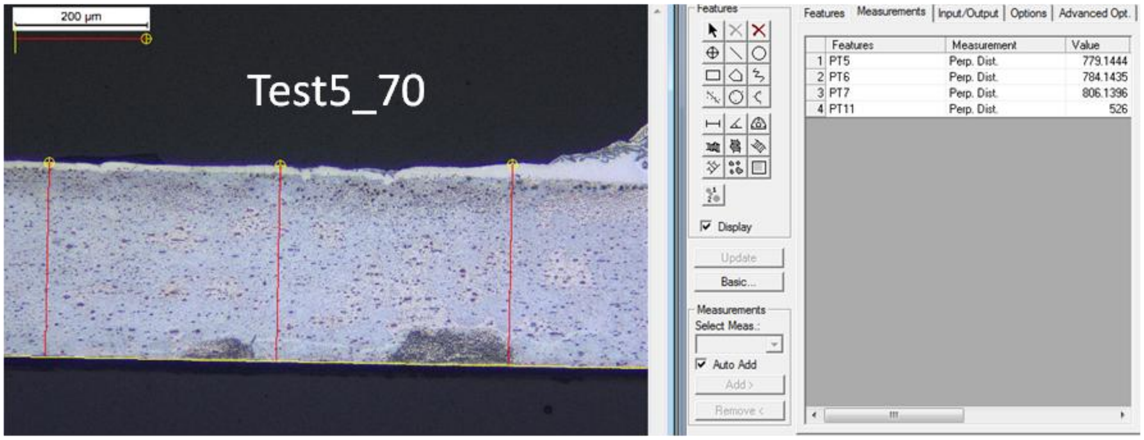

Figure 4. 10 Measurement of a brazed substrate thickness

The average brazed substrate thickness is 300 ± 5 μm. Therefore, the residual thickness is (300 ± 5) – (285 ± 1) = 15 ± 6 μm. Then the clad thickness that forms the joint is the difference of pre-brazed clad thickness from clad uniformity test 25 ± 1 μm and the residual thickness 15 ± 6 μm, 10 ± 7 μm.

Table 4.2 shows the results from each step mentioned earlier.

Table 4.2 Summarized measurements for residue thickness of Test5_70

70 ppm	Measurement (μm)	Comment	Note
step1	287 ± 1	Distance between the brazing sheet lower surface and the interface in the pre-brazed sample	Assumed to be the same for all tests
step2	285 ± 1	Distance between the brazing sheet lower surface and the interface in the brazed sample	
step3	2 ± 2	Absolute difference between measurements in step 1 and step 2	Interface assumed intact
step4	300 ± 5	The thickness of a brazed sample	
step5	15 ± 6	Clad residue thickness	
step6	10 ± 7	Clad thickness that is available to form the joint	

Figure 4.11 shows the core dissolution due to silicon diffusion across the interface in particular within the location of joint formation. Figure 4.12 provides three cross-section profiles at z=1.5 mm, 7.5 mm and 13.5 mm along the axial direction of the joint fillet, see Figure 4.8 for axes markings.

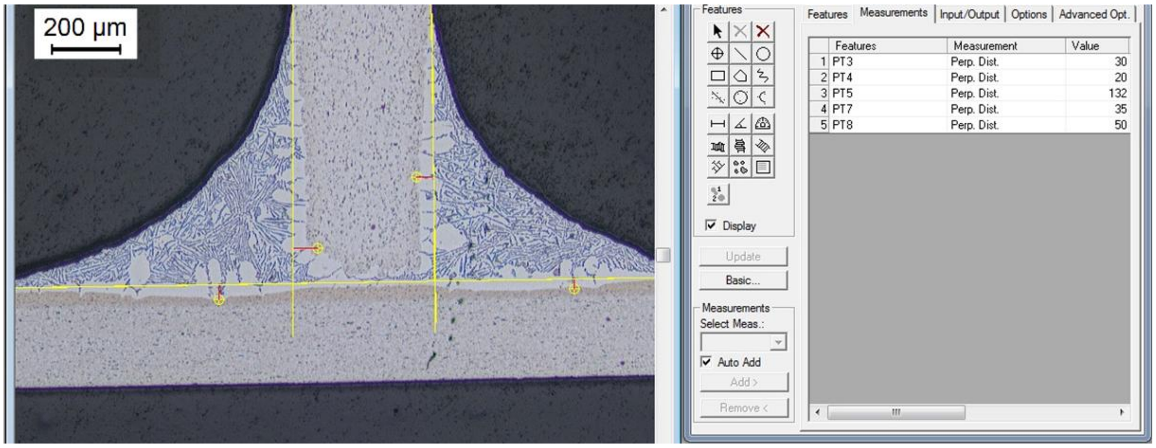

Figure 4. 11 Measurements of core dissolution for Test5_70

It is noted that the clearance between the substrate and vertical piece is fully filled with clad and no voids are visible. Aside from the clearance, at the left and right sides, the maximum dissolution depths of the horizontal piece from the original surface are 45 ± 1 μm and 30 ± 1 μm, respectively. At the left and right sides, the maximum diffusion depths of the vertical piece are 76 ± 1 μm and 53 ± 1 μm, respectively. It appears from Figure 4.11 that the average dissolution depth of vertical piece is larger than that of horizontal piece locally partially due to the fact that the clad layer originally existed on the substrate and solid state diffusion at the interface may be different, and partially due to the fact that molten clad has "climbed" the vertical piece over time so that dissolution close to the substrate is much more pronounced than away from the brazing sheet surface.

Note that all the auxiliary lines in Figures 4.12 are used for assisting the measurements of the triple line location.

The vertical and horizontal fillet joint's lengths measured at 3 locations are summarized in Table 4.3:

Table 4.3 Measured fillet formations at 3 locations along z axis (Figure 3.8 and Figure 4.8) for Test5_70 (mm)

70ppm	1.5 mm	7.5 mm	13.5 mm	Average	Std
Left L_V	0.883	0.912	0.939	0.911	0.028
Left L_H	0.874	0.894	0.848	0.872	0.023
Right L_V	0.898	0.958	0.920	0.925	0.030
Right L_H	0.821	0.918	0.882	0.874	0.049

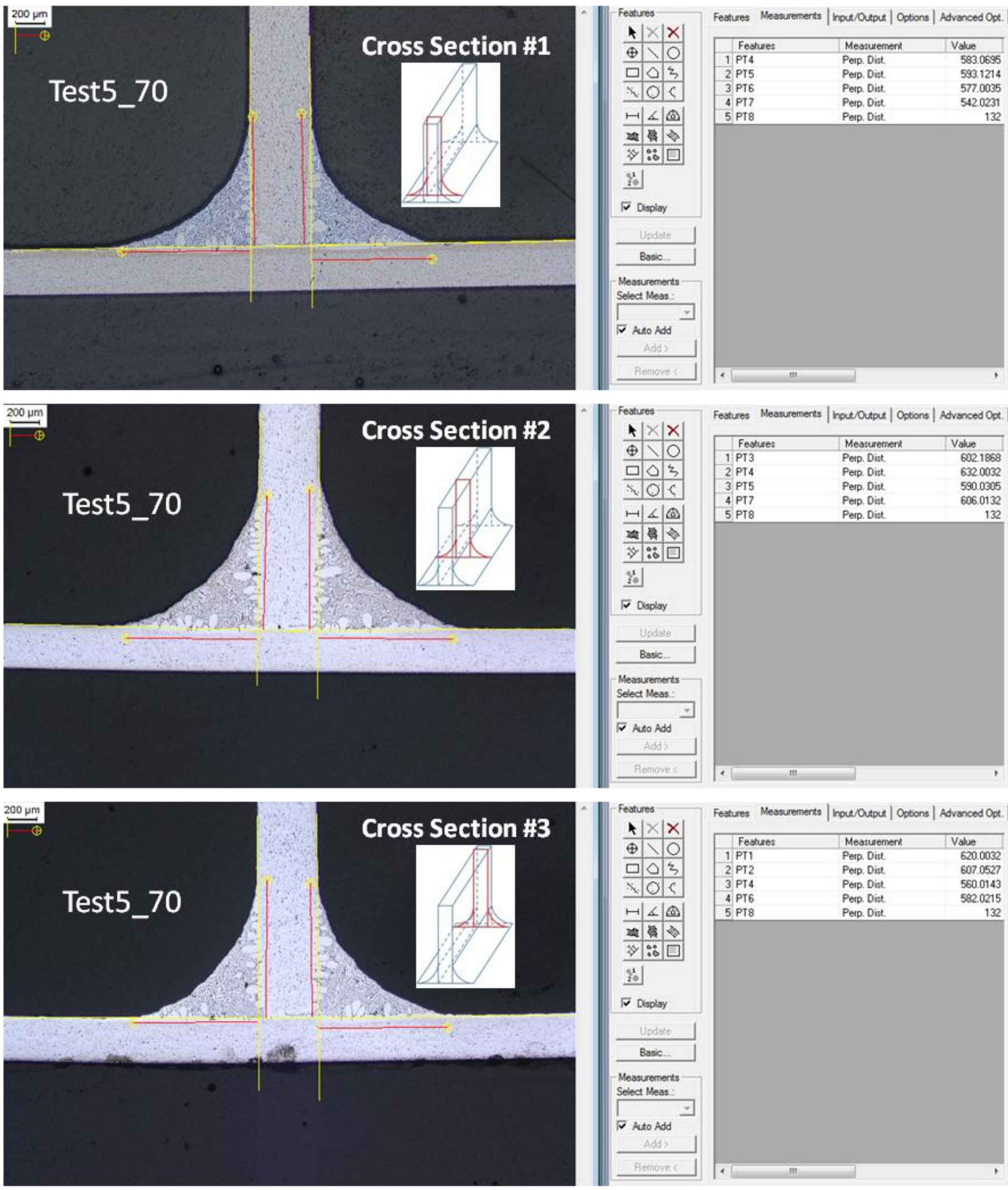

Figure 4. 12 Measurements of formation at 3 locations along the z axis for Test5_70

Hence, it can be validated that a 2-D joint formation under 70 ppm oxygen level condition is confirmed to a large degree. So, we postulate that the depth variation has negligible effect on the fillet cross-section profile. This statement is of particular importance for the level of optical sharpness of the fillet profile (a free surface of the fillet formed over time) that is reduced significantly if a cross-section of a joint changes along the z axis, Figure 4.8.

The equilibrium joint formations of Test5_70 measured using OCA units are:
Left L_V = 0.816 mm, Left L_H = 0.815 mm, Right L_V = 0.831 mm, Right L_H = 0.800 mm. (Appendix 8)

Since the camera of the OCA units is focused on the cross section that is at 0 mm along the z axis (i.e., closest to the observer) and the cross section at z=1.5 mm is close to the one at z=0 mm, the relative deviations for L_V and L_H at both sides are based on measurements at 1.5 mm from Table 4.1. (The deviation between OCA and micrographs measurements of the L value is determined as a relative difference between these values, L_{OCA} from Appendix 8 and L_{Micro} from Table 4.3)

Left: $\%L_V = \left|\frac{0.816-0.883}{0.883}\right| = 8\%, \ \%L_H = \left|\frac{0.800-0.874}{0.874}\right| = 8\%$

Right: $\%L_V = \left|\frac{0.831-0.898}{0.898}\right| = 9\%, \ \%L_H = \left|\frac{0.800-0.821}{0.821}\right| = 3\%$

These deviations are due to the following reasons:

(1) The shrinkage (liquid/solid) is not taken into consideration.

(2) The position of the sample in the chamber is not perfectly vertical or horizontal (90° ±1.5° between mating surfaces, see 3.1.1);

(3) The cross section measured using OCA (at z=0 mm) is not exactly the one polished (at z=1.5 mm)

(4) Sample configuration (See below for explanation)

The fillet formation's topographical metrics values, measured at the brazing sheet edge using OCA are smaller than those measured at three different locations along z axis. This implies that the sample configuration (See Figure 3.1 and Figure 3.2) has an influence on the joint formation (though small) at the edge area under 70 ppm condition.

4.2 200 ppm Group Results

Three tests in this group were performed with the same mating surfaces' configuration as for the 70 ppm group, but with a different oxygen level in the hot zone chamber, i.e., a high purity nitrogen with 200 ppm of oxygen. The kinetics data of the Test2_200 is plotted in Figure 4.13. Figure 4.14 shows the average triple line location with their associated error bars for all the three tests.

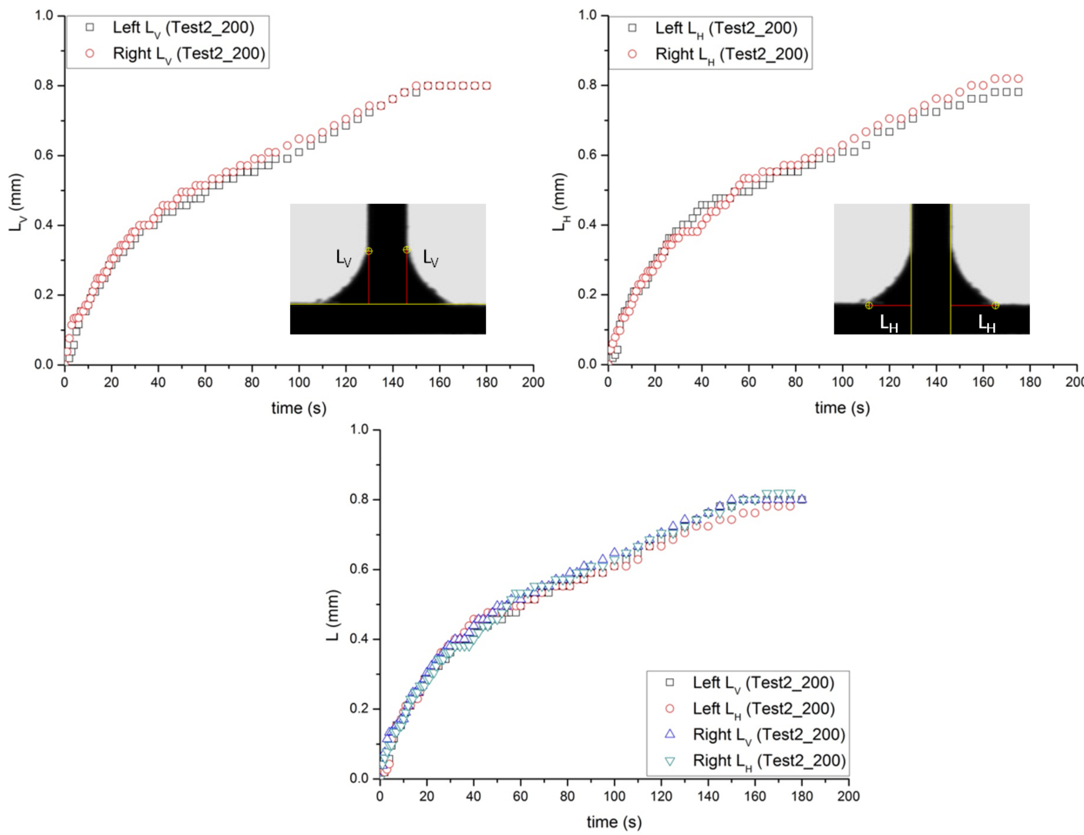

Figure 4. 13 Kinetics plot of Test2_200

Again, the maximum vertical and horizontal positions (the asymptotic location) of the triple line under 200 ppm condition are about 0.8 mm, which are virtually the same as under 70 ppm condition. However, under 200 ppm condition, it can be clearly observed that it takes ~160 seconds for the formation to be completed, 1 minute longer than under 70 ppm condition. This is, we hypothesize, due to the worse atmosphere condition (because all the other conditions were identical, i.e. uniform clad and temperature conditions). In addition, the individual trend of vertical and horizontal spreading is similar (Figure 4.13 and Figure 4.14) implying the gravity influence is insignificant.

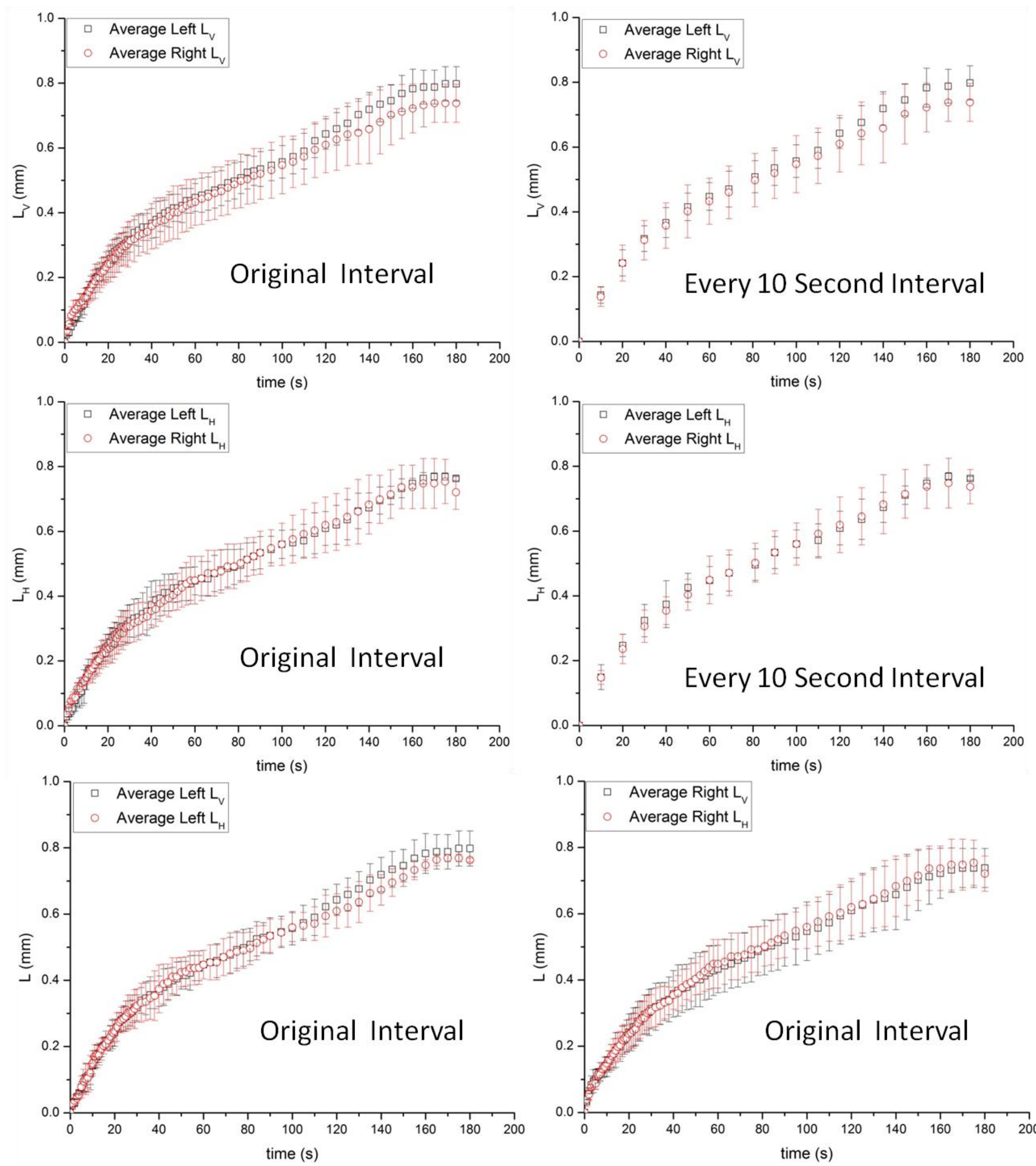

Figure 4. 14 Average kinetics of all tests in 200 ppm group

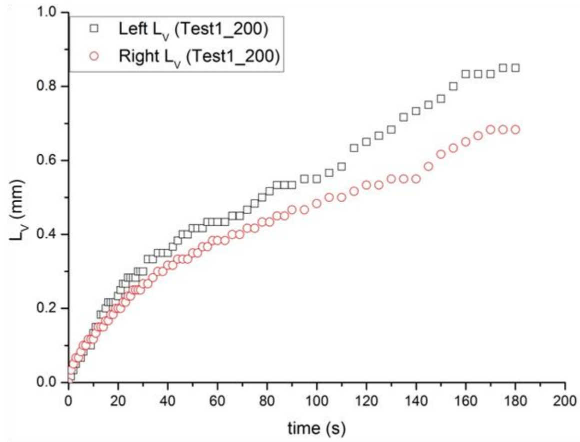

Figure 4. 15 Vertical triple line location evolution of Test1_200

It may be noted that in the Test1_200 (Figure 4.15) database an asymmetric spreading occurs along vertical direction leading to the two curves in the top left corner of Figure 4.14 not on top of each other after ~120 seconds. More tests in this group need to be performed to confirm whether slightly asymmetric spreading in vertical direction is accidentally random artifact or a consequence of the particular influential factor. However, regardless of this artifact, it is concluded that spreading under 200 ppm condition leads to the symmetric joint formation.

To investigate whether a power law relation between joint formation and spreading time exists under 200 ppm condition, the kinetic data were analyzed in logarithmic coordinates. Figure 4.16 shows the linear curve fit for Test2_200 and Figure 4.17 and Figure 4.18 present triple line location development for all the tests in 200 ppm test group, individual tests locations and average values, respectively. The power values (n) for Test1_200 through Test3_200 are summarized in Table 4.4.

Table 4. 4 Summarized power values for all the tests in 200 ppm test group

200 ppm LLv	n (15s - 160s)	200 ppm RLv	n (15s - 160s)	200 ppm LLH	n (15s - 160s)	200 ppm RLH	n (15s - 160s)
Test1_200	0.553	Test1_200	0.539	Test1_200	0.510	Test1_200	0.564
STD	0.008	STD	0.007	STD	0.008	STD	0.010
Test2_200	0.484	Test2_200	0.478	Test2_200	0.460	Test2_200	0.494
STD	0.006	STD	0.006	STD	0.010	STD	0.006
Test3_200	0.546	Test3_200	0.557	Test3_200	0.547	Test3_200	0.567
STD	0.007	STD	0.006	STD	0.006	STD	0.006
Average	0.528	Average	0.524	Average	0.506	Average	0.541
Uncertainty	0.045	Uncertainty	0.048	Uncertainty	0.052	Uncertainty	0.049
Total Average Power	0.525						
Uncertainty	0.052						

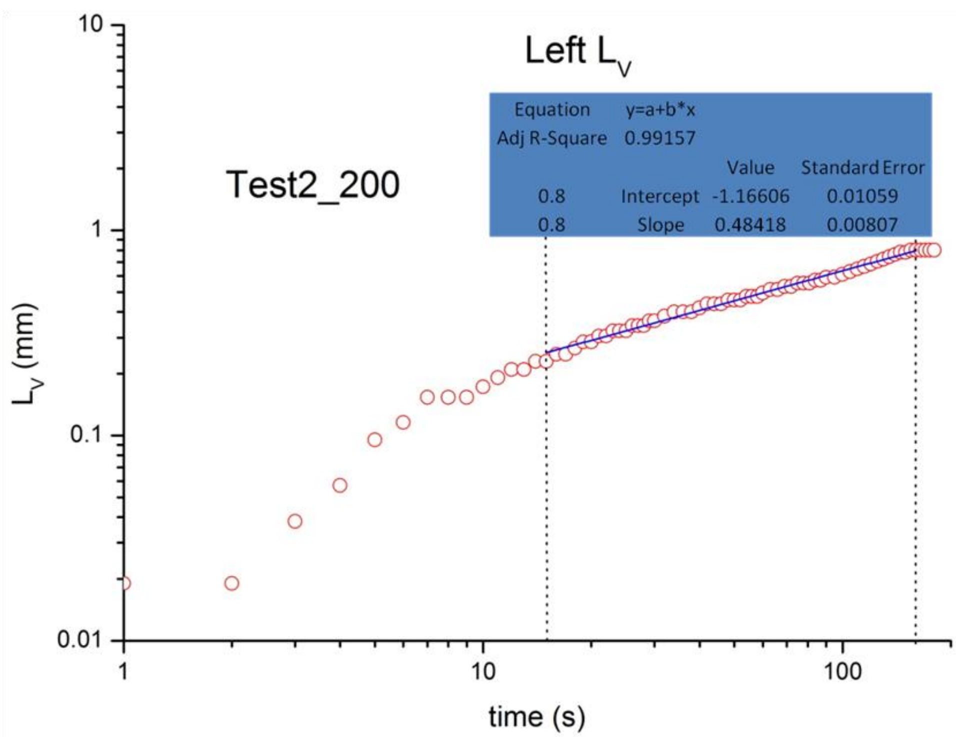

(a)

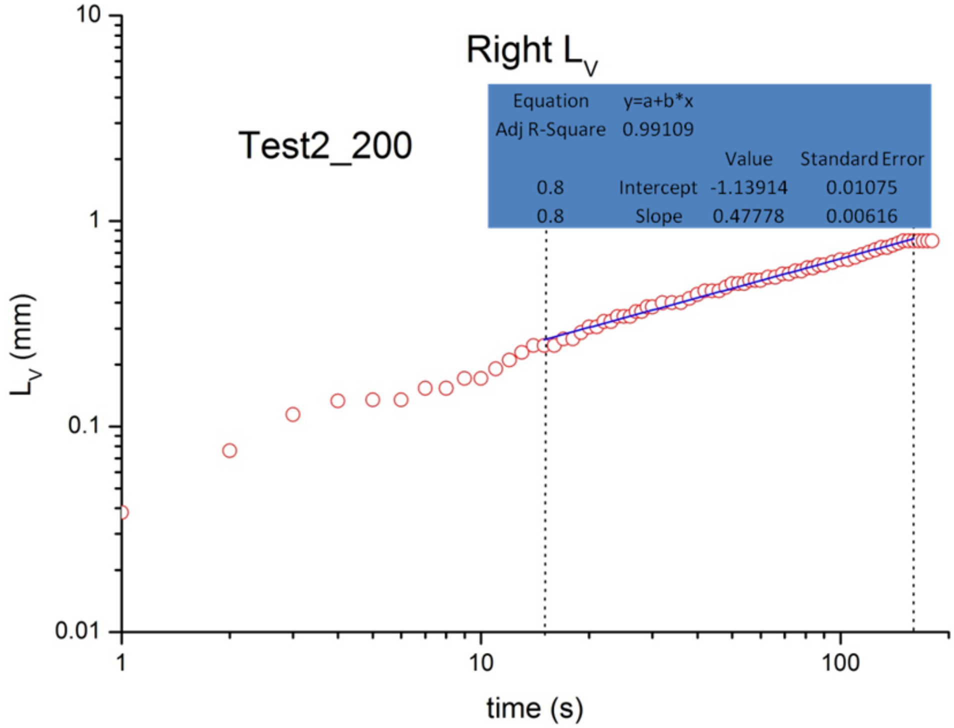
Right L_V
Test2_200
Equation y=a+b*x
Adj R-Square 0.99109
Value Standard Error
0.8 Intercept -1.13914 0.01075
0.8 Slope 0.47778 0.00616
L_V (mm)
time (s)
10
1
0.1
0.01
1
10
100

(b)

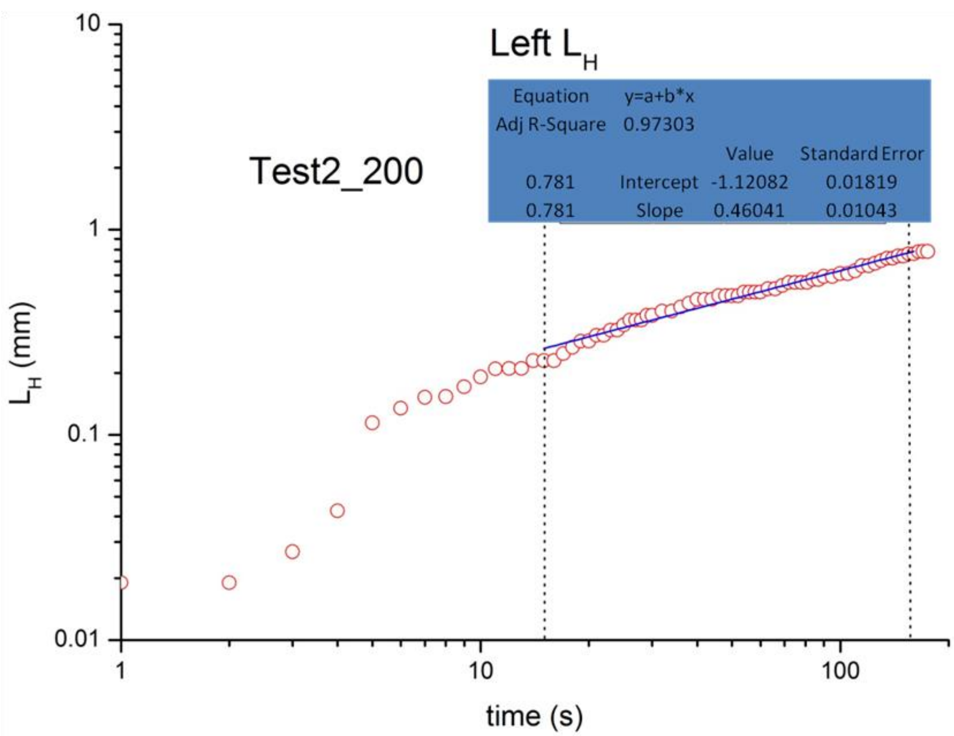
Left L_H
Test2_200
Equation y=a+b*x
Adj R-Square 0.97303
Value Standard Error
0.781 Intercept -1.12082 0.01819
0.781 Slope 0.46041 0.01043
L_H (mm)
time (s)
10
1
0.1
0.01
1
10
100

(c)

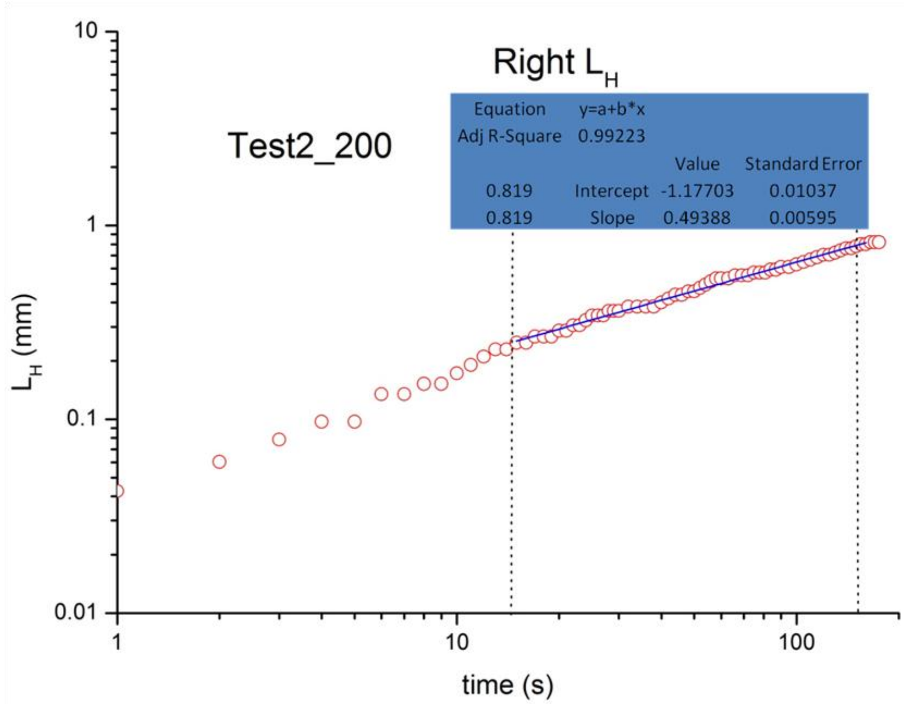

(d)

Figure 4. 16 Liner curve fit for Test2_200. (a) Left L_V (b) Right L_V (c) Left L_H (d) Right L_H

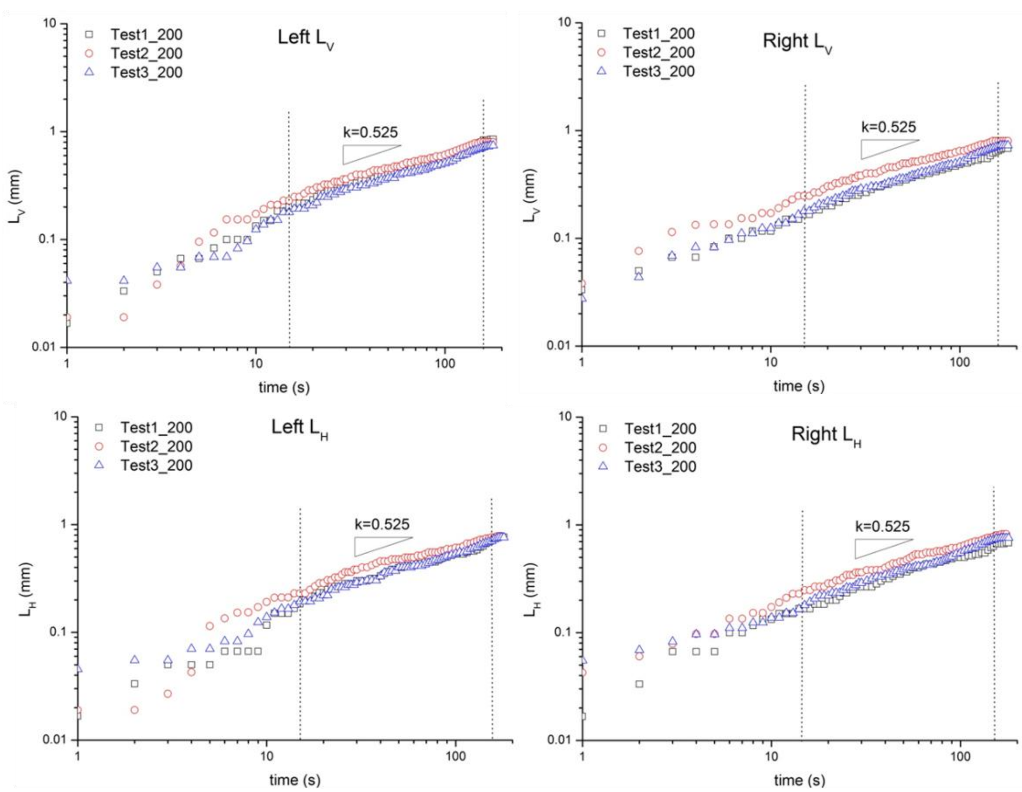

Figure 4. 17 Joint formations of Test1_200 to Test3_200 in Logarithmic coordinates

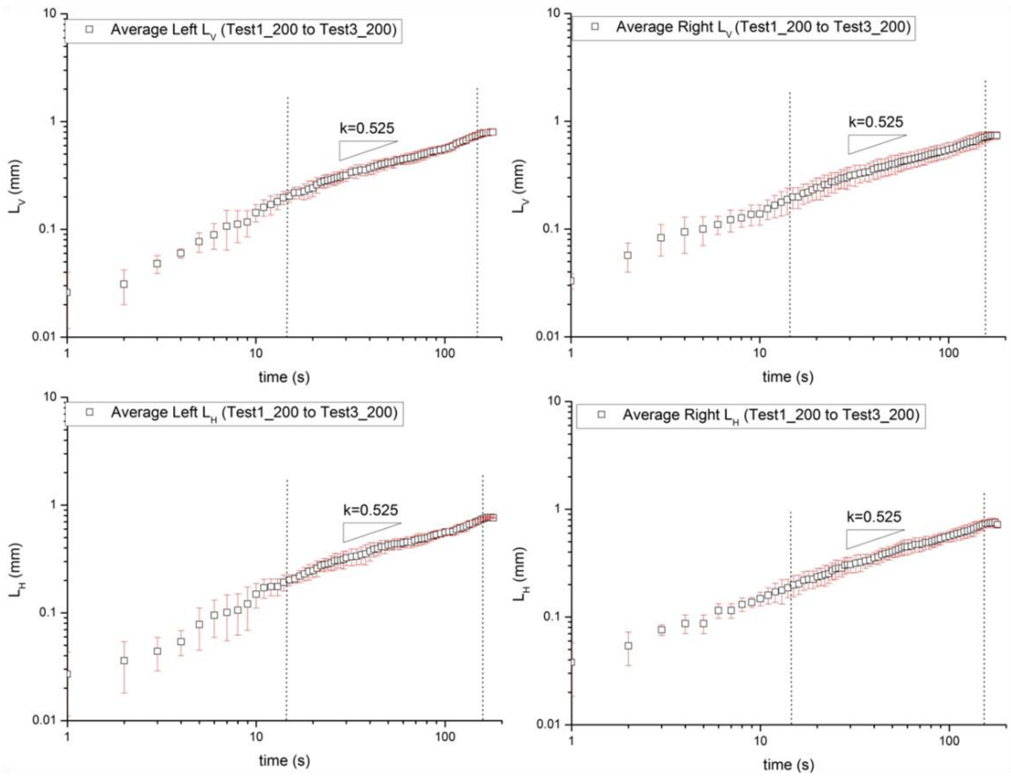

Figure 4. 18 Average Joint formation of Test1_200 to Test3_200 in logarithmic coordinates

From these figures, the development of formation under 200 ppm condition can also be divided into 3 phases as those for the 70 ppm group:

(1) Initial phase from 0 to 15s:

It is noted that compared to the same phase under the 70 ppm condition (20 seconds), the duration of this phase under 200 ppm condition (15 seconds) is 5 seconds shorter.

(2) 0.525 Power Law Phase from 15 to 160s:

The relationship between formation and spreading time is close to Washburn model ($L \sim t^{1/2}$). The power value (0.525) in this phase under 200 ppm condition is roughly the same as that under 70 ppm condition, without the influence of an outlier of Test4_70 (the average slope under 70 ppm condition is 0.525 , the same as that under 200 ppm condition!)

(3) Asymptotic phase from 160 to 180s.

Again, no obvious differences between vertical and horizontal triple line locations are noted (Figure 4.13 and Figure 4.14) in this phase. This implies that gravity has negligible impact on the formation under 200 ppm condition.

Figure 4.19 shows normalized formations for all tests and Figure 4.20 shows average normalized triple line locations in logarithmic coordinates under 200 ppm condition.

A brazed sample from Test2_200 was randomly selected for further analysis as described for a corresponding one under 70 ppm condition. Figure 4.21 shows the measurement of distance between the interface and bottom face of Test2_200.

The brazed substrate thickness (including the clad layer) is presented in Figure 4.22. Table 4.5 shows the measurements results from each step similar as those in Table 4.2.

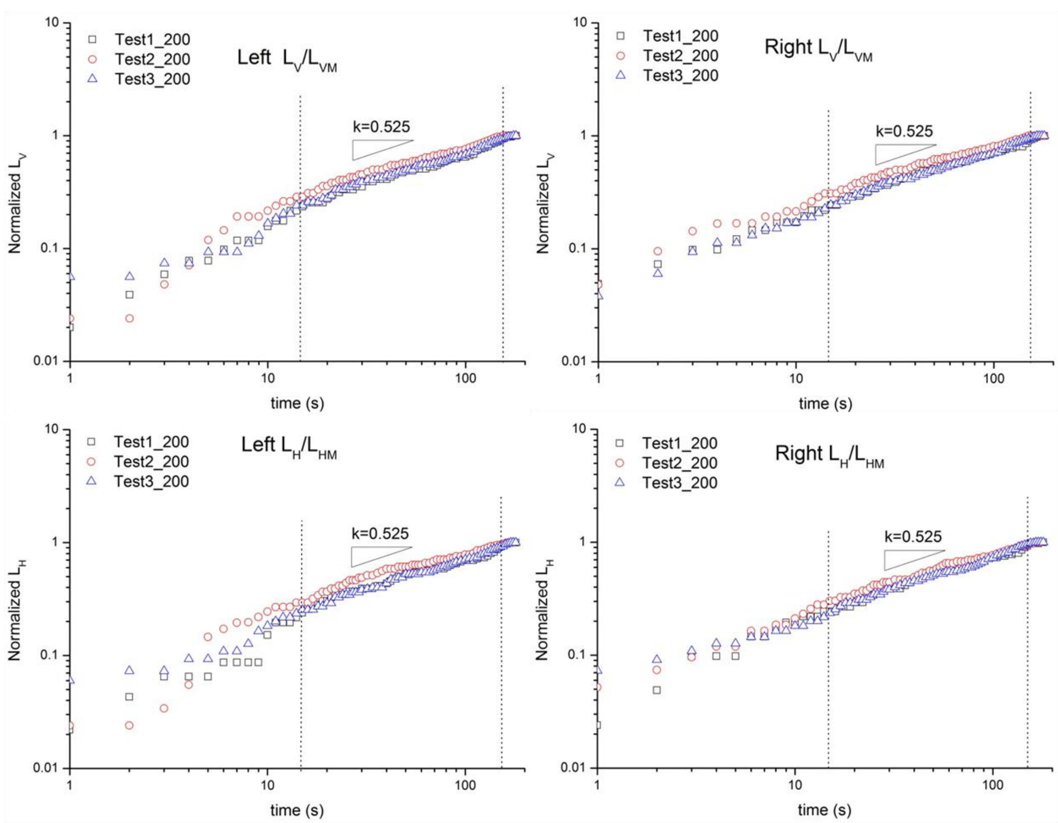

Figure 4. 19 Normalized joint formation of Test1_200 to Test3_200 in logarithmic coordinates

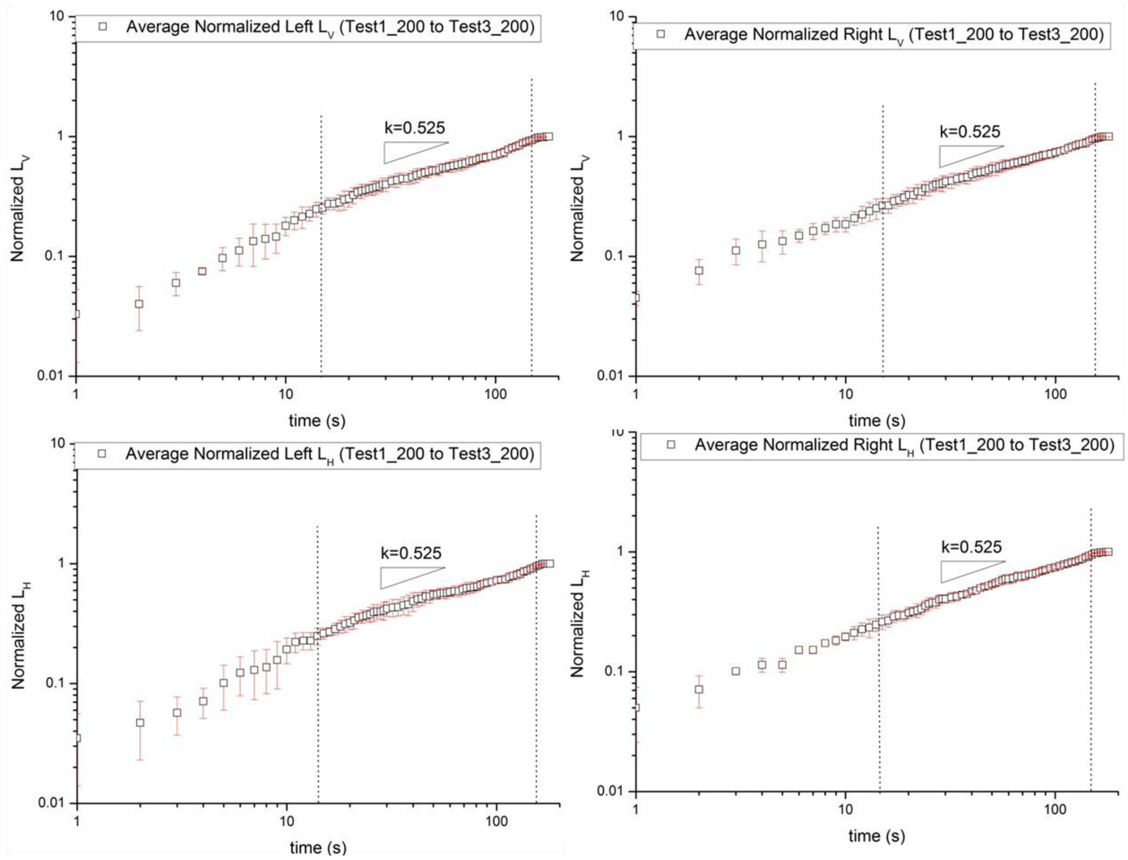

Figure 4. 20 Average normalized formation of Test1_200 to Test3_200 in logarithmic coordinates

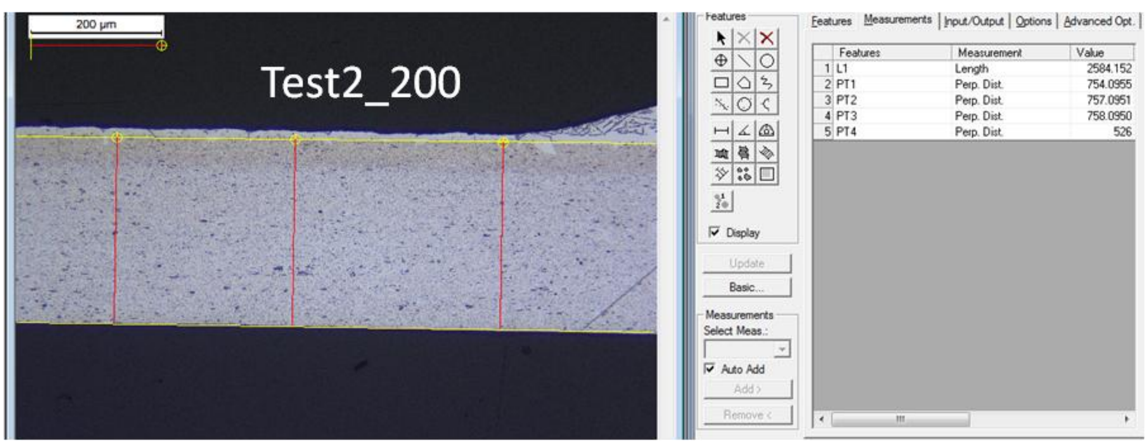

Figure 4. 21 Measurement of the distance between the brazing sheet lower surface and the clad/core interface of a brazed sample (Test2_200) near the joint area (to the right)

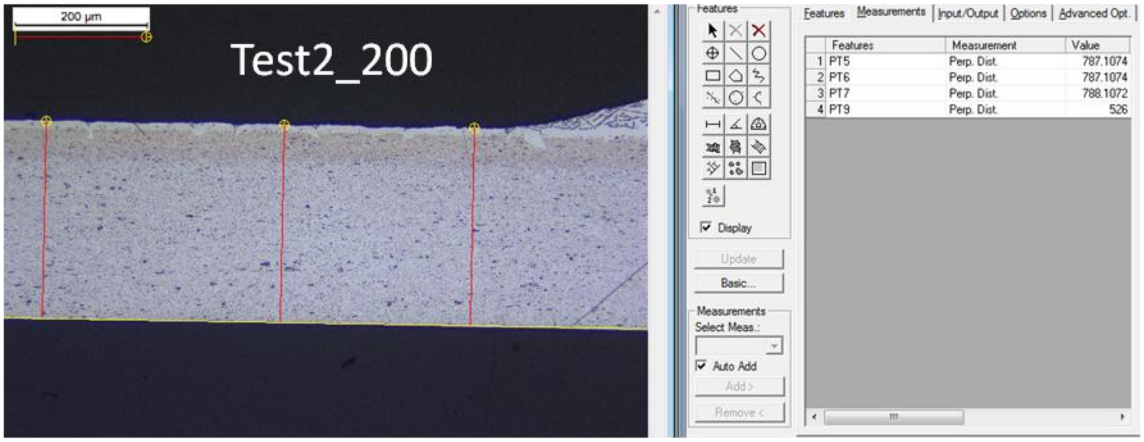

Figure 4. 22 Measurement of brazed sample thickness (Test2_200)

Table 4.5 Summarized measurements for residue thickness for Test2_200

200 ppm	Measurement (µm)	Comment	Note
step1	287 ± 1	Distance between the brazing sheet lower surface and the interface in the pre-brazed sample	Assumed to be the same for all tests
step2	288 ± 1	Distance between the brazing sheet lower surface and the interface in the brazed sample	
step3	1 ± 2	Absolute difference between measurements in step 1 and step 2	Interface assumed intact
step4	300 ± 1	The thickness of a brazed sample	
step5	12 ± 2	Clad residue thickness	
step6	13 ± 3	Clad thickness that is available to form the joint	

Figure 4.23 shows the minor core dissolution due to silicon diffusion in the joint over horizontal substrate for joint formation in brazed Test2_200. Note that the dissolution is significant for the vertical surface.

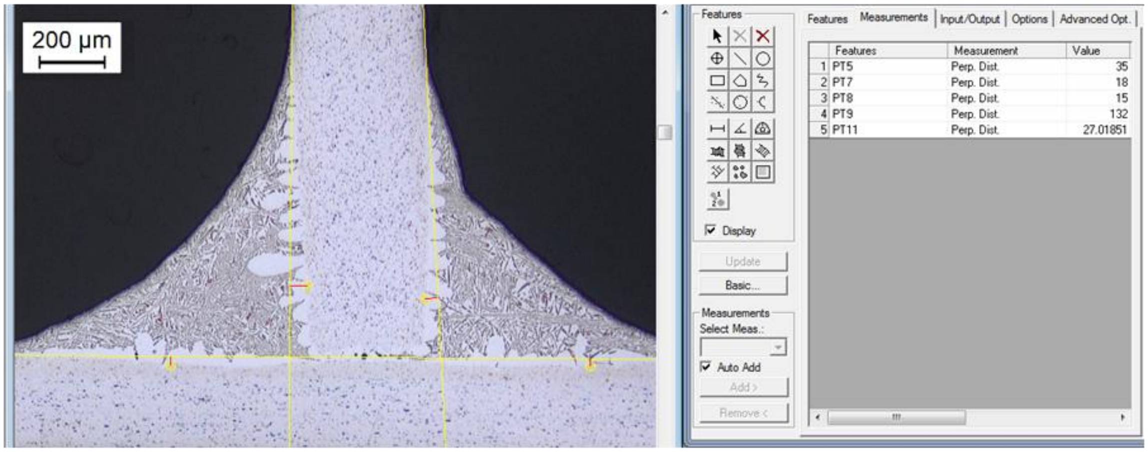

Figure 4. 23 Measurements of core dissolution (Test2_200)

The clearance between the substrate and vertical piece is fully filled with clad. At the left and right sides, the maximum dissolution depths of the horizontal piece from the original surface are 27 ± 1 µm and 23 ± 1 µm, respectively. The maximum diffusion depths of the vertical piece are sizably larger, i.e., 53 ± 1 µm and 41 ± 1µm, respectively.

Figure 4.24 provides three cross-section profiles at z=1.5 mm, 7.5 mm and 13.5 mm along the z axis of the joint fillet (Figure 4.8) for Test2_200.

The vertical and horizontal lengths measured at 3 locations are summarized in Table 4.6.

Hence, it can be validated that a 2-D joint formation under 200 ppm oxygen level condition is also preserved. The location along the z axis (along the joint fillet) has minimal effect on the cross-section size of the fillet.

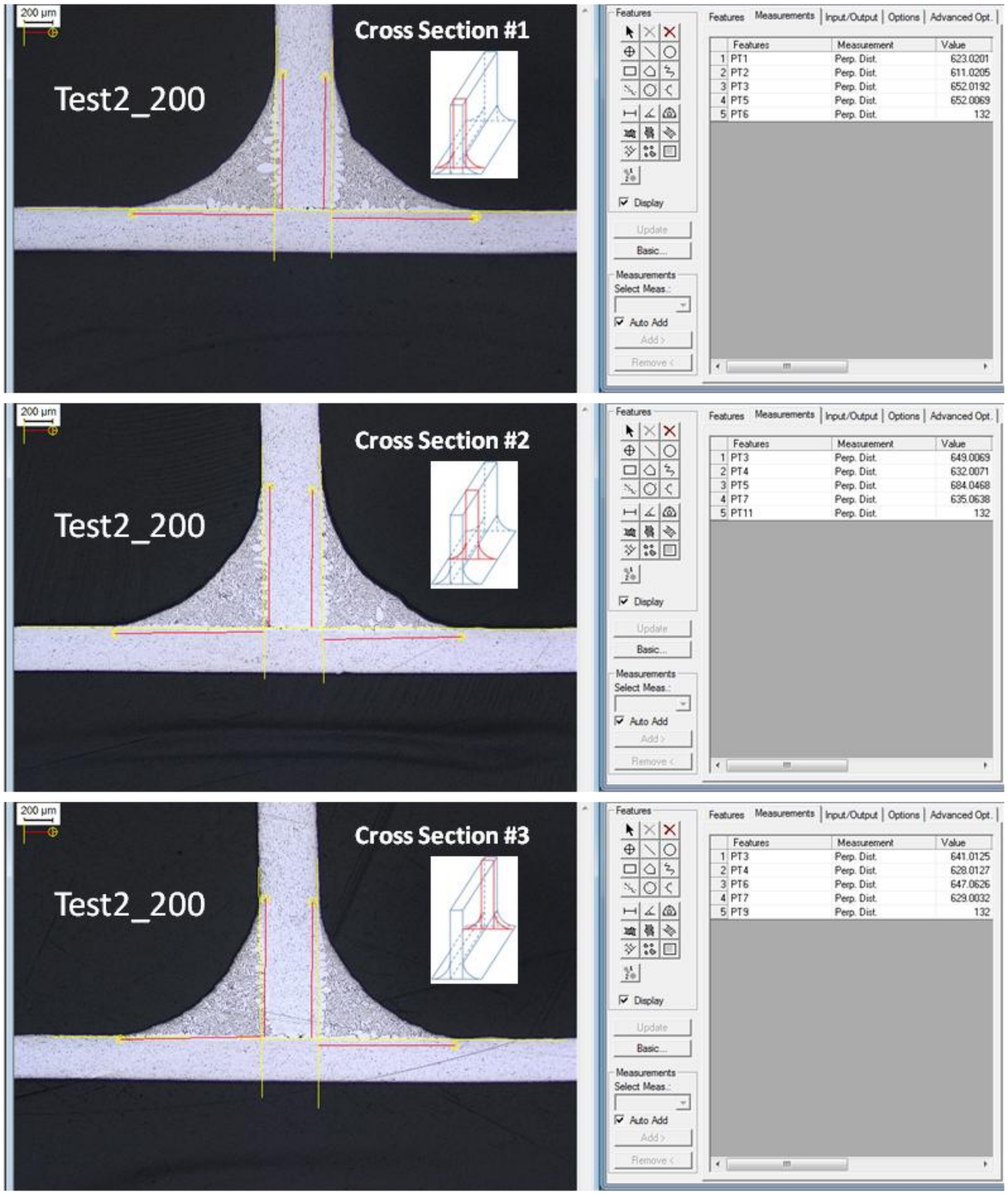

Figure 4. 24 Measurements of formation at 3 locations along the z axis (Test2_200)

Table 4.6 Measured fillet formations at 3 locations along the z axis (mm)

200ppm	1.5 mm	7.5 mm	13.5 mm	Average	Std
Left L_V	0.944	0.983	0.971	0.966	0.020
Left L_H	0.988	1.036	0.980	1.001	0.030
Right L_V	0.926	0.956	0.952	0.945	0.016
Right L_H	0.988	0.962	0.953	0.968	0.018

The equilibrium joint fillet formations of Test2_200 measured by OCA units are:

Left L_V = 0.800 mm, Left L_H = 0.781 mm, Right L_V = 0.800 mm, Right L_H = 0.819 mm. (Appendix 8)

The relative deviations in measurements under the 200 ppm condition are:

Left: $\%L_V = \left|\frac{0.800-0.944}{0.944}\right| = 15\%,\ \%L_H = \left|\frac{0.781-0.988}{0.988}\right| = 21\%$

Right: $\%L_V = \left|\frac{0.800-0.926}{0.926}\right| = 14\%,\ \%L_H = \left|\frac{0.819-0.988}{0.988}\right| = 17\%$

The relative deviations are larger compared to those under the 70 ppm condition. Hence, the edge influence may be considered. It appears that a deterioration of the conditions for facilitating clad flow may offer less liquid into the zone of the joint that receives liquid only from one side (along the joint formation).

4.3 500 ppm Group Results

Three experiments in this group were performed with the same configurations as for the 70 ppm and 200 ppm groups but with a different oxygen level in the chamber (at the level of 500 ppm). The kinetics data of Test2_500 is plotted in Figure 4.25. Figure 4.26 shows the average lengths with their associated error bars for all the three tests.

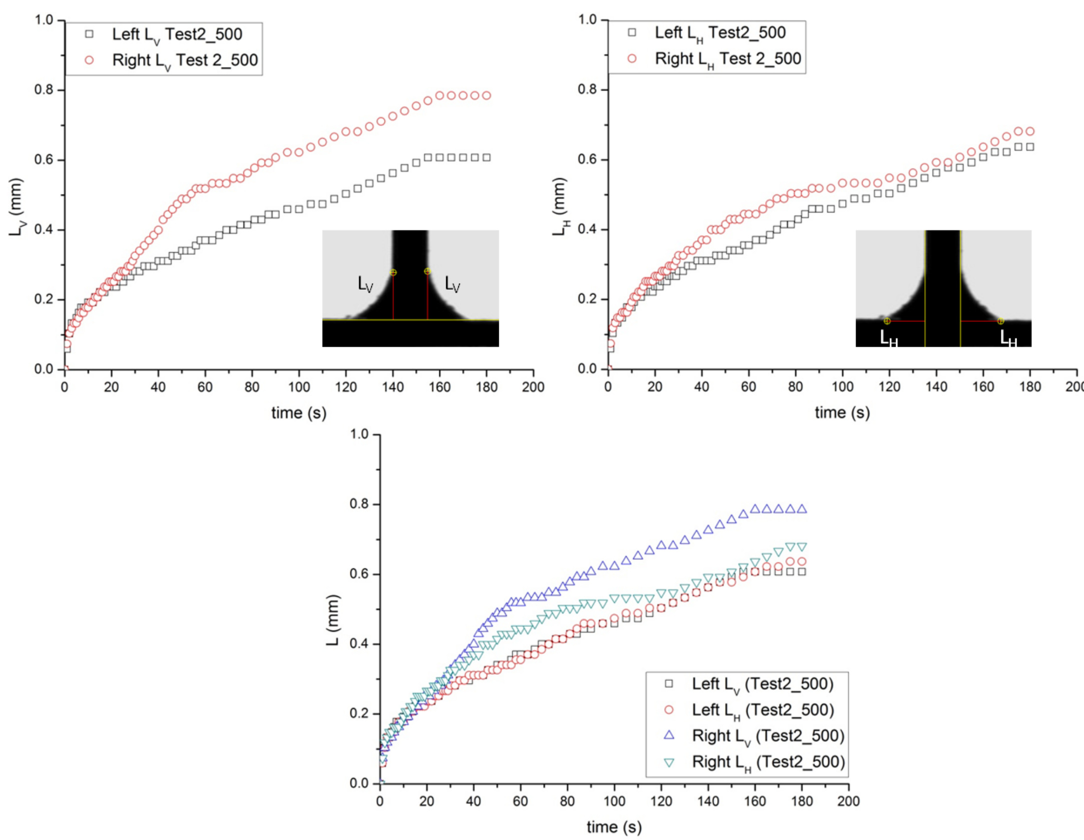

Figure 4. 25 Kinetics plot of Test2_500

Under 500 ppm condition, it takes ~160 seconds for the joint formation to evolve into the ultimate equilibrium state, virtually the same duration as under 200 ppm condition. It may be speculated that 200 ppm and 500 ppm are still too close to each other to cause a significant change in the triple line evolution, as opposed to 70 ppm case. In addition, it can be clearly seen in Figure 4.25 and Figure 4.26 that the joining process features filling the joint fillet differently at the two sides at the vertical mating surface, i.e., the joint is asymmetric (a significant triple line variation on left vs. right side, both along the vertical and the horizontal directions.

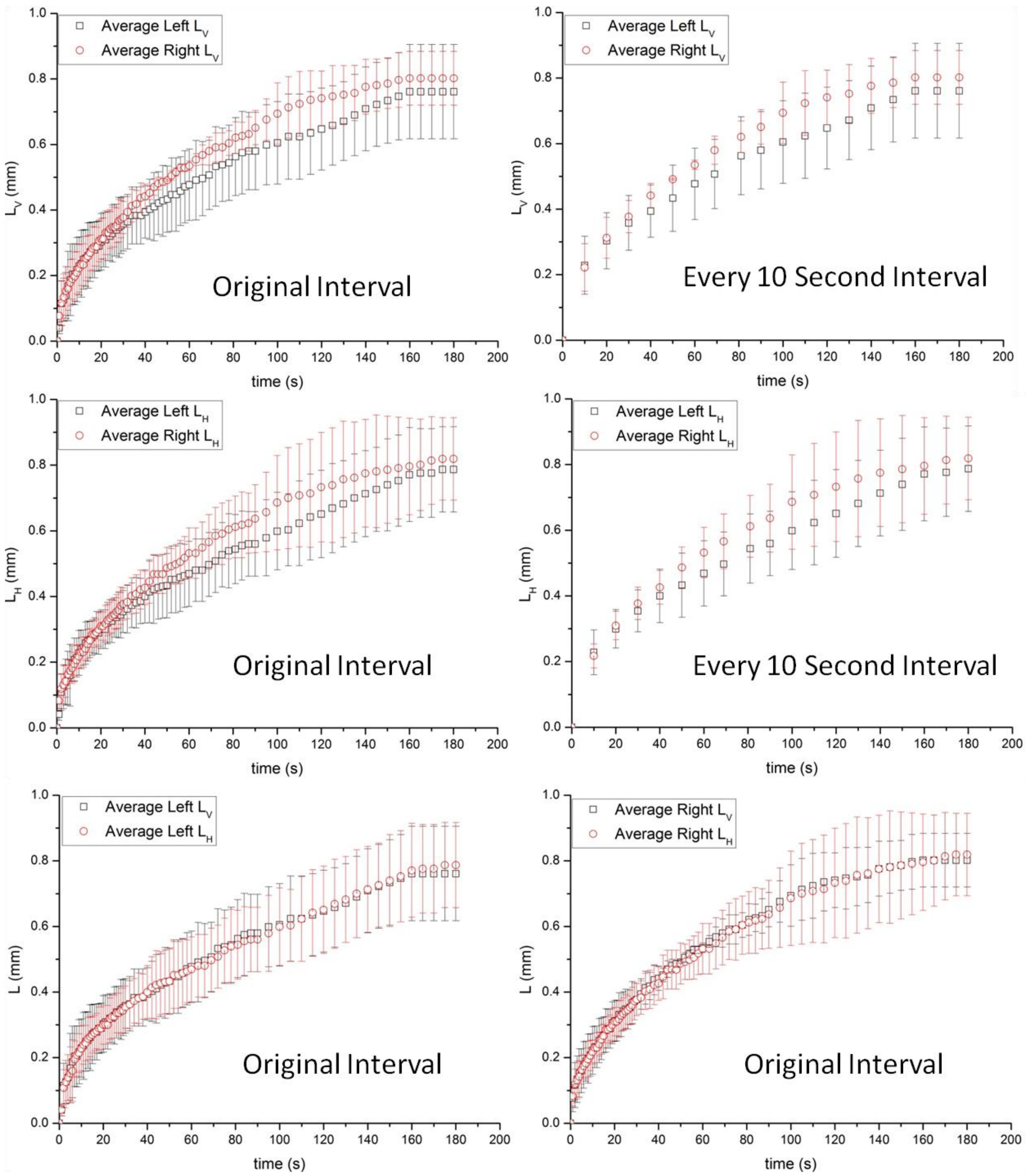

Figure 4. 26 Average kinetic data of all tests in the 500 ppm group

As indicated, both 200 ppm and 500 ppm hot zone chamber conditions result in a 160 seconds of the development of the joint formation, sizably longer than what is observed under 70 ppm condition. So, as hypothesized earlier, it is expected that a worse atmosphere condition brings an impact on the joint formation that results in a larger joint evolution time. In support of that hypothesis, it is indicated that 500 ppm condition not only leads to a longer formation development but also results to an asymmetric joint formation. To investigate whether a power law relation between joint formation and spreading time exists under 500 ppm condition, kinetic data were analyzed in logarithmic coordinates. Figure 4.27 shows the linear curve fit for Test2_500 within the surface tension-viscosity phase, and Figure 4.28 and Figure 4.29 provide the triple line location development for all the tests in 500 ppm test group. The power values (n) for Test1_500 through Test3_500 are summarized in Table 4.7.

Table 4.7 Summarized power values for all the tests in 500 ppm test group

500 ppm LL_V	Power (20s - 160s)	500 ppm RL_V	Power (20s - 160s)	500 ppm LL_H	Power (20s - 160s)	500 ppm RL_H	Power (20s - 160s)
Test1_500	0.522	Test1_500	0.536	Test1_500	0.506	Test1_500	0.564
STD	0.009	STD	0.008	STD	0.008	STD	0.007
Test2_500	0.449	Test2_500	0.543	Test2_500	0.453	Test2_500	0.416
STD	0.006	STD	0.013	STD	0.007	STD	0.008
Test3_500	0.375	Test3_500	0.346	Test3_500	0.387	Test3_500	0.434
STD	0.006	STD	0.005	STD	0.012	STD	0.005
Average	0.449	Average	0.475	Average	0.448	Average	0.472
Uncertainty	0.080	Uncertainty	0.120	Uncertainty	0.068	Uncertainty	0.088
Total Average Power	0.463						
Uncertainty	0.120						

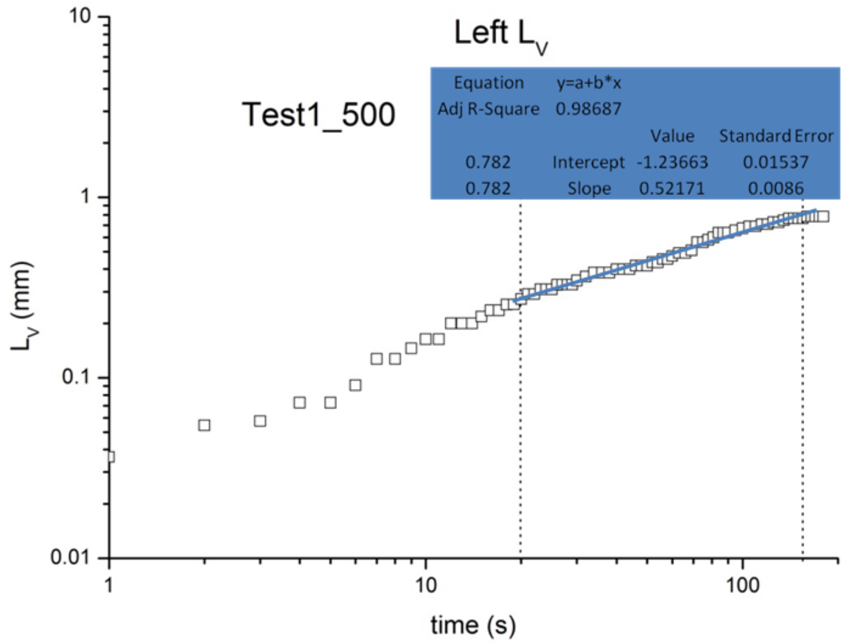
Left L_V
Test1_500
Equation y=a+b*x
Adj R-Square 0.98687
Value Standard Error
0.782 Intercept -1.23663 0.01537
0.782 Slope 0.52171 0.0086
L_V (mm)
time (s)
10
1
0.1
0.01
1
10
100

(a)

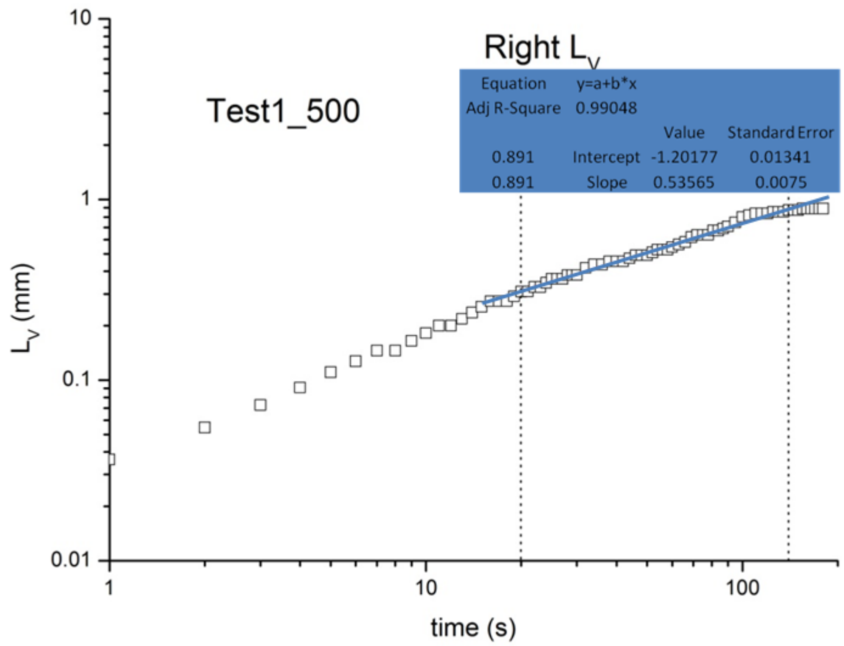
Right L_V
Test1_500
Equation y=a+b*x
Adj R-Square 0.99048
Value Standard Error
0.891 Intercept -1.20177 0.01341
0.891 Slope 0.53565 0.0075
L_V (mm)
time (s)
10
1
0.1
0.01
1
10
100

(b)

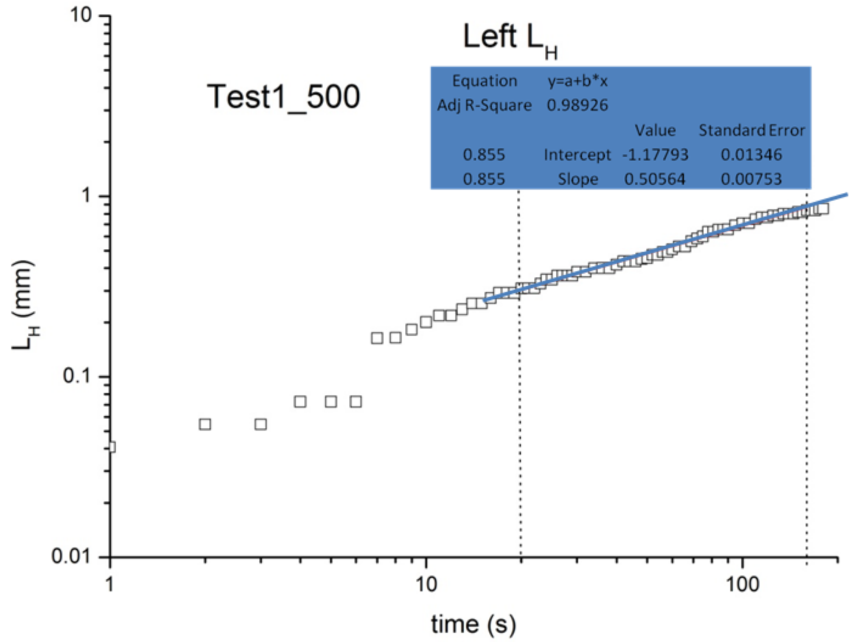

(c)

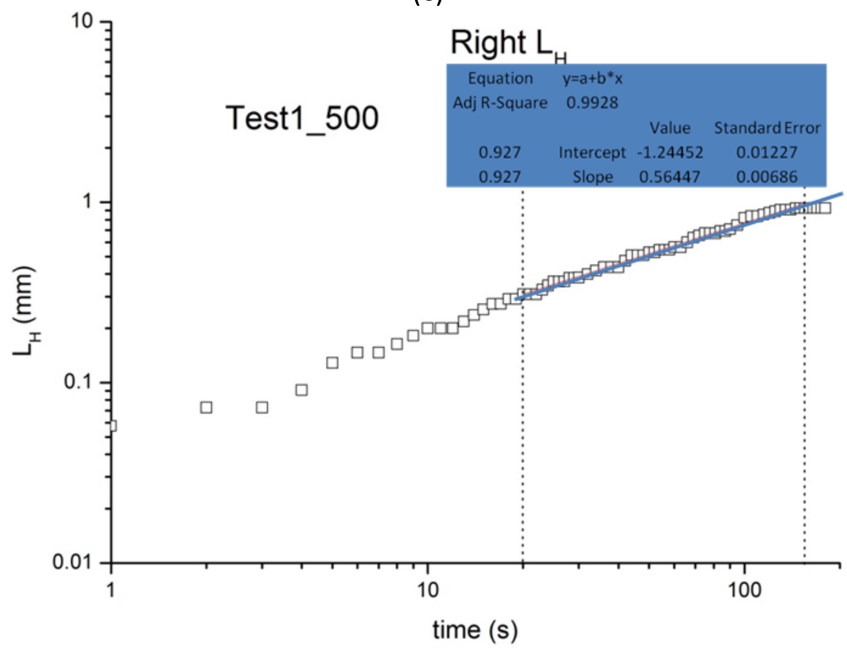

(d)

Figure 4. 27 Linear curve fit for Test2_500. (a) Left L_V (b) Right L_V (c) Left L_H (d) Right L_H

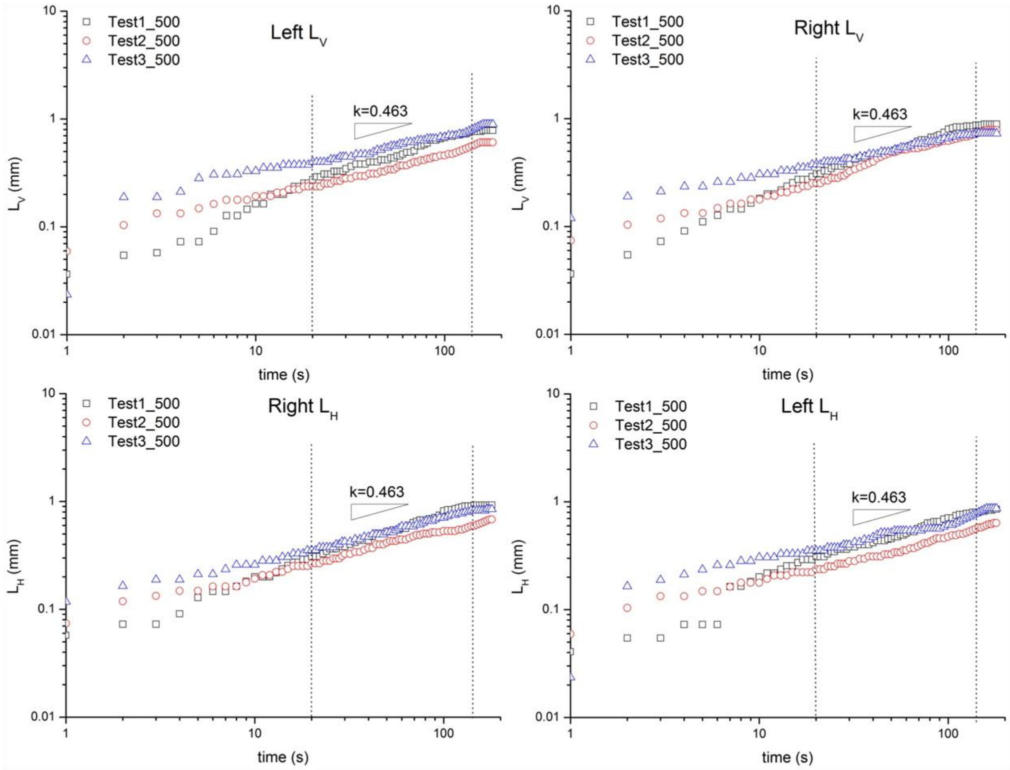

Figure 4. 28 Joint formation of Test1_500 to Test3_500 in logarithmic coordinates

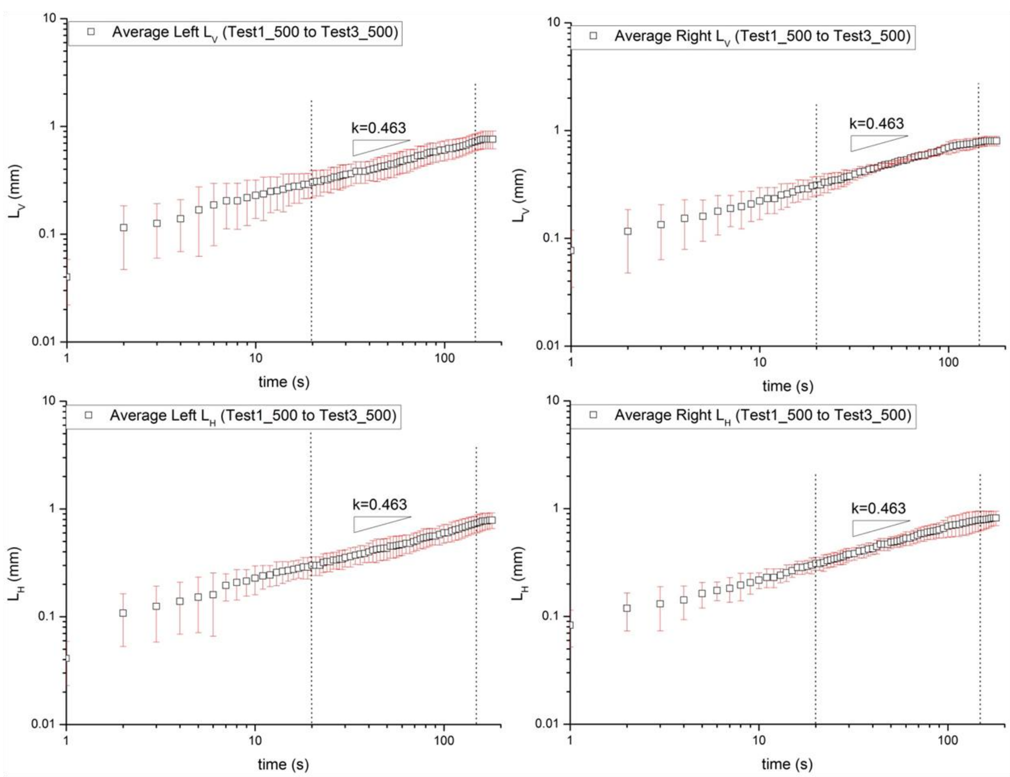

Figure 4. 29 Average Joint formation of Test1_500 to Test3_500 in logarithmic coordinates

From these figures, the development of the joint formation under 500 ppm (interpreted through the triple line movement) can still be divided into 3 stages:

(1) Initial Phase from 0 to 20s.

(2) 0.463 Power Law Phase from 20 to 160s.

The power law exponent value in this phase is smaller than that under 70 ppm and 200 ppm conditions indicating that a worse atmosphere condition results in slower formation growth rate. Hence, with the increase of oxygen level from 200 ppm to 500 ppm, it is hypothesized this leads to a change of the impact of the surface tension/capillary force and viscous force.

(3) Asymptotic Phase from 160 to 180s.

The curves become flat and no significant joint development is noticed beyond 160s indicating the full balance between capillary force, viscous force and possibly gravity.

Figure 4.30 shows normalized formations for all tests and Figure 4.31 shows average normalized length in logarithmic coordinates under 500 ppm condition.

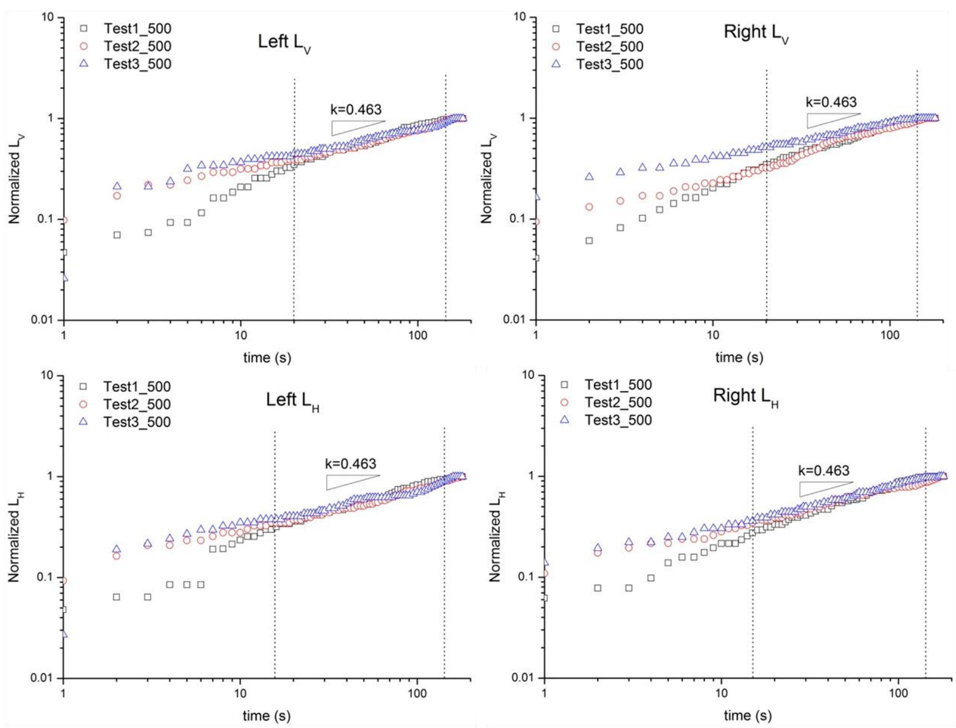

Figure 4. 30 Normalized joint formation of Test1_500 to Test3_500 in logarithmic coordinates

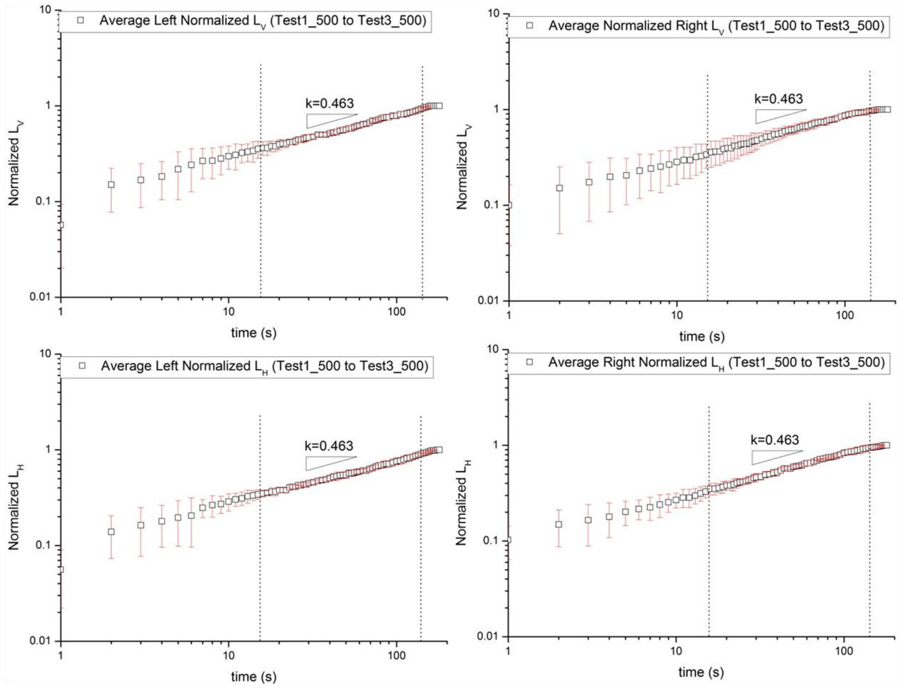

Figure 4. 31 Average normalized formation of Test1_500 to Test3_500 in logarithmic coordinates

Brazed sample of Test2_500 was randomly selected for further analysis as described for that under 70 ppm and 200 ppm conditions. Figure 4.32 shows the measurements of the distance between the interface and the lower surface of the brazing sheet.

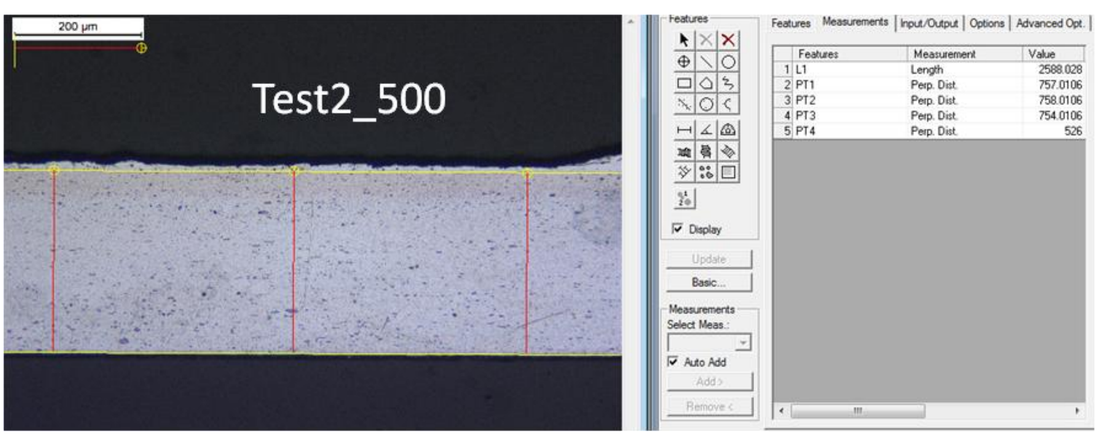

Figure 4. 32 Measurement of the distance between the brazing sheet lower surface and the clad/core interface of a brazed sample (Test2_500) near the joint area (to the right)

The brazed substrate thickness is examined in Figure 4.33. Table 4.8 shows the measurements results from each step similar as those in Table 4.2 and Table 4.5.

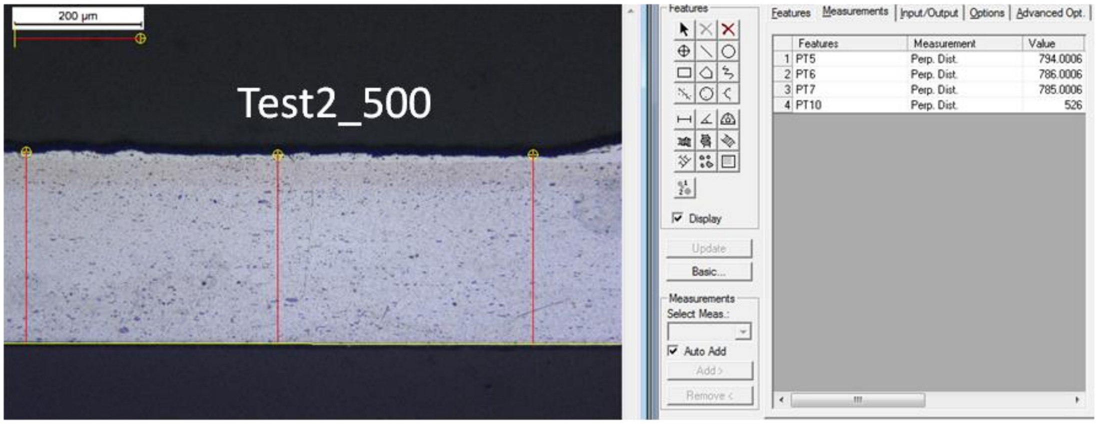

Figure 4. 33 Measurement of the brazed sample thickness (Test2_500)

Table 4.8 Summarized measurements for residue thickness study for Test2_500

500 ppm	Measurement (µm)	Comment	Note
step1	287 ± 1	Distance between the brazing sheet lower surface and the interface in the pre-brazed sample	Assumed to be the same for all tests
step2	288 ± 1	Distance between the brazing sheet lower surface and the interface in the brazed sample	
step3	1 ± 2	Absolute difference between measurements in step 1 and step 2	Interface assumed intact
step4	300 ± 2	The thickness of a brazed sample	
step5	12 ± 3	Clad residue thickness	
step6	13 ± 4	Clad thickness that is available to form the joint	

Figure 4.34 shows the core dissolution due to silicon diffusion in the joint formation in Test2_500.

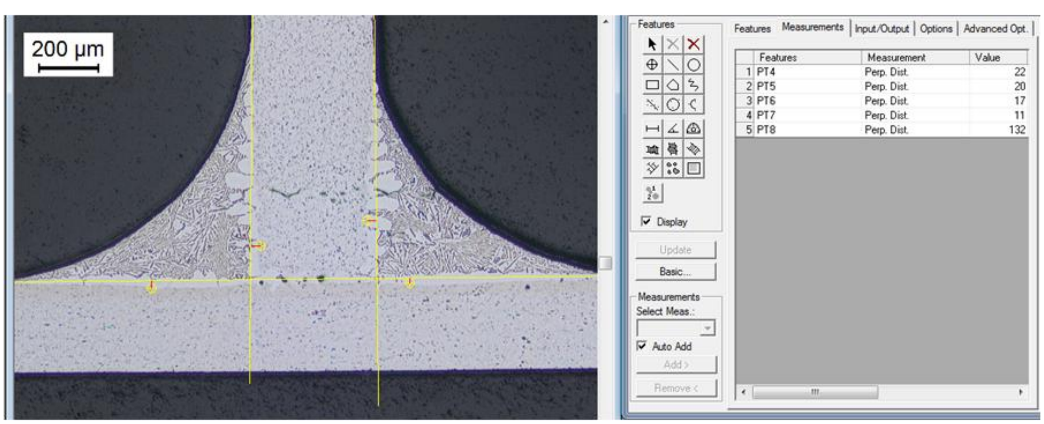

Figure 4. 34 Measurements of core dissolution (Test2_500)

The clearance between the horizontal substrate and vertical piece is completely filled with re-solidified clad. At the left and right sides, the maximum dissolution depths of the horizontal piece from the original surface are 26 ± 1 μm and 17 ± 1 μm, respectively. The maximum diffusion depths of the vertical piece are 33 ± 1 μm and 30 ± 1μm, respectively.

Figure 4.35 provides cross-section #1, cross-section #2 and cross-section #3 profiles at z=1.5 mm, z=7.5 mm and z=13.5 mm, respectively, along the z axis. The vertical and horizontal triple line locations measured at 3 cross-section profiles are summarized in Table 4.9.

It is clearly observed that along the depth direction L_V increases progressively and L_H reaches its maximum value at the center (7.5 mm). Based on the average value in Table 4.3 and Table 4.6, the standard deviations of all formations are much bigger (>0.08 mm) than those under 70 ppm and 200 ppm conditions. This implies that a 2-D configuration of joint formation can be questionable under 500 ppm condition. Clearly, the deterioration of the conditions causes non-uniform distribution of the clad flow. This phenomenon required further systematic study.

Table 4.9 Measured fillet formations of Test2_500 at 3 locations along the z axis (mm)

500ppm	1.5 mm	7.5 mm	13.5 mm	Average	Std
Left L_V	0.768	0.888	0.923	0.860	0.081
Left L_H	0.817	1.026	0.939	0.927	0.105
Right L_V	0.662	0.889	0.920	0.824	0.141
Right L_H	0.758	1.008	0.974	0.913	0.136

The equilibrium joint formations of Test2_500 measured using OCA units are:
Left L_V = 0.607 mm, Left L_H = 0.637 mm, Right L_V = 0.785 mm, Right L_H = 0.681 mm. (Appendix 8)

The relative deviations for L_V and L_H at both sides are:

Left: $$\%L_V = \left|\frac{0.607-0.768}{0.768}\right| = 21\%,\ \%L_H = \left|\frac{0.637-0.817}{0.817}\right| = 22\%$$

Right: $\%L_V = \left|\frac{0.785-0.662}{0.662}\right| = 19\%,\ \ \%L_H = \left|\frac{0.681-0.758}{0.758}\right| = 10\%$

The relative deviations are quite larger compared to those under the 70 ppm and 200 ppm conditions. This is because of both the combination of edge influence and non-uniformity joint formation along the z axis.

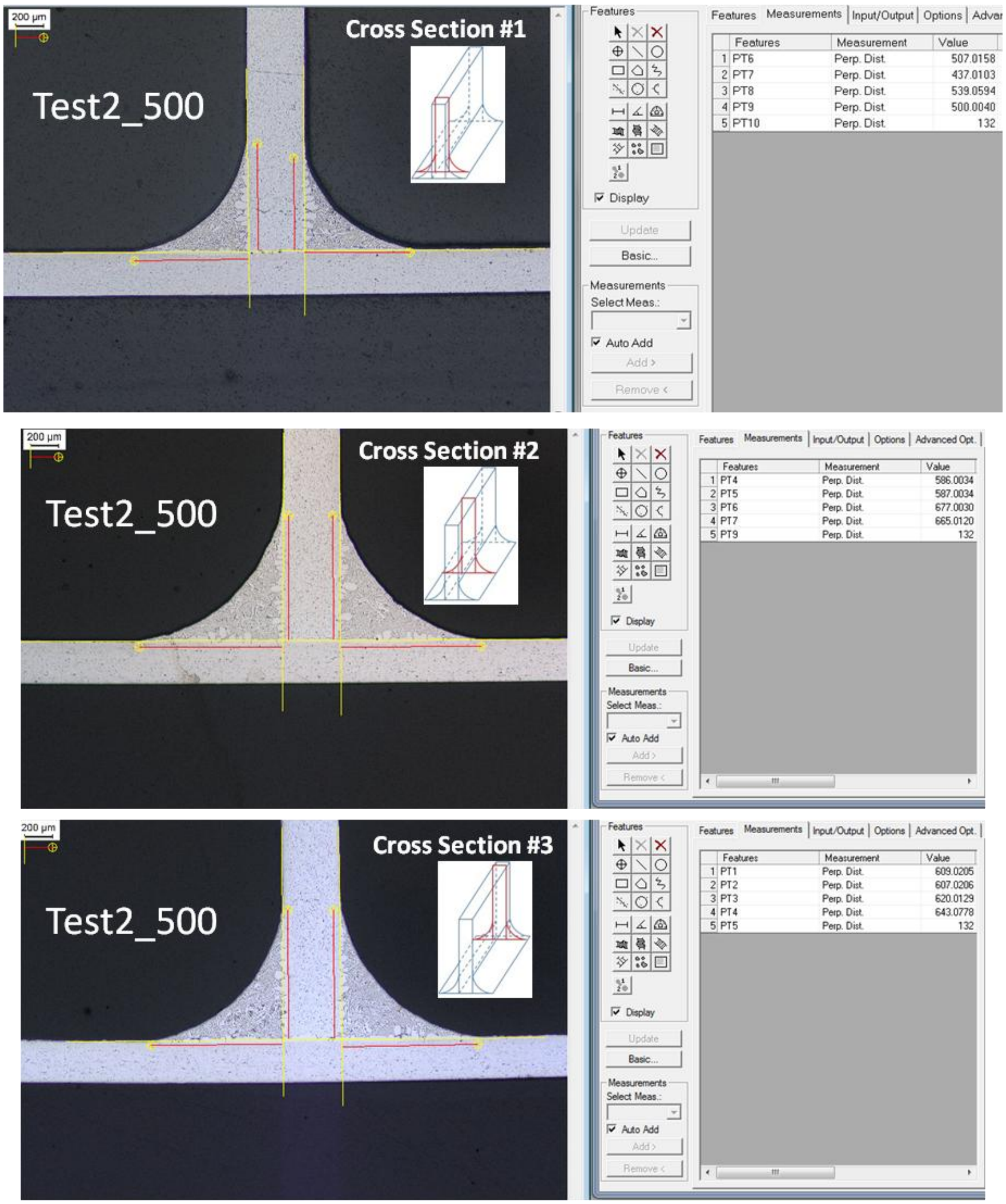

Figure 4. 35 Measurements of formation at 3 locations along the depth direction

4.4 2000 ppm Group Results

In order to explore a more severe deterioration of the background atmosphere, two additional series of tests had been executed. The first one involves a 400% increase in the oxygen concentration vs. the previous one, i.e., 2000 ppm vs. 500 ppm Oxygen. This series will be reviewed in this section. The final series refers to an air atmosphere conditions which has to illustrate an ultimate deterioration of up to 200000 ppm of Oxygen, and will be reniewed in the next section, 4.5.

11 tests were performed to investigate the kinetics of the triple line movement under the 2000 ppm Oxygen concentration condition. These tests can be divided into 4 groups, based on sample configurations and atmosphere condition.

4.4.1 The standard configuration & modified oxygen conditions:

7 tests were conducted with the same sample configuration used for tests under 70 ppm, 200 ppm and 500 ppm conditions.

Figure 4.36 shows the representative joint evolution (Test9_2000) for 3 minutes of recording time.

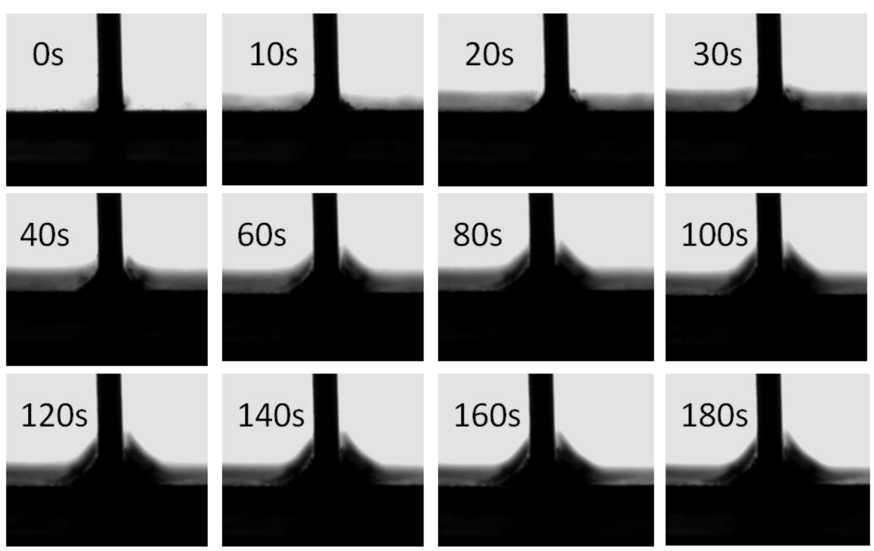

Figure 4. 36 Joint formation development of Test9_2000

It must be clear, after inspection of the sequence of images given in Figure 4.36 that the equilibrium envelopes of the growing fillet are becoming fuzzy and out of focus (what had not necessarily been a consequence of the out of focus imaging at the selected initial location). It can be clearly observed that after 30 seconds the area around vertical piece represented by shadow becomes darker and bigger and the cross-section profiles become blurry. This makes it impossible to reliably measure joint formations during the whole evolution time in the OCA. As mentioned earlier, the cross-section of T-joint seen in the OCA is the edge cross-section (at z=0 mm) along the joint fillet direction (Figure 4.8). In addition, the dimensions of L_V and L_H for that cross-section between 30s and 60s hardly change according to this observation (Figure 4.36). Therefore, this indicates that the formation development along the depth direction is not uniform. The change of shade level and dimension of shadows is due to the growth of formation at locations along the depth direction. The non-uniformity of joint development was confirmed at z=1.5 mm, 7.5 mm and 13.5 mm along the joint fillet direction through the *posteriori* evaluation of the re-solidified fillets formations (Figure 4.37).

The vertical and horizontal triple line locations measured at 3 locations are summarized in Table 4.10.

It is noted from Figure 4.37 that the joint formation is asymmetric under the condition of the oxygen level at 2000 ppm. Furthermore, from Table 4.10 one can notice that the joint formation (fillet) increases along the axial direction of the joint at an advanced "depth" location. Note that the standard deviations of the triple line locations are sizably larger when compared with those under 70 ppm, 200 ppm and 500 ppm conditions. Hence, it is relatively established that the non-uniformity of the joint formation becomes evident with an increase of oxygen level in the chamber due to the non-uniformity of molten clad flow into the joint (most likely due to an increased impact of oxidation during the joint formation at high Oxygen concentrations).

Table 4.10 Measured fillet formations at 3 locations along the depth direction (mm)

2000ppm	1.5 mm	7.5 mm	13.5 mm	Average	Std
Left Lv	0.256	0.809	0.917	0.661	0.355
Left LH	0.258	1.055	1.197	0.837	0.506
Right Lv	0.138	0.885	1.123	0.715	0.514
Right LH	0.218	0.967	1.306	0.830	0.557

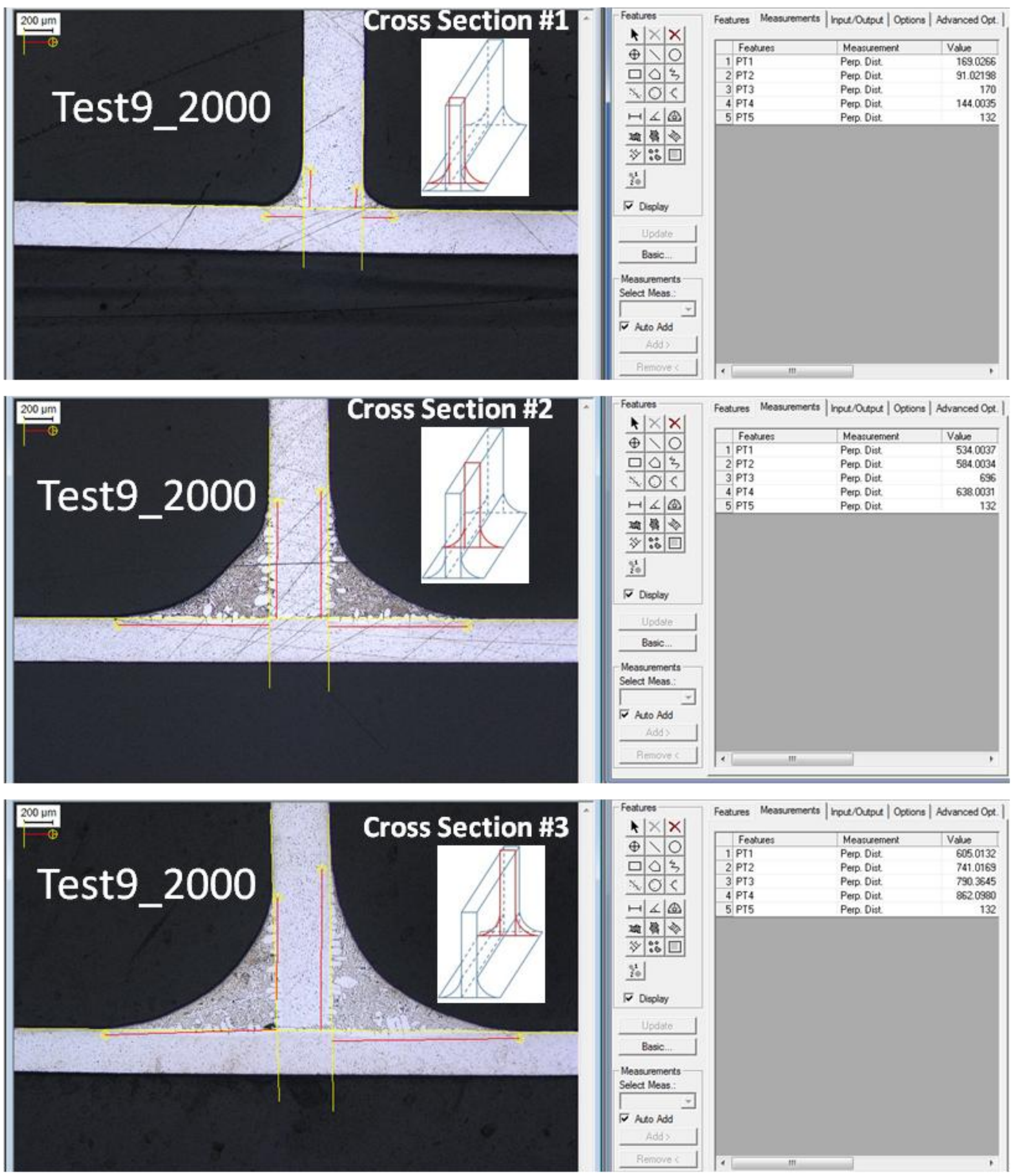

Figure 4. 37 Joint formation of Test9_2000 at 1.5 mm, 7.5 mm and 13.5 mm along the joint fillet direction

4.4.2 Prolonged purging duration

To explore whether the residue of the hot zone atmosphere prior to test execution may impact the experimental evaluations, one test was conducted with the same sample configuration as that in 4.4.1 but with an increased purging time, i.e., 4 hours and 15 minutes of purging of the 2000 ppm Nitrogen (Appendix 1).

Figure 4.38 shows the joint evolution of Test11_2000 for 3 minutes of recording time. The non-uniformity of the joint formation still exists; even though the purging duration was increased to more than 4 hours. Figure 4.39 shows the joint formations at 1.5 mm, 7.5 mm and 13.5 mm along the joint fillet direction.

The vertical and horizontal triple line locations measured at 3 locations are summarized in Table 4.11.

Table 4.11 Measured fillet formations from test with prolonged purging condition at 3 locations along the depth direction (mm), 2000 ppm

4.25 hr purging	1.5 mm	7.5 mm	13.5 mm	Average	Std
Left L_V	0.359	0.888	1.027	0.758	0.352
Left L_H	0.426	0.824	1.156	0.802	0.365
Right L_V	0.333	0.782	1.094	0.736	0.383
Right L_H	0.412	0.936	1.224	0.857	0.412

The non-uniformity and an asymmetry of the joint formation were still observed in this test under a prolonged purging Nitrogen condition. It can be concluded that the non-uniformity of the joint formation under 2000 ppm would not be impacted by the purging duration. Hence, a 2 hour purging of Nitrogen is considered as being sufficient to reach specified condition.

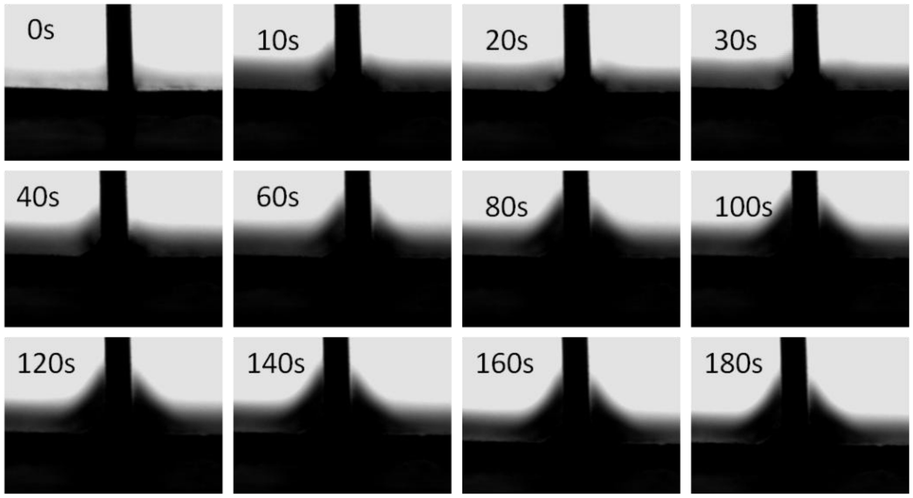

Figure 4. 38 Joint formation development of Test11_2000 under prolonged purging condition. The fuzziness of the fillet free surface is apparent.

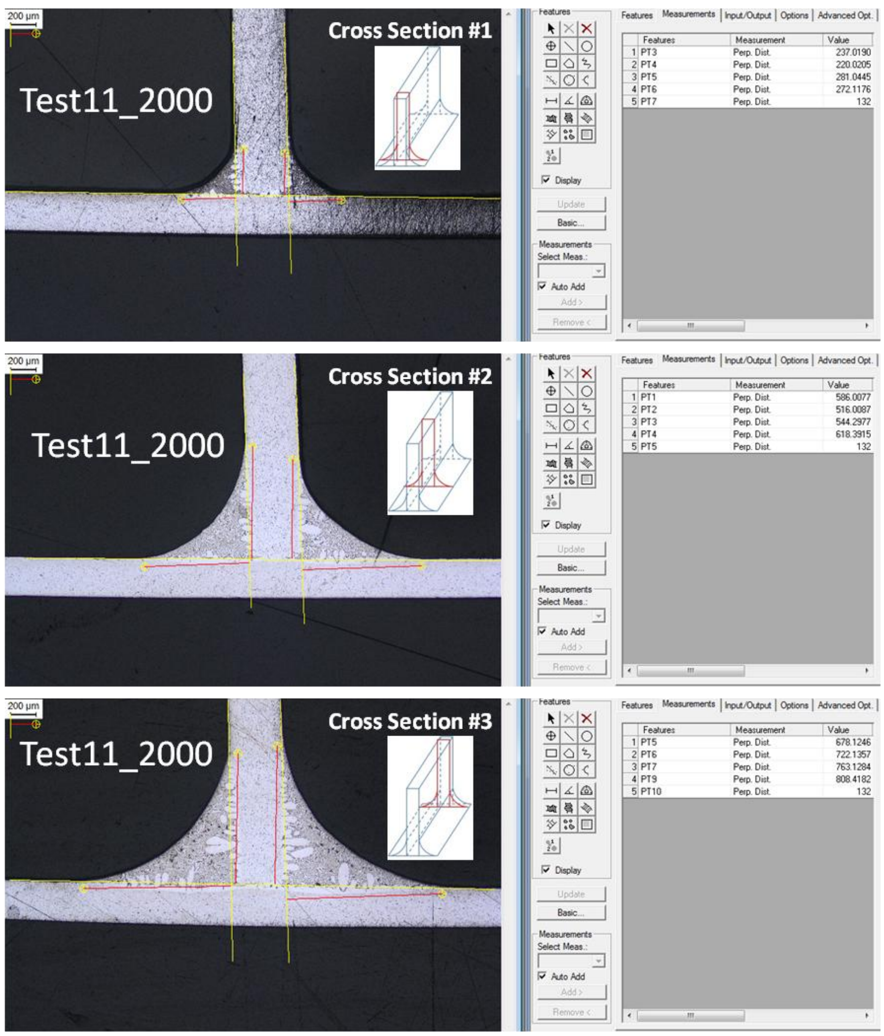

Figure 4. 39 Joint formation of Test11_2000 at 1.5 mm, 7.5 mm and 13.5 mm along the joint fillet direction

4.4.3 "Inverse" configuration

In order to explore whether the sample configuration/orientation within the hot zone has an impact, 2 tests were performed under an "inverse" sample configuration depicted in Fiugre 4.40.

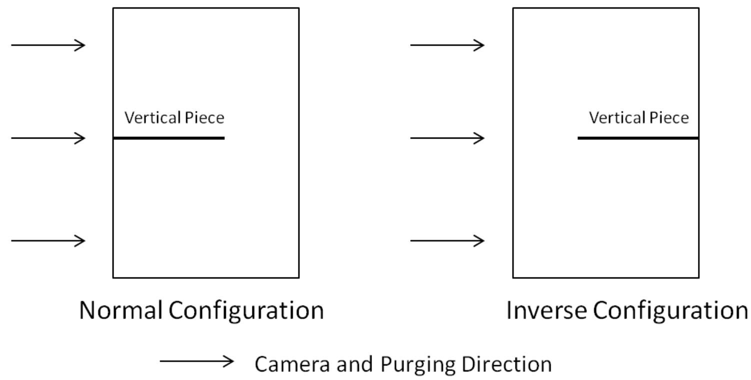

Figure 4. 40 Normal Configuration VS Inverse Configuration in top view

Figure 4.41 shows the joint evolution of Test4_2000 for 3 minutes of recording time with the "inverse" configuration. Figure 4.42 shows the joint formations at 1.5 mm, 7.5 mm and 13.5 mm along the joint fillet direction.

The vertical and horizontal lengths measured at 3 locations are summarized in Table 4.12.

Table 4.12 Measured fillet formations from test with an inverse configuration at 3 locations along the joint fillet direction (mm), 2000 ppm

Inverse Configuration	1.5 mm	7.5 mm	13.5 mm	Average	Std
Left L_V	0.633	0.915	0.868	0.805	0.151
Left L_H	0.691	0.930	0.995	0.872	0.160
Right L_V	0.747	0.921	0.852	0.840	0.088
Right L_H	0.712	0.882	0.826	0.807	0.087

It can be seen that under "inverse" configuration the asymmetry and non-uniformity still exist but are better mitigated compared with the previous configuration. Further investigation needs to be conducted.

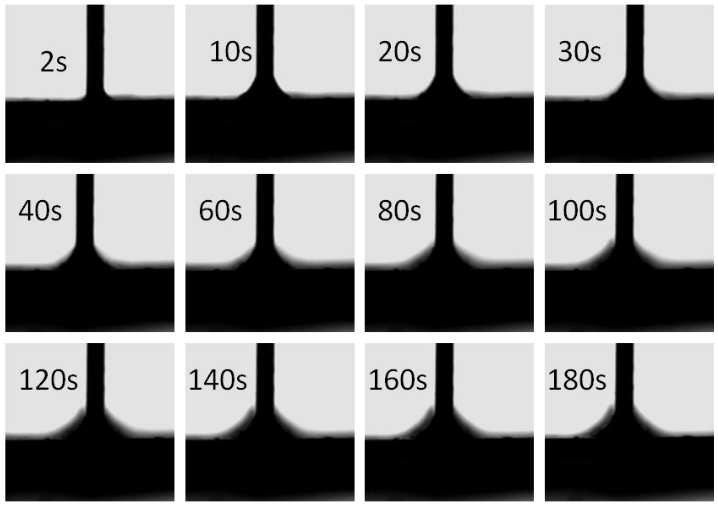

Figure 4. 41 Joint formation development of Test4_2000 under inverse configuration

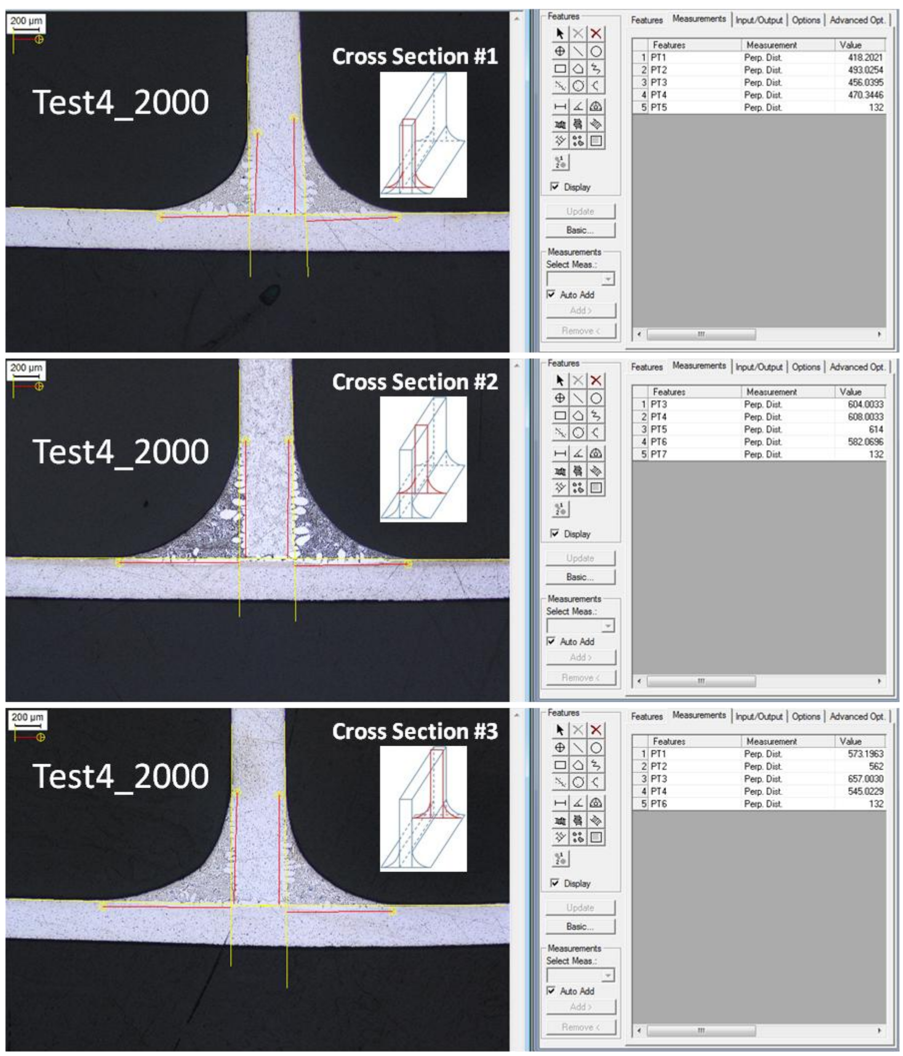

Figure 4. 42 Joint formation of Test4_2000 at 1.5 mm, 7.5 mm and 13.5 mm along the joint fillet direction

4.4.4 "Narrow" configuration

Further sample configuration has been considered. Namely, 2 tests were performed on samples with a so called "narrow" sample configuration. The narrow sample configuration is presented in Fiugre 4.43.

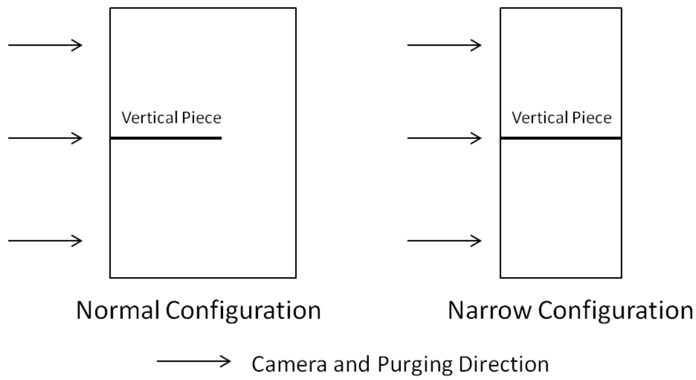

Figure 4. 43 Normal Configuration VS Narrow Configuration in top view

Figure 4.44 shows the joint evolution of Test8_2000 for 3 minutes of recording time. Figure 4.45 shows the joint formations at 1.5 mm, 7.5 mm and 13.5 mm along the joint fillet direction for that test.

The vertical and horizontal lengths measured at 3 locations are summarized in Table 4.13.

Table 4.13 Measured fillet formations from test with narrow configuration at 3 locations along the joint fillet direction (mm), 2000 ppm

Narrow Configuration	1.5 mm	7.5 mm	13.5 mm	Average	Std
Left L_V	0.523	0.858	0.853	0.745	0.192
Left L_H	0.598	0.838	0.894	0.777	0.157
Right L_V	0.370	0.845	0.852	0.689	0.276
Right L_H	0.573	0.873	0.891	0.779	0.179

As it can be seen (Figure 4.43 and Figure 4.44 and Table 4.13), under the narrow configuration the asymmetry and non-uniformity still exist but are a bit better mitigated when compared with the original configuration. It may be hypothesized that this is due to the geometric symmetry of the sample configuration. The center line of the substrate is coincident with the center line of the vertical piece hence resulting in more or less uniform formation along the depth direction. Further investigation needs to be designed to verify this.

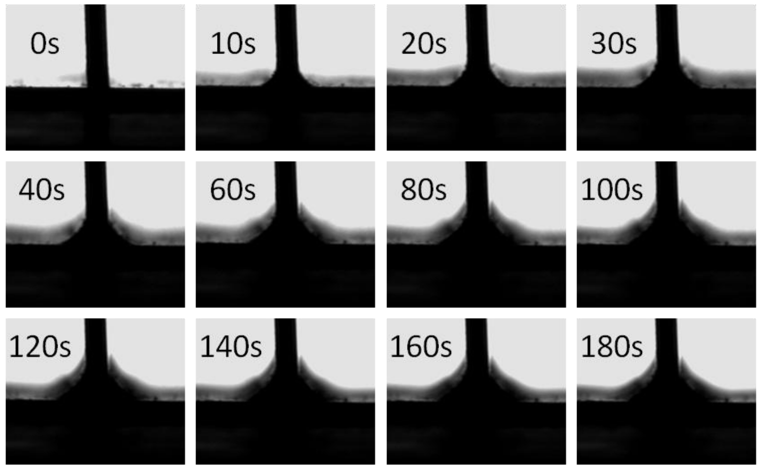

Figure 4. 44 Joint formation development of Test8_2000 under narrow configuration

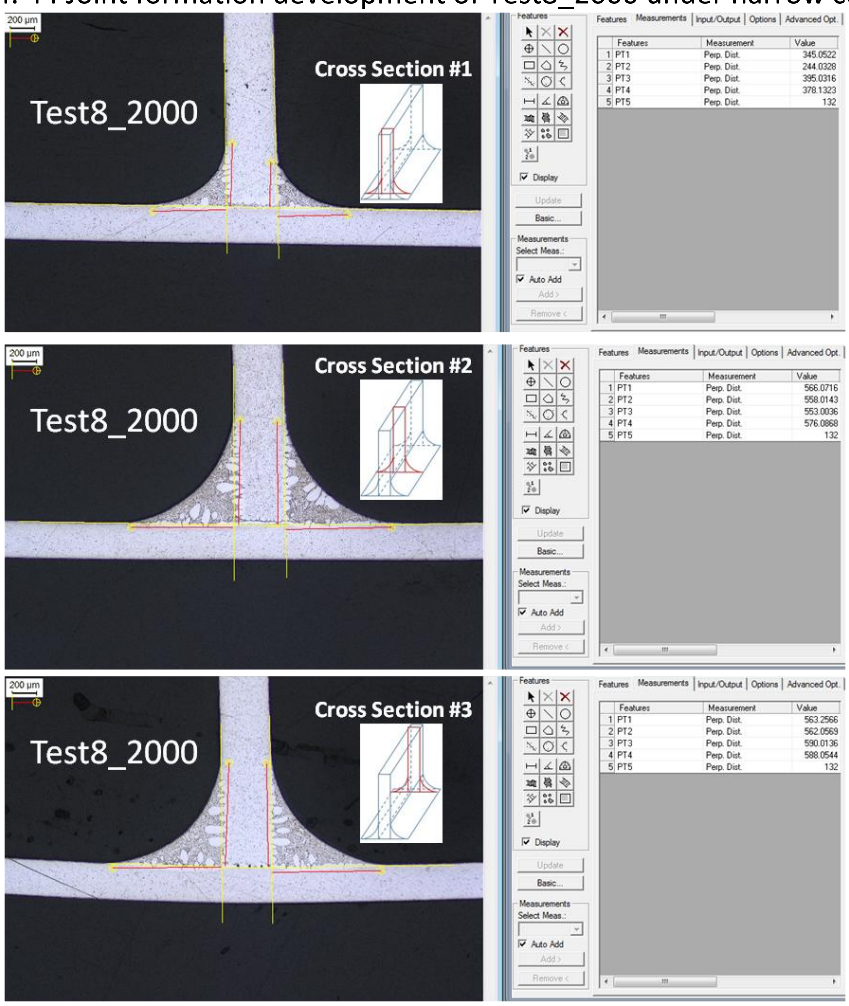

Figure 4. 45 Joint formation of Test8_2000 at 1.5 mm, 7.5 mm and 13.5 mm along the joint fillet direction

4.5 200000 ppm (Compressed Air) Group Results

Finally, to consider a case of an ultimately poor background atmosphere conditions, three tests were performed under the 200000 ppm (compressed air) condition, with all the other conditions unchanged. The video recording time was increased to 7 minutes corresponding to thermocouple temperature change in the range of 569 °C ~ 605 °C, in order to examine whether a joint formation takes place at all. Joint formations were not observed in all three tests.

Figure 4.46 shows the three cross-sections of samples' mating surfaces at 1.5 mm, 7.5 mm and 13.5 mm along the joint fillet direction.

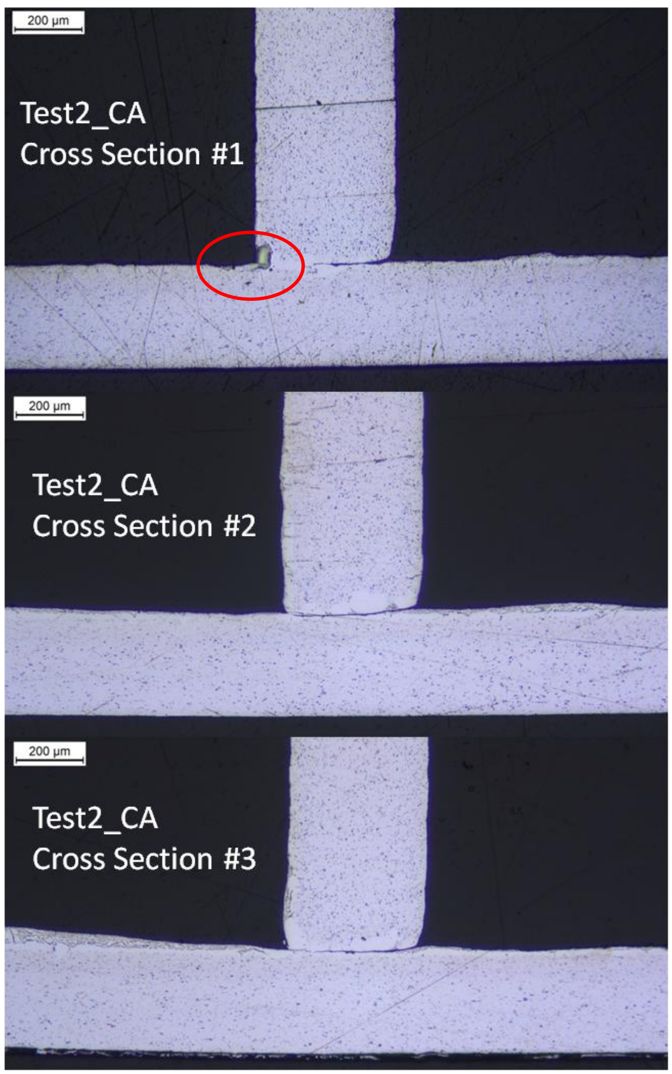

Figure 4. 46 Three cross-section profiles along the joint fillet direction of Test2_CA

It is clearly seen that the joint zone is not formed and that the clearance between vertical piece and substrate at 7.5 mm and 13.5 mm is not filled with the re-solidified clad. At 1.5 mm location, a small portion of the gap is filled. Note that some melting of the clad and its re-solidification in form of the primarily alpha phase in the joint zone are apparent. Some re-solidified eutectic phase is accumulated away from the vertical mating surface (see in particular the 13.5 mm cross-section), but this liquid was not able to flow into the joint. Therefore, it is concluded that brazing cannot join AA3003 vertical piece to the horizontal substrate with this clad material under air/atmosphere conditions. Since joint formation was observed under 2000 ppm condition, there must be a threshold between 2000 ppm and 200000 ppm under which joint formation fails to occur while keeping other conditions unchanged. This threshold has been under consideration by another project currently under way in the UK brazing laboratory[65].

4.6 Summary Comparisons of the Kinetics Results for Different Background Atmosphere Conditions

The joint formation non-uniformity was not negligible under 2000 ppm condition, and no joint formation was observed under the atmosphere of 200000 ppm Oxygen content (Air). So, the kinetics of the triple line movement comparisons was made for 70 ppm, 200 ppm and 500 ppm tests only.

Figure 4.47 and Figure 4.48 show the average dimensional and normalized joint formations for 70 ppm, 200 ppm and 500 ppm in linear Cartesian coordinates, with a time interval of 1 second and 10 seconds (for the sake of clarity) at left and right, respectively.

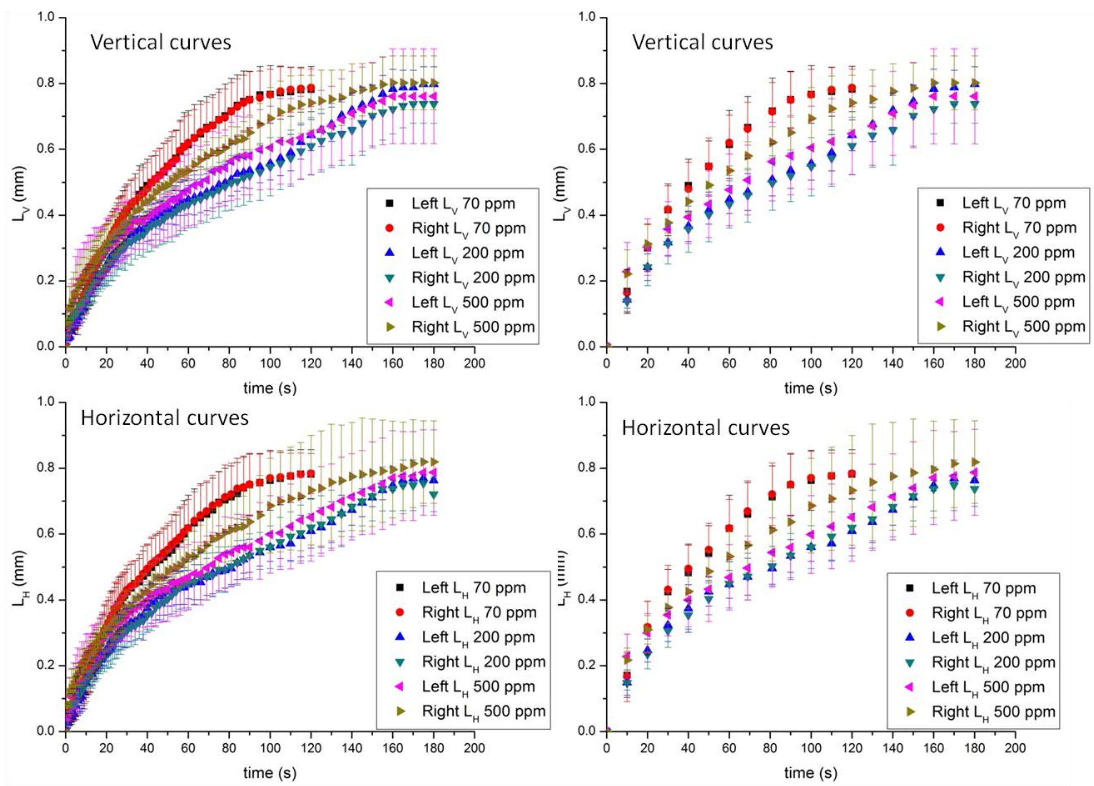

Figure 4. 47 Triple line kinetics under 70 ppm, 200 ppm and 500 ppm conditions

As mentioned in previous sections, the duration of evolution of the joint formation is around 100 seconds and 160 seconds for 70 ppm/200 ppm groups, and 500 ppm group, respectively. In addition, the joint fillet formation is highly symmetric under 70 ppm condition. With an increase in oxygen level in the chamber, the asymmetry of the kinetics/joint topography increases. Under the 200 ppm condition, asymmetry is only noted in vertical dimension for a smaller evolution time duration (120 s ~ 160 s). Under the 500 ppm condition asymmetry is observed in both vertical and horizontal directions for a larger-time duration (between 40 s ~ 160 s).

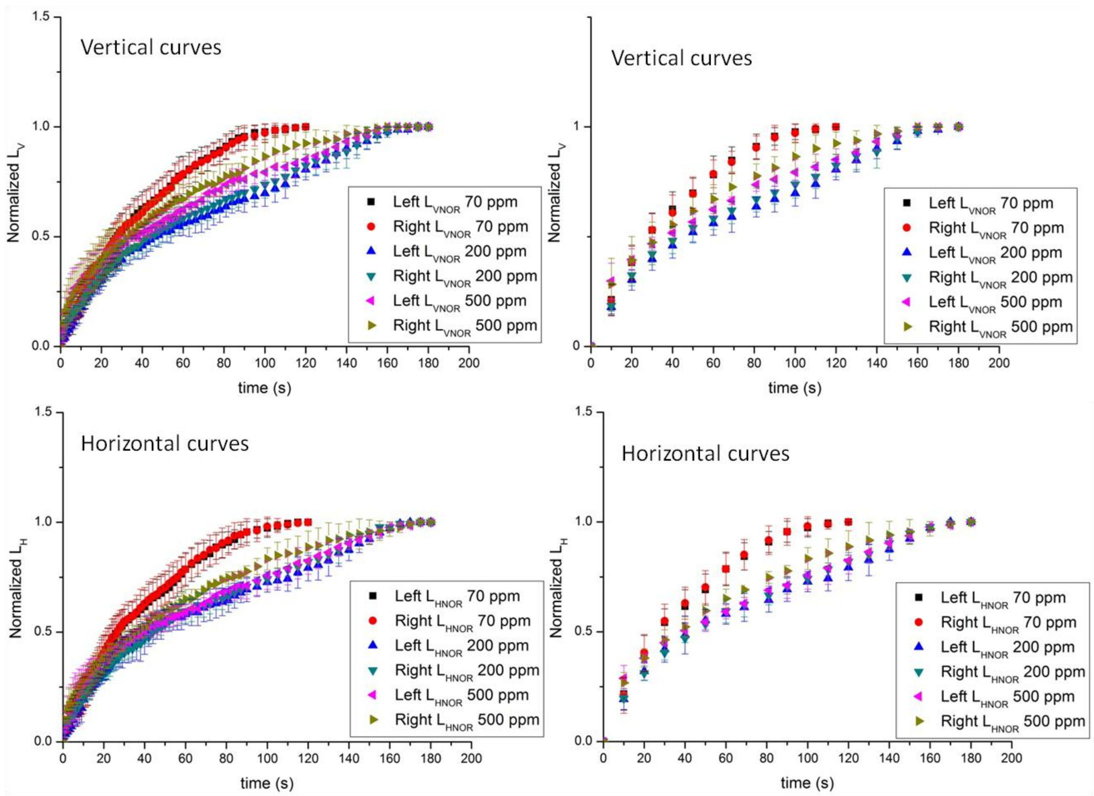

Figure 4. 48 Normalized triple line kinetics under 70 ppm, 200 ppm and 500 ppm conditions

It is found that the joint formation is completed in a shorter time (that is, the triple line movement is faster) under 70 ppm condition than under 200 ppm and 500 ppm condition. Note that, the formation curves under 500 ppm condition are slightly above those under 200 ppm condition. That is, the rate of growth appears to be larger for 500 ppm but both are rather slow when compared with the more ideal conditions. This may be an artifact of experimentation because the data are primarily associated with the cross-section at the location of z=0 mm along the joint fillet direction (where the focus is) and the geometric configuration at the edge has notable influence on joint formations under both 200 ppm and 500 ppm conditions (See relative deviations for each group, Table 4.3, 4.6 and 4.9). But at different locations along the depth direction, the formation between 200 ppm and 500 ppm conditions are not the same as for the joint formation at 0 mm. Comparing the data in Table 4.6 with those in Table 4.9, it is discovered that data associated in Table 4.6 is larger than those in Table 4.9. Thus, overall, it is reasonable to speculate that actual kinetic curves of 200 ppm should be above those of 500 ppm at correspondent location along the depth direction. However, most likely, both 200 and 500 ppm cases belong to the same level of impact of the atmosphere on the kinetics (the impact most likely has to be measured on a logarithmic scale so that 500 and 200 ppm's are close to each other).

CHAPTER 5: CONCLUSIONS AND FUTURE STUDY

The kinetics of wedge-Tee joint formation of aluminum brazing on a reactive substrate in a Controlled Atmosphere Brazing furnace under 5 different oxygen level conditions has been researched. Joint formation evolutions more or less conform to a theoretical Washburn type model for oxygen concentrations equal or smaller than 200 ppm. The non-uniformity of the joint formation under these conditions is negligible. Non-uniformity and asymmetry of the joint formation was well documented for larger oxygen concentration (500 ppm and 2000 ppm conditions). It is demonstrated that under dry air condition, the joining formation is unable to occur. It was realized that the oxidation of the clad has significant impact on the uniformity of joint formation. The joint formation micrographs were investigated, focusing on core erosion in the vertical piece and horizontal substrate.

5.1 Summaries and Conclusions

The following conclusions can be made from this thesis work:

(1) Joining process can be divided, in general, into 3 phases:

a) Initial Phase: Lasts for about 20 s (70 ppm), 15 s (200 ppm) and 20 s (500 ppm);

b) Power Law Phase: n=0.525 lasts for about 80 s under 70 ppm condition , n= 0.525 lasts for about 145 s under 200 ppm condition and n=0.463 lasts for about 120 s under 500 ppm condition;

c) Equilibrium Phase: Beyond 100 s (70 ppm) and beyond 160 s (200 ppm and 500 ppm).

(2) With an increase of the oxygen level, the fillet formation of joints deteriorates: a) The rate of joint formation evolution decreases; b) Non-uniform spreading appears with an increase in oxygen level concentration above 200 ppm; c) Non-

uniform joint formation fillet cross-section in axial direction of the joint formation is sizable if oxygen level concentration is larger than 500 ppm.

(3) 2-D Configuration (uniform fillet) of joint formation can be secured under 70 ppm and 200 ppm conditions; not valid at the 500 ppm and 2000 ppm levels.

(4) Joining cannot occur (no surface tension flow) under 200000 ppm (air) condition. Any produced liquid metal re-solidifies *in situ*.

(5) Local horizontal direction core dissolutions (on a vertical member of the wedge-tee joint) are more significant than vertical direction substrate dissolutions (on a horizontal member – brazing sheet).

(6) Geometric configuration of a sample may influence joint formation under a high oxygen level (200 ppm, 500 ppm and 2000 ppm) since the molten metal flow kinetics at the sample edge and along the depth direction differs.

(7) 2 hour of purging of specified composition of the Nitrogen background atmosphere is sufficient for the controlled atmosphere brazing in this study.

5.2 Future Study

The following topics should be investigated in order to understand the mechanism of an aluminum alloy brazing on a substrate in a T-joint configuration.

(1) Increase the statistical confidence of the joint topology data set. A large number of tests have been executed but a limited number of joint cross sections after brazing have been analyzed. More samples from each group need to be processed to investigate the development of clad-core interface with the help of SEM and extend this impact to understand the consequences related to kinetics (i.e., how the interface reaction impacts the kinetics).

(2) A theoretical modeling of the triple line kinetics under 70 ppm of Oxygen condition can be performed based on the collected data (an acceptable reproducibility since the relative errors between measurements from OCA and those from polished samples are small and kinetics curves collapse to the same domain in multiple tests). The modeling has to identify the multi-phase character of the kinetics curves and follow the impact of inertial, surface tension and viscosity forces. The asymptotic termination of the joint formation vs. the removal of the available liquid phase has to be considered through the conservation of mass.

(3) Investigate the exact position of the threshold of oxygen level impact between 2000 ppm and 200000 ppm beyond which the joint formation will not occur.

Appendix 1: Gas Sources specification data from the supplier

Gas type*	O_2 level in thesis (ppm)	Certified O_2 concentration (ppm)	Certified Moisture (ppm)	Notes
Nitrogen	70	<2	<3	99.999% purity
Nitrogen	200	210±4	N/A	
Nitrogen	500	501±10	N/A	
Nitrogen	2000	2003±40	N/A	
Compressed air	200000	195000 - 235000	<8	

* Source: Scott-Gross Certifications

Appendix 2: Test designations and conditions

NOR = Normal Configuration   INV = Inverse Configuration

NAR = Narrow Configuration T_{FS} = Joint Formation Start Temperature

Designation	Configuration	Date	Purging source	Purging duration (h)	Oxygen level (ppm)	T_{FS} (°C)
Test1_70	NOR	100912	2 ppm N_2	2	73	575
Test2_70	NOR	102112	2 ppm N_2	2	72	575
Test3_70	NOR	102612	2 ppm N_2	2	69	574
Test4_70	NOR	110112	2 ppm N_2	2	73	575
Test5_70	NOR	110412	2 ppm N_2	2	67	579
Test6_70	NOR	110912	2 ppm N_2	2	63	576
Test7_70	NOR	112712	2 ppm N_2	2	72	572
Test1_200	NOR	113012	210 ppm N_2	2	240	572
Test2_200	NOR	120112	210 ppm N_2	2	240	574
Test3_200	NOR	120312	210 ppm N_2	2	240	572
Test1_500	NOR	120412	501 ppm N_2	2	520	576
Test2_500	NOR	120512	501 ppm N_2	2	520	573
Test3_500	NOR	120812	501 ppm N_2	2	510	575
Test1_2000	NOR	112812	2003 ppm N_2	2	2000	572
Test2_2000	NOR	121012	2003 ppm N_2	2	1900	571
Test3_2000	NOR	010713	2003 ppm N_2	2	2000	573
Test4_2000	INV	010613	2003 ppm N_2	2	2000	570
Test5_2000	INV	011213	2003 ppm N_2	2	2000	575
Test6_2000	NOR	011313	2003 ppm N_2	2	2000	573
Test7_2000	NOR	012813	2003 ppm N_2	2	2000	573
Test8_2000	NAR	012913	2003 ppm N_2	2	2000	580
Test9_2000	NOR	013013	2003 ppm N_2	2	2000	578
Test10_2000	NAR	020113	2003 ppm N_2	2	2000	580
Test11_2000	NOR	021013	2003 ppm N_2	4.25	2000	579
Test1_CA	NOR	011713	Compressed air	2	N/A*	N/A
Test2_CA	NOR	011813	Compressed air	2	N/A	N/A
Test3_CA	NOR	011913	Compressed air	2	N/A	N/A

* See Appendix 1, compressed air specification

Appendix 3: Oxygen level data for all tests

	Test1_70	Test2_70	Test3_70	Test4_70	Test5_70	Test6_70	Test7_70	Test1_200	Test2_200	Test3_200
time (s)	O2 (ppm)	O2 (ppm)	O2 (ppm)	O2 (ppm)	O2 (ppm)	O2 (ppm)	O2 (ppm)	O2 (ppm)	O2 (ppm)	O2 (ppm)
0	73	72	69	74	66	63	72	240	240	230
30	73	72	69	74	67	63	72	240	240	230
60	73	72	69	73	67	63	71	240	240	230
91	73	72	68	73	66	62	71	240	240	230
121	73	72	68	73	66	62	70	230	240	230
151	72	71	68	73	65	62	70	230	230	230
181	72	68	68	72	63	62	70	230	240	230
211	71	63	68	72	57	61	68	230	240	230
242	67	60	66	70	54	61	67	230	240	230
272	64	60	64	68	53	60	64	230	230	230
302	60	60	59	64	53	57	59	220	220	220
332	56	60	57	59	53	52	56	190	180	180
362	54	59	56	57	53	49	55	180	150	140
393	55	60	56	57	53	49	54	190	150	140
423	59	59	56	57	53	49	54	200	180	160
453	60	59	57	57	53	49	54	210	190	180
483	60	59	57	58	53	49	54	220	200	190
514	61	59	57	58	53	49	54	220	210	190
544	61	59	57	58	53	49	55	220	210	200
574	62	59	57	58	53	49	55	220	210	200
604	62	59	57	58	54	49	55	220	210	200
634	63	59	57	58	54	49	55	220	210	200
665	63	59	57	58	54	49	55	220	210	200
695	64	59	57	58	54	49	55	220	210	200
725	64	59	57	58	54	49	59	220	210	200
755	65	59	57	58	54	49	58	210	200	200
785	65	58	57	58	54	49	58	210	200	200
816	66	57	57	58	54	49	58	210	200	190
846	66	57	57	58	54	49	58	210	200	190
876	66	57	57	58	54	49	58	210	200	190
906	67	57	56	58	54	49	58	200	190	190
936	67	57	56	57	55	48	58	200	190	190
967	68	57	56	57	55	48	58	200	180	190
997	68	58	56	57	55	48	58	190	180	180
1027	69	58	56	57		47	57	190	170	170

1057	69		55	57		47	57	190	170	170
1087	69		55	57		47	56	180	170	170
1118	70		55	57		47	56	180	170	170
1148	71		55	58		46	55	180	170	170
1178	71		55	58		47	55	180	180	170
1208	71		55	58		47	55	180	180	170
1239	72		56			47	55	180	190	170
1269	72		56			47	55	180	190	180
1299	73					47	55	180	190	180
1329						48	56	190	190	180
1359								190		190
1390								190		190
1420								190		190
1450										200
1480										200
1510										200
1541										190
1571										190

	Test1_ 500	Test2_ 500	Test3_ 500	Test1_ 2000	Test2_ 2000	Test3_ 2000	Test4_ 2000	Test5_ 2000	Test6_ 2000	Test7_ 2000
time (s)	O2 (ppm)	O2 (ppm)	O2 (ppm)	O2 (ppm)	O2 (ppm)	O2 (ppm)	O2 (ppm)	O2 (ppm)	O2 (ppm)	O2 (ppm)
0	520	520	510	1900	1900	1900	1900	1900	2000	2000
30	520	520	510	2000	1900	2000	1900	1900	2000	2000
60	520	520	510	2000	1900	2000	1900	1900	2000	2000
91	520	520	510	2000	1900	1900	1900	1900	2000	2000
121	520	520	510	2000	1900	2000	1900	1900	2000	2000
151	520	520	510	2000	1900	1900	1900	1900	2000	2000
181	520	520	510	2000	1900	1900	1900	1900	2000	2000
211	520	510	510	1900	1900	1900	1900	1900	2000	2000
242	510	500	510	1900	1900	1900	1900	1900	2000	2000
272	510	500	500	1800	1900	1900	1900	1900	2000	2000
302	490	500	490	1800	1800	1900	1900	1900	1900	2000
332	460	500	460	1800	1800	1900	1800	1800	1900	1900
362	450	490	430	1900	1800	1900	1700	1700	1900	1900
393	460	490	430	1900	1800	1900	1800	1700	1800	1900
423	470	490	440	1900	1800	1900	1800	1800	1800	1900
453	480	480	450	1900	1800	1900	1800	1800	1800	2000
483	490	480	450	1900	1800	1900	1800	1900	1800	2000
514	490	480	450	1900	1900	1900	1900	1900	1900	2000
544	490	480	460	1900	1900	1900	1900	1900	1900	2000

574	490	470	460	1900	1900	1900	1900	1900	1900	2000
604	490	460	460	1900	1900	1900	1900	1900	1900	2000
634	480	450	460	1900	1800	1900	1900	1900	1900	2000
665	480	450	460	1900	1800	1900	1900	1900	1900	2000
695	480	440	460	1900	1800	1900	1900	1900	1900	2000
725	480	440	460	1900	1800	1900	1900	1900	1900	2000
755	470	440	460	1800	1800	1900	1900	1900	1900	2000
785	470	440	460	1800	1800	1900	1900	1800	1900	2000
816	470	440	460	1800	1800	1900	1900	1900	1900	2000
846	460	440	450	1800	1800	1900	1900	1900	1900	2000
876	440	450	450	1800	1800	1900	1900	1900	1900	2000
906	440	450	440	1800	1800	1900	1800	1900	1900	2000
936	440	460	430	1700	1800	1900	1900	1800	1900	2000
967	430	460	430	1700	1800	1900	1800	1800	1900	1900
997	430	470	420	1700	1800	1900	1800	1800	1900	1900
1027	440	470	420	1700	1700	1900	1800	1800	1900	1900
1057	440	470	420	1800	1700	1900	1800	1800	1900	1900
1087	450	460	430	1800	1800	1900	1700	1800	1900	1900
1118	450	440	430	1800	1800	1900	1700	1800	1900	1900
1148	460	440	440	1800	1800	1900	1800	1700	1900	1900
1178	460	440	440	1800	1800	1900	1800	1800	1900	1900
1208			450	1900	1800	1900	1800	1800	1900	1900
1239			450	1900	1800	1800	1800	1800	1900	2000
1269			460	1900	1800	1800	1800	1800	1900	2000
1299			460	1900	1800	1800	1800	1800	1900	2000
1329			460	1900	1800	1800	1800	1800	1900	2000
1359			460	1900	1900	1800	1800	1900	1900	
1390				1900	1900	1900	1900	1900	1800	
1420				1900		1900	1900	1900	1800	
1450				1900		1900	1900	1900	1800	
1480				1900		1900	1900	1900	1800	
1510				1900		1900			1800	
1541				1900		1900			1800	
1571				1900		1900			1800	

	Test8 _2000	Test9 _2000	Test10 _2000	Test11 _2000	Test1 _CA	Test2 _CA	Test3 _CA
time (s)	O_2 (ppm)	O_2 (ppm)	O_2 (ppm)	O_2 (ppm)	O_2 (ppm)	O_2 (ppm)	O_2 (ppm)
0	2000	2000	2000	2000	N/A	N/A	N/A
30	2000	2000	2000	2000	N/A	N/A	N/A

60	2000	2000	2000	2000	N/A	N/A	N/A
91	2000	2000	2000	2000	N/A	N/A	N/A
121	2000	2000	2000	2000	N/A	N/A	N/A
151	2000	2000	2000	2000	N/A	N/A	N/A
181	2000	2000	2000	2000	N/A	N/A	N/A
211	2000	2000	2000	2000	N/A	N/A	N/A
242	2000	2000	2000	2000	N/A	N/A	N/A
272	2000	2000	2000	2000	N/A	N/A	N/A
302	2000	1900	2000	2000	N/A	N/A	N/A
332	1900	1900	1900	1900	N/A	N/A	N/A
362	1800	1900	1900	1900	N/A	N/A	N/A
393	1800	1900	1900	1900	N/A	N/A	N/A
423	1900	1900	1900	1900	N/A	N/A	N/A
453	1900	1900	2000	2000	N/A	N/A	N/A
483	1900	1900	2000	2000	N/A	N/A	N/A
514	2000	1900	2000	2000	N/A	N/A	N/A
544	2000	1900	2000	2000	N/A	N/A	N/A
574	2000	1900	2000	2000	N/A	N/A	N/A
604	2000	1900	2000	2000	N/A	N/A	N/A
634	2000	1900	2000	2000	N/A	N/A	N/A
665	2000	1900	2000	2000	N/A	N/A	N/A
695	2000	1900	2000	2000	N/A	N/A	N/A
725	2000	1900	2000	2000	N/A	N/A	N/A
755	2000	1900	2000	2000	N/A	N/A	N/A
785	2000	1900	2000	2000	N/A	N/A	N/A
816	1900	1900	2000	2000	N/A	N/A	N/A
846	1900	1900	2000	2000	N/A	N/A	N/A
876	1900	1900	2000	2000	N/A	N/A	N/A
906	1900	1900	1900	1900	N/A	N/A	N/A
936	1900	1900	1900	1900	N/A	N/A	N/A
967	1900	1900	1900	1900	N/A	N/A	N/A
997	1900	1900	1900	1900	N/A	N/A	N/A
1027	1900	1900	1900	1900	N/A	N/A	N/A
1057	1900	1900	1900	1900	N/A	N/A	N/A
1087	2000	1900	1900	1900	N/A	N/A	N/A
1118	2000	1900	1900	1900	N/A	N/A	N/A
1148	2000	1900	1900	1900	N/A	N/A	N/A
1178	2000	1900	2000	2000	N/A	N/A	N/A
1208	2000	1900	2000	2000	N/A	N/A	N/A
1239	2000	2000	2000	2000	N/A	N/A	N/A
1269			2000	2000	N/A	N/A	N/A

1299			2000	2000	N/A	N/A	N/A
1329			2000	2000	N/A	N/A	N/A
1359			2000	2000	N/A	N/A	N/A
1390					N/A	N/A	N/A
1420					N/A	N/A	N/A
1450					N/A	N/A	N/A
1480					N/A	N/A	N/A
1510					N/A	N/A	N/A
1541					N/A	N/A	N/A
1571					N/A	N/A	N/A

Appendix 4: FEM verification of uniform temperature distribution on the test horizontal substrate during joint formation evolution

The geometric model and meshed model for the test sample configuration are presented below.

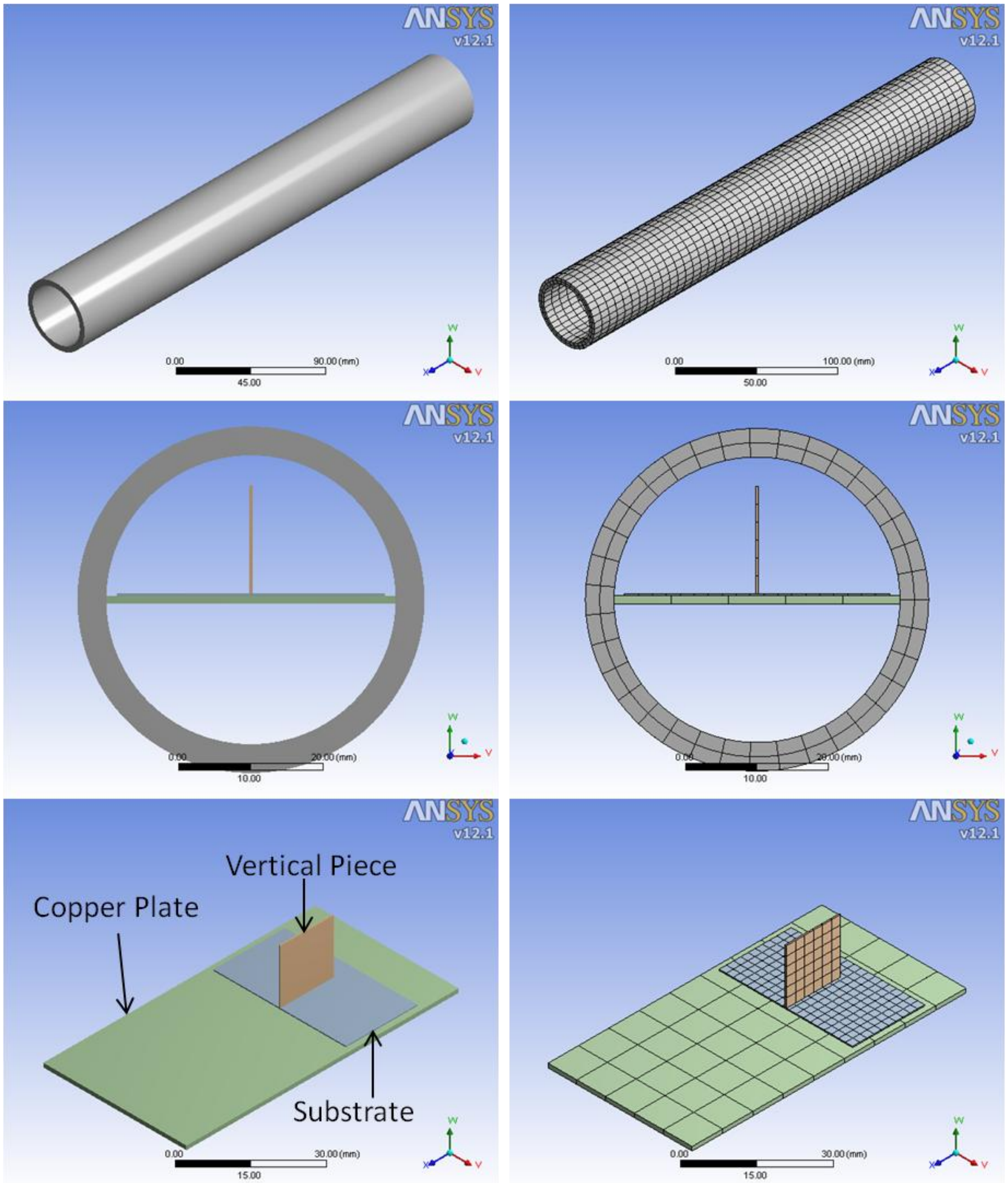

The temperature distribution on the substrate during the joining process between 850s and 1030s is shown in the following top view: (The probe represents the temperature of the substrate location where the thermocouple is positioned.)

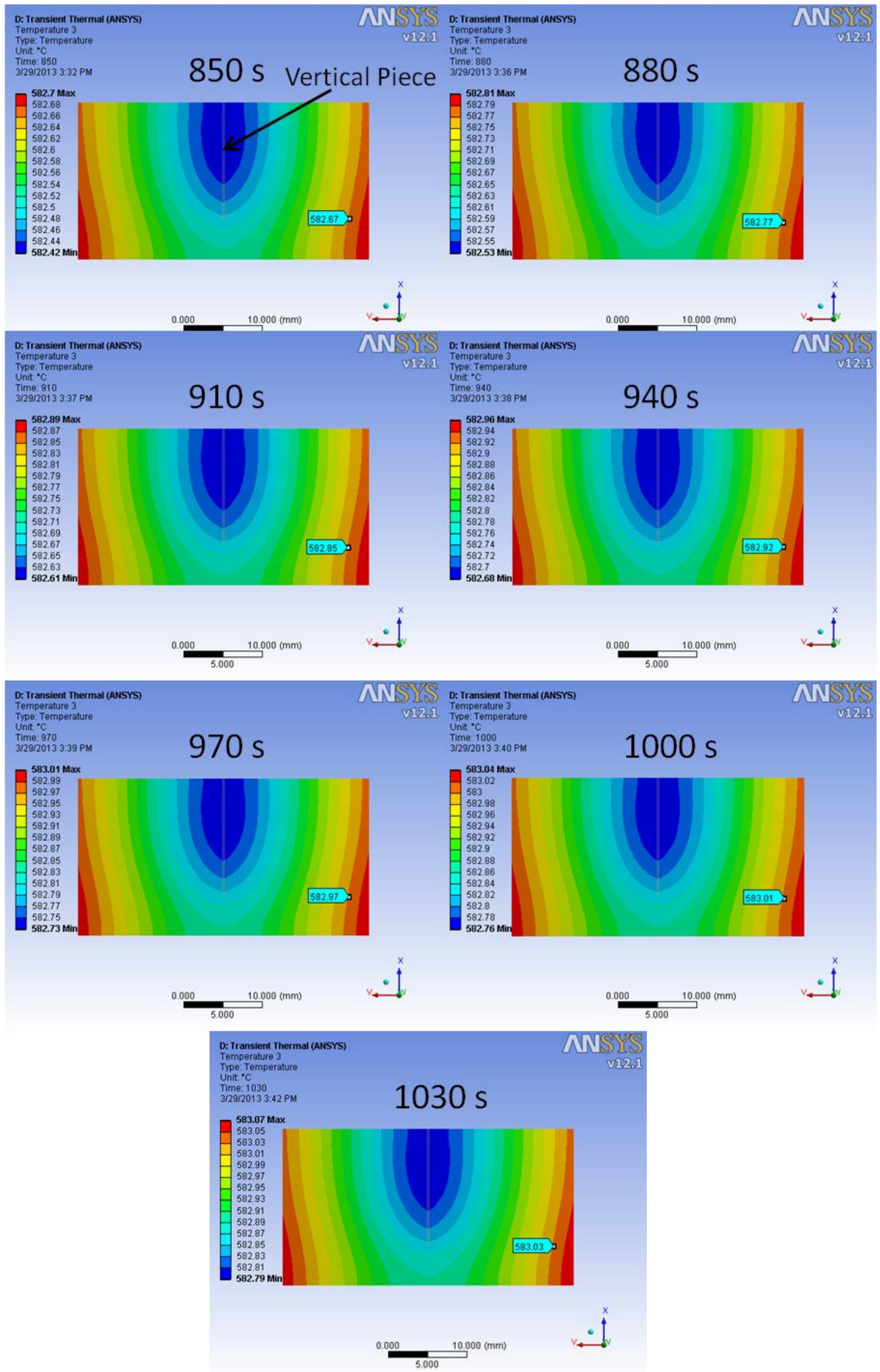

The properties of materials used related to this analysis are assumed to be constant and are summarized in the following table.

Parts	Material	Density (kg/m^3)	Thermal Conductivity (W/m·K)	Specific Heat (J/Kg·K)	Emissivity
Ceramic* Tube	96% Al_2O_3	3720	25	880	0.9
Copper Plate**	Copper	8933	401	385	0.78
Substrate**	AA3003 H24***	2730	171	880	0.2
Vertical Piece**	AA3003 H14***	2730	159	893	0.2

* http://www.makeitfrom.com/material-data/?for=96-Percent-Purity-Alumina

** Reference 52

*** http://www.scribd.com/doc/36719273

The average convective heat transfer coefficient of Nitrogen is 9.5 $W/m^2 \cdot °C$. It is based on an assumption of forced convection over the flat plate using the convection heat transfer correlations[52] for external flow with Laminar flow and $P_r > 0.6$ conditions. The atmosphere temperature (450 °C) in the ceramic tube is taken as the average built-in thermocouple (Figure 2.1) temperature throughout the test time. Thermal radiation is the dominant heat transfer in this model and is based on Stefan-Boltzmann Law[52]. Conduction part is based on heat diffusion equations. It is assumed in this analysis there is no radiation heat transfer exchange between surfaces composing the samples geometry inside the ceramic tubes (Only radiation exchange between ceramic tube inner surface and sample surfaces). ANSYS Thermal Solver used the following two equations to calculate the radiation heat transfer rate between two surfaces i and j and conduction in the respective components:

$$Q_i = \frac{1}{\left(\frac{1-\varepsilon_i}{A_i \varepsilon_i} + \frac{1}{A_i F_{ij}} + \frac{1-\varepsilon_j}{A_j \varepsilon_j}\right)} \sigma\left(T_i^4 - T_j^4\right)$$

$$\frac{\partial^2 T}{\partial x^2} + \frac{\partial^2 T}{\partial y^2} + \frac{\partial^2 T}{\partial z^2} = \frac{\rho_i c_{pi}}{K_i} \frac{\partial T}{\partial t}$$

Where,

Q_i = Radiation heat transfer rate between two surfaces, W,

ε_i, ε_i = effective emissivity of surface i and j,

F_{ji} = radiation view factors, defined as the fraction of total radiant energy that leaves surface i which arrives directly on surface j,

A_i, A_j = area of surface i and j, m^2,

σ = Stefan-Boltzmann constant,

T_i,T_j = absolute temperature of surface i and j, K,

K_i = Conductivity of each material, W/m·K.

The calculation is performed by ANSYS Thermal solver. The element type used in the modeling is SOLID90 with total elements 3967. The following figure shows the temperature profiles of the experimental measured thermocouple temperature and numerically determined temperature at the location that is coincident to the external thermocouple position during the joint evolution time. There is no obvious temperature non-uniformity on the substrate and due to the geometric symmetry of the sample configuration the thermocouple was positioned only in the one side of the substrate.

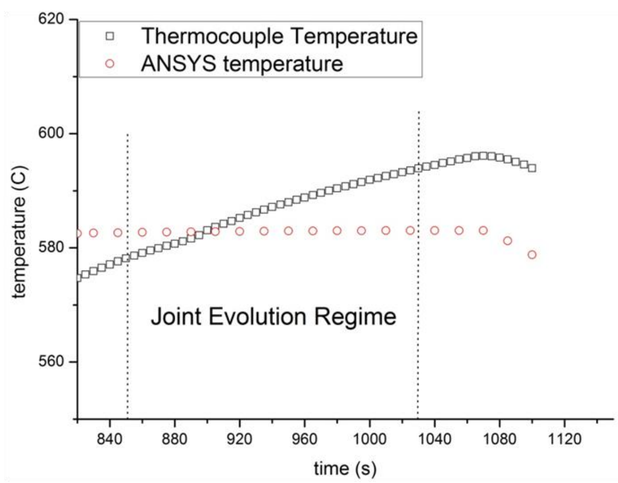

It can be clearly seen that there is a little difference (<1°C) between maximum and minimum temperature on the substrate during joining process. Hence, it is verified that the temperature distribution is virtually uniform during the period of the joint formation evolution. The temperature reading from the external thermocouple can be assumed to be the temperature at the joint location.

Appendix 5: External thermocouple temperature data for all tests

	Test1 _70	Test2 _70	Test3 _70	Test4 _70	Test5 _70	Test6 _70	Test7 _70	Test1 _200	Test2 _200	Test3 _200
time (s)	T (°C)	T (°C)	T (°C)	T (°C)	T (°C)	T (°C)	T (°C)	T (°C)	T (°C)	T (°C)
0	27	27	33	31	33	26	25	26	28	26
30	32	29	35	34	35	28	27	28	30	28
60	48	37	43	42	43	37	34	35	38	35
90	78	56	61	62	61	56	53	53	58	54
120	125	88	94	96	94	90	85	84	92	86
150	190	135	144	145	144	140	132	131	141	133
180	252	185	204	204	168	193	184	181	194	185
210	311	237	264	259	188	246	236	231	246	237
240	369	293	321	313	227	299	291	283	300	287
270	428	351	379	372	283	352	347	334	356	339
300	475	411	432	429	348	410	404	385	414	393
330	482	455	454	454	417	449	445	420	448	431
360	488	470	464	465	466	462	459	435	460	445
390	495	480	474	476	484	472	468	447	469	455
420	504	490	484	488	494	483	477	458	479	465
450	512	500	494	499	504	494	486	470	488	476
480	520	509	503	509	513	504	495	480	498	486
510	528	518	512	519	522	513	503	491	507	496
540	535	527	521	528	531	522	511	500	515	505
570	542	535	528	536	539	531	518	509	523	513
600	548	542	535	544	546	539	525	516	530	521
630	553	549	542	551	553	545	532	524	536	528
660	558	555	548	557	559	552	538	530	542	534
690	563	561	554	563	565	557	543	536	548	540
720	567	566	558	568	570	563	548	542	553	545
750	571	570	563	572	575	567	553	547	557	550
780	574	574	567	576	579	571	557	551	561	555
810	577	577	571	580	582	575	561	556	565	559
840	580	581	574	582	586	578	564	559	569	563
870	583	584	577	586	589	581	568	563	572	566
900	585	587	579	589	592	584	570	566	575	569
930	588	589	582	592	595	587	573	569	577	572
960	590	589	585	594	594	590	575	572	579	575
990	592	584	587	595	590	592	577	574	582	577
1020	593	577	589	592	584	594	580	576	584	579
1050	594	572	590	587	578	595	582	578	586	581
1080	590	566	587	581	572	594	584	580	584	583

1110	584	559	582	576	564	589	585	582	580	585
1140	578	553	576	569	558	584	583	584	575	585
1170	571	547	571	562	551	578	579	585	570	582
1200	565	540	564	555	544	572	573	584	563	577
1230	559	533	557	549	537	566	568	580	558	572
1260	552	527	551	542	531	559	561	575	554	566
1290	545	521	545	536	525	552	557	569	551	560
1320	537	515	538	529	518	546	553	563	548	553
1350	531	509	532	522	512	539	550	559	545	547
1380	524	503	525	516	506	533	547	556	543	541
1410	518	498	518	510	500	526	544	552	541	535
1440	512	492	512	504	495	520	542	547	539	529
1470	506	487	506	498	489	514	540	541	538	523
1500	501	482	500	493	484	508	539	535	537	518
1530	495	477	494	487	478	502	536	529	535	512
1560	490	472	489	482	473	496	531	523	531	506
1590	484	467	484	477	468	490	527	517	527	501
1620	479	462	478	472	463	485	522	511	522	495
1650	474	458	473	467	458	479	517	505	517	489
1680	469	453	468	462	453	474	511	500	512	484
1710	464	448	463	457	448	469	506	494	507	478
1740	459	444	458	452	444	464	501	489	502	473
1770	455	440	454	447	439	459	496	484	497	468
1800	450	435	449	443	435	455	491	479	492	462
1830	445	431	444	438	430	450	486	474	487	457
1860	441	427	440	434	426	445	482	469	482	453
1890	436	422	435	429	422	441	477	464	477	448
1920	432	418	431	425	417	436	472	460	472	443
1950	427	414	426	421	413	432	467	455	468	439
1980	423	410	422	416	409	427	463	450	463	434
2010	419	406	418	412	405	423	458	446	458	430
2040	415	402	414	408	401	419	454	441	454	426
2070	411	399	410	404	397	415	449	437	449	421
2100	407	395	405	400	393	411	445	433	445	417
2130	403	391	401	396	389	406	440	428	441	413
2160	399	387	397	392	386	402	436	424	437	409
2190	395	384	394	388	382	398	432	420	432	405
2220	391	380	390	384	378	394	428	416	428	401
2250	387	377	386	381	375	391	424	412	424	397
2280	383	373	382	377	371	387	419	408	420	393
2310	380	370	378	373	368	383	415	404	416	389

2340	376	366	375	369	364	379	412	400	412	385
2370	372	363	371	366	361	376	408	396	408	382
2400	369	359	367	362	357	372	404	392	404	378
2430	365		364	359	354	368	400	388	401	375
2460	362		361	355	351	365	396	385	397	371
2490	358		357	352	347	361	392	381	393	368
2520	355		354	348	344	358	389	377	389	364
2550	351		350	345	341	354	385	374	386	361
2580	348		347	342	338	351	381	370	382	357
2610	345		344	339	335	348	378	367	379	354
2640	341		341	335	332	344	374	363	375	343
2670	338		337	332	329	341	371	360	372	340
2700	335		334	329	326	338	367	357	369	337
2730	332		331	326	323	335	364	353	365	334
2760	328		328	323	320	331	360	350	362	331
2790	325		325	320	317	328	357	347	359	328
2820	322		322	317	315	325	354	344	356	325
2850	319		319	314	312	322	350	340	352	322
2880	316		316	311	309	319	347	337	349	319
2910	313		313	308	306	316	344	334	346	316
2940	310		310	305	304	313	341	331	343	313
2970	308		307	302	301	310	338	328	340	310
3000	305		304			307	335	325	337	308
3030	302		301			305	331	322	334	305
3060						302	329	319	331	302
3090							326	317	329	
3120							323	314	326	
3150							320	311	323	
3180							317	308	320	
3210							314	306	317	
3240							311	303	315	
3270							308	301	312	
3300							305		309	
3330							303		307	
3360									304	
3390									302	

	Test1_ 500	Test2_ 500	Test3_ 500	Test1_ 2000	Test2_ 2000	Test3_ 2000	Test4_ 2000	Test5_ 2000	Test6_ 2000	Test7_ 2000
time (s)	T (°C)	T (°C)	T (°C)	T (°C)	T (°C)	T (°C)	T (°C)	T (°C)	T (°C)	T (°C)
0	27	27	29	28	29	28	26	35	32	30

30	29	29	31	30	30	29	28	35	33	30
60	37	37	40	38	34	32	35	39	37	34
90	56	56	60	58	46	42	54	52	50	47
120	90	90	94	92	71	63	86	76	75	70
150	140	140	143	97	109	96	105	116	114	108
180	195	195	198	106	160	140	107	170	167	159
210	249	249	252	128	217	190	117	233	227	215
240	304	304	306	165	270	237	139	291	279	273
270	361	333	363	216	323	283	175	350	330	328
300	417	344	421	276	377	332	223	410	383	383
330	453	369	453	339	418	370	278	449	420	424
360	466	408	465	399	435	385	333	461	435	439
390	476	455	473	440	447	396	385	468	445	450
420	487	495	483	456	459	407	429	477	457	461
450	497	510	493	466	471	418	447	486	468	473
480	508	517	502	476	483	429	458	495	480	484
510	517	524	511	487	494	439	469	503	490	494
540	526	531	520	497	504	449	480	511	500	504
570	535	538	527	507	513	458	491	519	508	513
600	542	544	534	515	521	466	501	526	516	522
630	549	549	541	524	529	474	511	532	524	529
660	555	554	547	531	535	481	519	538	531	536
690	561	559	552	538	542	487	527	543	537	542
720	566	563	557	544	547	493	534	548	542	548
750	570	567	562	549	552	499	541	553	547	553
780	575	570	566	554	557	504	547	557	552	558
810	578	573	570	558	561	509	552	561	556	562
840	581	575	573	563	565	513	557	564	560	566
870	584	578	576	566	569	517	561	568	564	570
900	588	580	579	570	572	521	565	571	567	573
930	590	582	581	573	575	524	569	573	570	576
960	591	584	584	576	577	527	572	575	572	579
990	587	585	586	578	580	530	575	578	575	582
1020	582	585	583	581	582	533	578	580	577	584
1050	577	581	579	584	585	536	580	582	579	587
1080	570	577	573	586	586	538	583	584	582	589
1110	563	572	567	588	588	540	585	586	583	590
1140	559	566	561	588	587	542	556	587	585	588
1170	555	560	557	585	584	544	553	589	587	584
1200	552	554	553	581	579	546	550	590	588	579
1230	548	548	550	575	573	548	547	590	590	574

1260	546	543	547	569	567	549	545	586	590	567
1290	542	537	545	563	562	551	543	581	587	561
1320	537	531	543	559	558	552	542	576	582	555
1350	532	525	542	555	555	554	540	570	577	549
1380	526	520	540	552	552	555	535	563	572	543
1410	520	514	536	549	547	557	531	557	566	537
1440	514	508	531	547	542	558	526	551	562	531
1470	509	502	526	546	536	559	520	545	558	525
1500	503	496	521	544	531	563	515	539	555	519
1530	497	491	515	543	525	565	509	533	552	513
1560	492	486	509	542	519	566	503	527	547	507
1590	487	481	503	542	514	568	498	521	542	502
1620	482	476	498	541	508	570	492	514	536	496
1650	477	471	493	541	502	571	487	508	531	491
1680	472	467	487	540	497	573	482	503	525	486
1710	467	463	482	540	491	574	477	497	520	481
1740	462	391	477	540	486	575	472	492	514	476
1770	457	340	473	539	481	576	467	486	509	471
1800	453	323	468	539	476	577	463	481	503	467
1830	448	311	463	539	471	577	458	476	498	462
1860	443	303	458	539	467	578	454	472	493	458
1890	439		454	539	462	577	449	467	488	453
1920	434		449	539	457	574	445	462	483	449
1950	430		445	539	453	570	440	457	478	444
1980	426		440	539	448	565	436	453	474	440
2010	422		436	539	444	559	432	448	470	436
2040	417		432	539	439	554	427	444	465	432
2070	413		428	539	435	549	423	440	461	428
2100	409		423	539	431	543	419	435	456	424
2130	405		419	539	426	537	415	431	451	420
2160	401		415	538	422	532	411	427	446	416
2190	398		411	537	418	526	407	423	442	412
2220	394		407	535	414	520	403	419	437	409
2250	390		403	531	410	515	399	415	433	405
2280	386		399	526	406	510	395	411	429	401
2310	383		395	522	402	504	391	407	425	398
2340	379		392	517	398	499	388	403	421	394
2370	375		388	512	394	494	384	399	417	391
2400	372		384	508	390	489	380	400	413	387
2430	368		380	503	386	485	377	360	409	384
2460	365		377	498	383	480	373		405	380

2490	362		373	494	379	475	369		401	377
2520	358		370	489	375	471	366		397	373
2550	355		366	484	372	466	366		394	370
2580	352		366	479	368	462	318		390	367
2610	349		327	475	365	457			386	364
2640	345			470	361	453			383	360
2670	342			466	358	448			379	357
2700	339			461	354	444			375	354
2730	336			457	351	440			372	351
2760	333			453	348	435			368	348
2790	330			448	345	431			365	345
2820	327			444	341	427			361	342
2850	324			440	338	423			358	339
2880	322			436	335	419			354	336
2910	319			432	332	415			351	334
2940	316			428	329	411			348	331
2970	313			424	326	407			344	328
3000	311			420	323	403			341	325
3030	308			416	321	399			338	323
3060	305			412	318	399			335	
3090	303			408	315	355			332	
3120	300			404	312				328	
3150				400	310				325	
3180				396	302				314	
3210				393						
3240				389						
3270				386						
3300				382						
3330				378						
3360				375						
3390				371						
3420				368						
3450				365						
3480				361						
3510				358						
3540				355						
3570				351						
3600				348						
3630				345						
3660				342						
3690				339						

3720				336						
3750				333						
3780				330						
3810				327						
3840				324						
3870				321						
3900				318						
3930				315						
3960				312						
3990				309						
4020				307						
4050				304						
4080				301						

	Test8 _2000	Test9 _2000	Test10 _2000	Test11 _2000	Test1 _CA	Test2 _CA	Test3 _CA
time (s)	T (°C)	T (°C)	T (°C)	T (°C)	T (°C)	T (°C)	T (°C)
0	30	30	30	30	25	35	32
30	31	31	31	31	25	35	32
60	36	34	36	36	27	39	35
90	50	48	51	51	35	52	46
120	79	74	80	80	52	76	66
150	125	116	123	123	80	116	100
180	183	173	179	179	122	170	145
210	247	237	237	237	173	233	198
240	302	296	289	289	227	291	246
270	358	351	343	343	278	350	294
300	416	408	400	400	329	410	343
330	458	449	439	439	370	449	381
360	473	464	454	454	386	461	396
390	483	474	464	464	394	468	407
420	494	485	476	476	403	477	418
450	505	496	488	488	412	486	430
480	516	506	499	499	421	495	441
510	527	516	509	509	430	503	452
540	536	525	519	519	438	511	462
570	545	534	527	527	446	519	471
600	553	542	535	535	454	526	480
630	560	549	542	542	461	532	488
660	566	555	549	549	467	538	495

690	572	561	555	555	474	543	501
720	577	566	560	560	479	548	508
750	581	571	565	565	485	553	513
780	586	576	569	569	489	557	518
810	590	579	573	573	494	561	523
840	594	582	577	577	498	564	528
870	597	586	580	580	502	568	532
900	600	590	583	583	506	571	535
930	600	592	586	586	509	573	539
960	597	595	589	589	512	575	542
990	591	595	591	591	515	578	545
1020	585	591	593	593	518	580	548
1050	579	586	595	595	521	582	550
1080	573	580	596	596	523	584	553
1110	565	575	593	593	525	586	555
1140	558	567	588	588	528	587	557
1170	552	561	582	582	530	589	559
1200	545	554	576	576	531	590	560
1230	539	548	570	570	533	590	562
1260	532	541	563	563	536	586	564
1290	526	535	556	556	537	581	565
1320	520	529	550	550	539	576	567
1350	514	523	544	544	541	570	568
1380	507	516	538	538	542	563	569
1410	501	510	531	531	544	557	570
1440	496	504	525	525	546	551	571
1470	490	498	519	519	547	545	572
1500	485	493	513	513	548	539	573
1530	479	487	508	508	549	533	574
1560	474	482	502	502	551	527	575
1590	469	476	496	496	552	521	576
1620	464	471	490	490	553	514	576
1650	459	466	485	485	553	508	577
1680	454	462	480	480	554	503	578
1710	450	457	475	475	555	497	579
1740	445	452	470	470	556	492	579
1770	440	447	465	465	557	486	580
1800	436	443	460	460	556	481	580
1830	431	438	455	455	558	476	581
1860	427	434	451	451	558	472	581
1890	423	430	446	446	556	467	582

1920	419	425	442	442	562	462	582
1950	414	421	438	438	565	457	582
1980	410	417	434	433	566	453	583
2010	406	413	431	429	566	448	583
2040	402	408	427	425	567	444	584
2070	398	404	423	421	568	440	584
2100	394	400	419	417	569	435	584
2130	391	397	416	413	570	431	585
2160	387	393	412	409	571	427	585
2190	383	389	408	405	571	423	585
2220	380	385	405	401	572	419	583
2250	376	382	401	398	572	415	579
2280	372	378	398	391	572	411	575
2310	369	375	395	326	572	407	570
2340	365	371	391		572	403	564
2370	362	368	388		572	399	559
2400	359	364	385		573	400	554
2430	355	361	381		574	360	549
2460	352	358	378		575	294	543
2490	349	354	375		576		538
2520	346	351	372		576		533
2550	343	348	369		577		527
2580	340	346	366		577		522
2610	337	342	363		578		516
2640	334	339	360		578		510
2670	331	336	357		578		505
2700	328	333	354		579		499
2730	325	331	351		578		494
2760	322	328	348		575		489
2790	319	325	345		571		484
2820	316	322	342		566		479
2850	314	319	340		561		475
2880	311	316	337		556		470
2910	308	314	334		551		466
2940	306	311	331		546		461
2970	303	308	329		541		457
3000	300	306	326		536		453
3030		303	324		531		449
3060		301	321		526		445
3090			319		520		441
3120			316		515		437

3150			314		509		433
3180			311		504		429
3210			309		499		425
3240			306		494		422
3270			304		489		418
3300			302		485		414
3330					480		411
3360					476		407
3390					471		404
3420					467		400
3450					462		397
3480					458		393
3510					454		390
3540					450		387
3570					446		383
3600					442		380
3630					438		377
3660					434		374
3690					430		371
3720					427		367
3750					423		364
3780					419		361
3810					415		358
3840					412		355
3870					408		353
3900					405		350
3930					401		347
3960					398		344
3990					395		341
4020					391		338
4050					388		336
4080					385		333
4110					381		330
4140					378		328
4170					375		325
4200					372		323
4230					369		320
4260					366		318
4290					363		315
4320					360		313
4350					357		310

4380					354		308
4410					351		305
4440					349		303
4470					346		301
4500					343		
4530					340		
4560					338		
4590					335		
4620					332		
4650					330		
4680					327		
4710					324		
4740					322		
4770					319		
4800					317		
4830					314		
4860					312		
4890					310		
4920					307		
4950					305		
4980					302		
5010					300		

Appendix 6: Uncertainty determination of kinetics data

The uncertainty of measured triple line location for a certain test group at each recorded time specified in 3.3.1 is considered to be related to standard deviation based on the number of tests in each group conducted (Precision Index[60]). The uncertainty of measurement for a particular test within that test group is hard to define since the measurement (Figure 3.8 and Figure 3.10) uncertainties are heavily dependent on baseline selection in each test (Bias Error[60]).

Hence, the triple line location for a certain test group can be expressed as:

$$L_{V\ (H)} = L_{Avg} \pm U$$

Where,

$L_{V(H)}$ = Vertical or horizontal triple line location for a certain test group,

L_{Avg} = Average triple line location from the measurements at each test performed in a particular test group:

$$L_{Avg} = \frac{\sum_1^n L_n}{n}$$

Where,

L_n = measured vertical or horizontal triple line location for each test in the test group,

n = Number of tests performed in the particular test group,

U = Uncertainties of each test group:

$$U^{60} = \sqrt{\frac{\sum_1^n (L_n - L_{Avg})^2}{n}}$$

Appendix 7: One set of extracted pictures representing joint formation evolution for each test group

Test5_70

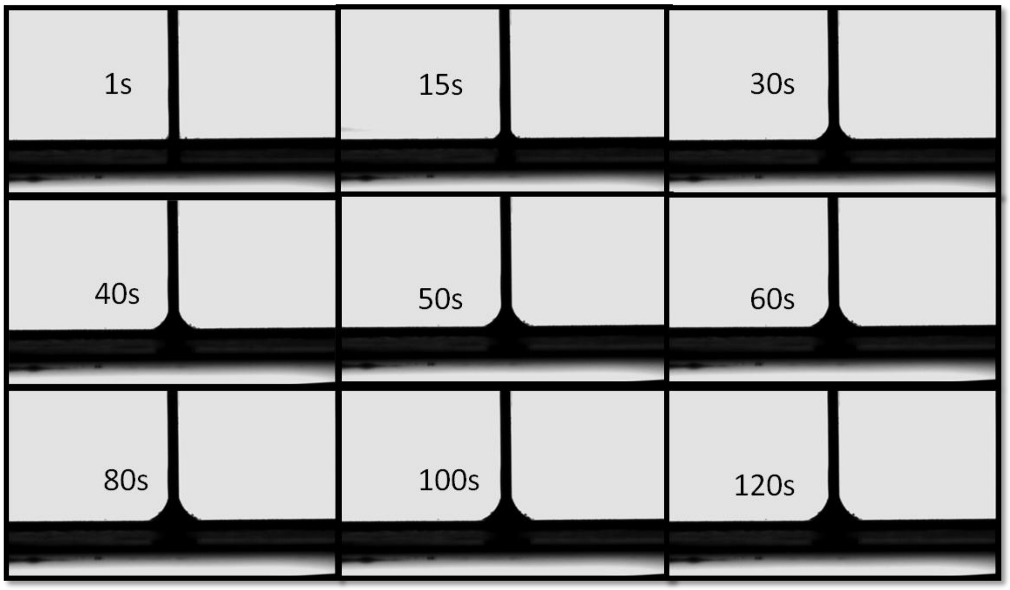

Test2_200

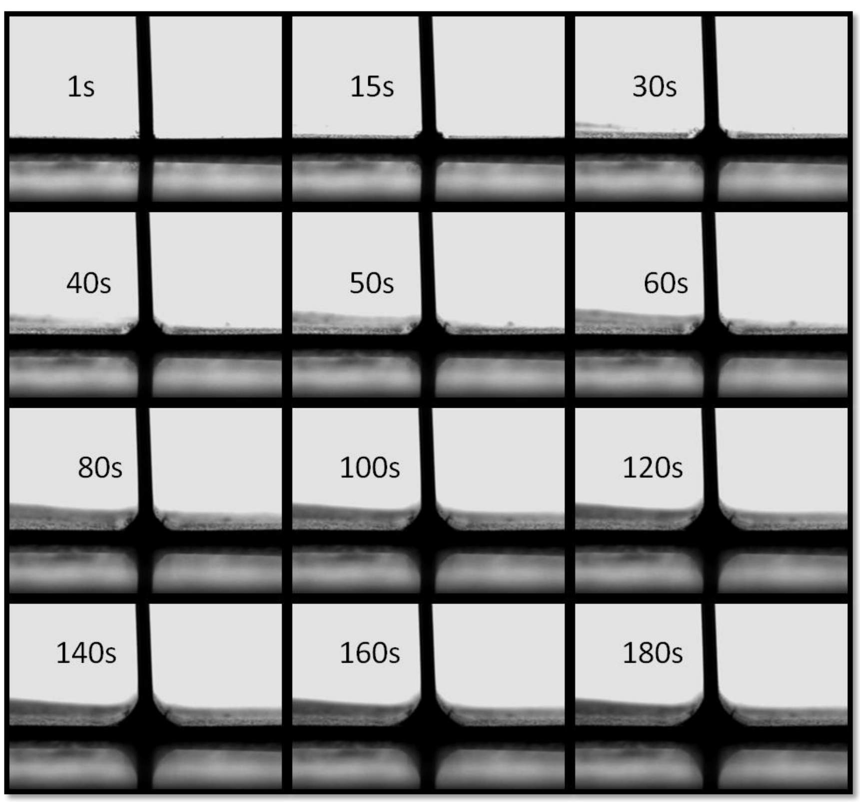

Test2_500

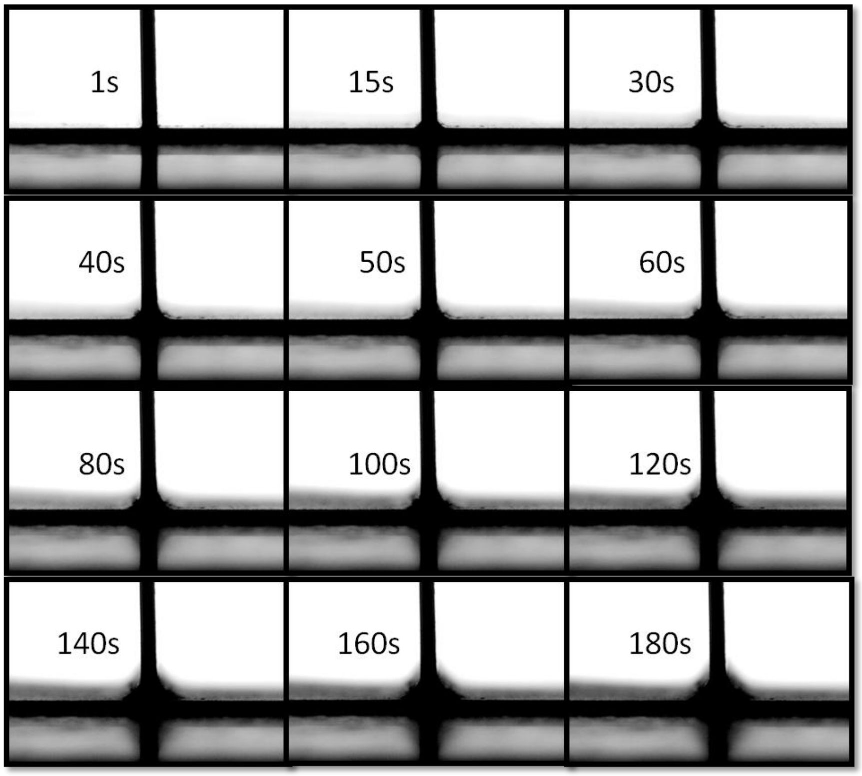

Test9_2000

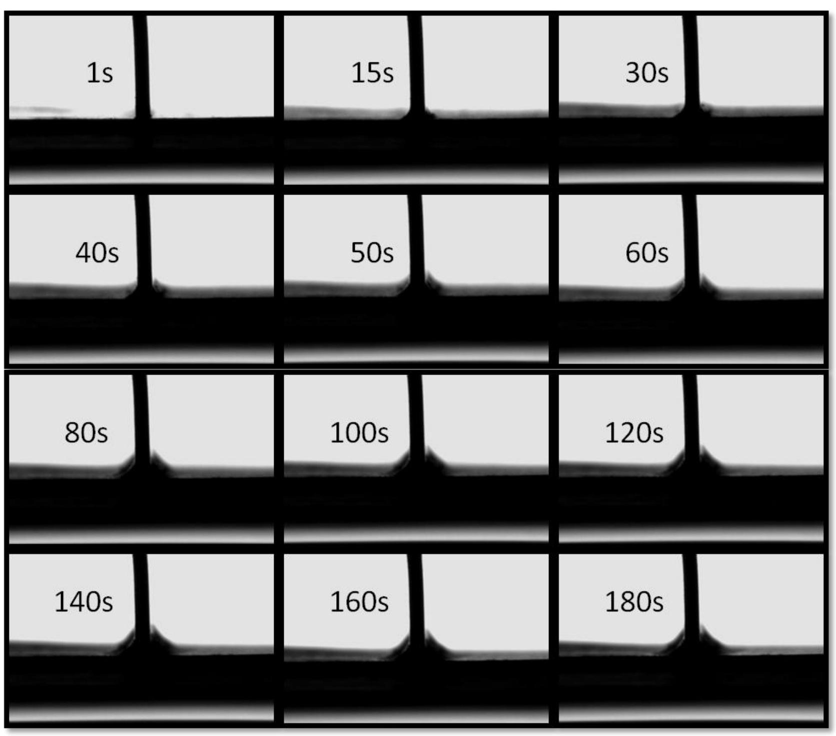

Appendix 8: Dimensional and normalized kinetics data for all tests

Dimensional data:

	Test1_ 70	Test1_ 70	Test1_ 70	Test1_ 70	Test2_ 70	Test2_ 70	Test2_ 70	Test2_ 70
	LEFT	LEFT	RIGHT	RIGHT	LEFT	LEFT	RIGHT	RIGHT
Time (s)	LV (mm)	LH (mm)	LV (mm)	LH (mm)	LV (mm)	LH (mm)	LV (mm)	LH (mm)
0	0.000	0.000	0.000	0.000	0.000	0.000	0.000	0.000
1	0.061	0.046	0.061	0.077	0.040	0.000	0.040	0.040
2	0.077	0.108	0.123	0.108	0.080	0.040	0.040	0.060
3	0.169	0.169	0.154	0.123	0.080	0.040	0.100	0.080
4	0.184	0.184	0.169	0.169	0.080	0.040	0.100	0.080
5	0.200	0.246	0.184	0.169	0.080	0.100	0.140	0.120
6	0.231	0.246	0.200	0.200	0.010	0.100	0.140	0.120
7	0.246	0.262	0.215	0.230	0.120	0.140	0.140	0.140
8	0.246	0.277	0.277	0.292	0.140	0.160	0.160	0.140
9	0.261	0.292	0.277	0.323	0.140	0.160	0.180	0.160
10	0.307	0.292	0.277	0.323	0.160	0.200	0.180	0.200
11	0.307	0.308	0.307	0.323	0.160	0.200	0.200	0.200
12	0.307	0.323	0.323	0.338	0.180	0.200	0.220	0.200
13	0.354	0.354	0.323	0.354	0.220	0.220	0.220	0.220
14	0.354	0.354	0.338	0.354	0.240	0.240	0.240	0.240
15	0.369	0.354	0.338	0.369	0.260	0.280	0.260	0.240
16	0.384	0.354	0.369	0.384	0.260	0.280	0.260	0.260
17	0.384	0.400	0.369	0.400	0.280	0.280	0.260	0.260
18	0.400	0.415	0.385	0.415	0.280	0.280	0.280	0.260
19	0.400	0.446	0.385	0.446	0.300	0.300	0.300	0.280
20	0.415	0.461	0.385	0.461	0.300	0.300	0.300	0.280
21	0.415	0.461	0.400	0.477	0.320	0.300	0.300	0.320
22	0.430	0.492	0.400	0.492	0.340	0.320	0.320	0.320
23	0.446	0.477	0.415	0.492	0.360	0.340	0.340	0.360
24	0.446	0.477	0.430	0.507	0.360	0.380	0.340	0.380
25	0.461	0.492	0.430	0.507	0.380	0.380	0.360	0.380
26	0.477	0.507	0.446	0.508	0.380	0.380	0.360	0.380
27	0.477	0.508	0.461	0.523	0.380	0.380	0.360	0.400
28	0.477	0.523	0.461	0.523	0.380	0.400	0.380	0.400
29	0.492	0.523	0.477	0.523	0.400	0.401	0.380	0.400
30	0.507	0.523	0.492	0.554	0.420	0.420	0.400	0.400
32	0.507	0.554	0.492	0.554	0.420	0.420	0.420	0.420

34	0.538	0.554	0.507	0.554	0.420	0.440	0.420	0.440
36	0.569	0.554	0.538	0.569	0.440	0.440	0.420	0.480
38	0.569	0.585	0.553	0.600	0.460	0.480	0.440	0.480
40	0.584	0.600	0.553	0.600	0.480	0.480	0.440	0.480
42	0.584	0.616	0.600	0.615	0.480	0.480	0.460	0.500
44	0.584	0.630	0.600	0.615	0.500	0.500	0.460	0.500
46	0.600	0.630	0.615	0.615	0.500	0.500	0.500	0.520
48	0.630	0.646	0.630	0.630	0.500	0.500	0.500	0.540
50	0.630	0.661	0.646	0.646	0.520	0.520	0.520	0.540
52	0.646	0.677	0.661	0.676	0.520	0.520	0.520	0.560
54	0.661	0.692	0.661	0.677	0.540	0.560	0.540	0.560
56	0.707	0.723	0.692	0.692	0.540	0.540	0.580	0.560
58	0.723	0.739	0.707	0.707	0.540	0.560	0.580	0.600
60	0.738	0.754	0.707	0.723	0.560	0.600	0.600	0.600
63	0.753	0.769	0.738	0.753	0.600	0.640	0.620	0.640
66	0.769	0.784	0.738	0.784	0.620	0.680	0.620	0.680
69	0.784	0.785	0.738	0.800	0.640	0.680	0.640	0.700
72	0.784	0.800	0.753	0.815	0.660	0.700	0.680	0.740
75	0.815	0.815	0.784	0.830	0.680	0.720	0.680	0.740
78	0.830	0.831	0.799	0.846	0.720	0.740	0.700	0.760
81	0.846	0.847	0.799	0.846	0.740	0.740	0.720	0.760
84	0.846	0.862	0.815	0.861	0.760	0.760	0.740	0.780
87	0.846	0.876	0.815	0.861	0.780	0.780	0.760	0.780
90	0.846	0.877	0.830	0.876	0.780	0.780	0.760	0.780
95	0.876	0.877	0.830	0.876	0.780	0.780	0.780	0.780
100	0.876	0.893	0.830	0.876	0.780	0.780	0.800	0.780
105	0.876	0.893	0.846	0.876	0.780	0.780	0.800	0.780
110	0.876	0.908	0.846	0.877	0.780	0.780	0.800	0.780
115	0.876	0.908	0.846	0.877	0.780	0.800	0.800	0.780
120	0.876	0.908	0.846	0.877	0.800	0.800	0.800	0.780

	Test3_70	Test3_70	Test3_70	Test3_70	Test4_70	Test4_70	Test4_70	Test4_70
	LEFT	LEFT	RIGHT	RIGHT	LEFT	LEFT	RIGHT	RIGHT
Time (s)	LV (mm)	LH (mm)	LV (mm)	LH (mm)	LV (mm)	LH (mm)	LV (mm)	LH (mm)
0	0.000	0.000	0.000	0.000	0.000	0.000	0.000	0.000
1	0.064	0.048	0.080	0.080	0.029	0.029	0.014	0.029
2	0.064	0.048	0.096	0.080	0.057	0.029	0.043	0.043
3	0.080	0.064	0.096	0.080	0.071	0.043	0.043	0.043
4	0.096	0.064	0.096	0.112	0.071	0.057	0.057	0.043

5	0.096	0.064	0.112	0.128	0.071	0.057	0.057	0.057
6	0.112	0.080	0.112	0.112	0.086	0.057	0.057	0.057
7	0.112	0.096	0.112	0.112	0.086	0.057	0.071	0.073
8	0.128	0.128	0.128	0.128	0.100	0.071	0.071	0.086
9	0.144	0.144	0.128	0.144	0.100	0.071	0.086	0.086
10	0.160	0.176	0.128	0.144	0.100	0.071	0.087	0.086
11	0.192	0.176	0.144	0.144	0.114	0.086	0.087	0.100
12	0.192	0.176	0.144	0.144	0.114	0.086	0.101	0.100
13	0.224	0.208	0.176	0.176	0.114	0.114	0.129	0.129
14	0.240	0.224	0.208	0.208	0.129	0.129	0.129	0.129
15	0.272	0.240	0.224	0.240	0.143	0.143	0.144	0.143
16	0.272	0.256	0.256	0.240	0.143	0.143	0.144	0.157
17	0.288	0.256	0.256	0.240	0.171	0.157	0.157	0.171
18	0.304	0.288	0.256	0.272	0.172	0.186	0.157	0.186
19	0.304	0.304	0.272	0.272	0.200	0.200	0.186	0.200
20	0.320	0.304	0.288	0.288	0.200	0.200	0.186	0.214
21	0.320	0.304	0.304	0.304	0.214	0.214	0.201	0.229
22	0.336	0.336	0.320	0.304	0.214	0.243	0.215	0.243
23	0.352	0.336	0.320	0.320	0.243	0.243	0.243	0.257
24	0.368	0.336	0.336	0.336	0.257	0.243	0.258	0.257
25	0.384	0.352	0.336	0.336	0.257	0.271	0.272	0.271
26	0.384	0.368	0.352	0.352	0.271	0.272	0.272	0.271
27	0.400	0.368	0.352	0.352	0.300	0.286	0.300	0.300
28	0.416	0.384	0.368	0.384	0.314	0.329	0.300	0.314
29	0.416	0.400	0.368	0.400	0.315	0.343	0.329	0.343
30	0.416	0.400	0.384	0.416	0.329	0.343	0.329	0.343
32	0.448	0.432	0.416	0.416	0.329	0.357	0.343	0.357
34	0.448	0.432	0.416	0.416	0.357	0.386	0.371	0.372
36	0.448	0.432	0.432	0.432	0.386	0.386	0.371	0.371
38	0.464	0.432	0.432	0.432	0.400	0.400	0.400	0.386
40	0.480	0.448	0.448	0.464	0.414	0.415	0.429	0.429
42	0.496	0.464	0.464	0.480	0.443	0.429	0.457	0.443
44	0.496	0.464	0.464	0.480	0.457	0.457	0.471	0.443
46	0.512	0.464	0.480	0.480	0.486	0.457	0.471	0.471
48	0.512	0.480	0.480	0.480	0.486	0.471	0.500	0.486
50	0.528	0.496	0.496	0.496	0.529	0.486	0.514	0.500
52	0.528	0.496	0.496	0.496	0.529	0.500	0.529	0.529
54	0.560	0.496	0.496	0.512	0.557	0.514	0.557	0.557
56	0.560	0.512	0.528	0.528	0.586	0.543	0.586	0.586
58	0.576	0.512	0.528	0.528	0.614	0.586	0.600	0.586
60	0.576	0.528	0.544	0.544	0.614	0.600	0.614	0.600

63	0.576	0.544	0.560	0.544	0.629	0.600	0.643	0.629
66	0.592	0.560	0.576	0.560	0.643	0.614	0.686	0.629
69	0.608	0.576	0.592	0.576	0.671	0.643	0.700	0.643
72	0.624	0.592	0.592	0.592	0.686	0.671	0.700	0.657
75	0.624	0.624	0.608	0.592	0.714	0.714	0.714	0.671
78	0.640	0.640	0.608	0.608	0.729	0.714	0.729	0.714
81	0.672	0.640	0.640	0.640	0.743	0.729	0.771	0.729
84	0.704	0.640	0.656	0.656	0.771	0.743	0.786	0.757
87	0.736	0.656	0.688	0.672	0.786	0.771	0.786	0.771
90	0.736	0.688	0.704	0.688	0.786	0.771	0.814	0.786
95	0.736	0.688	0.704	0.704	0.800	0.786	0.814	0.786
100	0.736	0.704	0.720	0.720	0.814	0.800	0.829	0.814
105	0.736	0.704	0.720	0.720	0.814	0.800	0.829	0.814
110	0.736	0.704	0.720	0.720	0.814	0.800	0.829	0.814
115	0.736	0.704	0.720	0.720	0.816	0.800	0.829	0.816
120	0.736	0.704	0.720	0.720	0.816	0.800	0.829	0.816

	Test5_ 70	Test5_ 70	Test5_ 70	Test5_ 70	Test6_ 70	Test6_ 70	Test6_ 70	Test6_ 70
	LEFT	LEFT	RIGHT	RIGHT	LEFT	LEFT	RIGHT	RIGHT
Time (s)	LV (mm)	LH (mm)	LV (mm)	LH (mm)	LV (mm)	LH (mm)	LV (mm)	LH (mm)
0	0.000	0.000	0.000	0.000	0.000	0.000	0.000	0.000
1	0.015	0.046	0.031	0.015	0.018	0.018	0.000	0.000
2	0.046	0.046	0.046	0.031	0.036	0.018	0.018	0.018
3	0.062	0.046	0.046	0.031	0.057	0.041	0.018	0.018
4	0.077	0.062	0.077	0.062	0.057	0.057	0.018	0.018
5	0.092	0.077	0.108	0.077	0.073	0.073	0.036	0.036
6	0.108	0.092	0.108	0.077	0.075	0.073	0.055	0.055
7	0.123	0.123	0.123	0.092	0.091	0.073	0.075	0.073
8	0.123	0.123	0.123	0.123	0.111	0.111	0.111	0.109
9	0.154	0.138	0.138	0.138	0.127	0.127	0.127	0.127
10	0.185	0.169	0.154	0.154	0.127	0.129	0.145	0.127
11	0.185	0.185	0.185	0.185	0.127	0.147	0.165	0.164
12	0.215	0.200	0.215	0.200	0.147	0.164	0.182	0.183
13	0.246	0.231	0.231	0.231	0.165	0.183	0.218	0.219
14	0.277	0.246	0.262	0.246	0.182	0.201	0.218	0.219
15	0.292	0.262	0.292	0.277	0.200	0.201	0.237	0.237
16	0.308	0.277	0.308	0.292	0.218	0.219	0.255	0.255
17	0.308	0.308	0.338	0.323	0.237	0.237	0.273	0.273
18	0.323	0.323	0.354	0.338	0.237	0.255	0.291	0.291

19	0.338	0.354	0.385	0.369	0.255	0.255	0.309	0.310
20	0.354	0.369	0.385	0.369	0.273	0.291	0.309	0.310
21	0.385	0.385	0.400	0.369	0.273	0.291	0.327	0.327
22	0.400	0.416	0.431	0.385	0.273	0.309	0.327	0.327
23	0.400	0.416	0.431	0.400	0.309	0.327	0.345	0.346
24	0.415	0.431	0.446	0.431	0.327	0.345	0.345	0.364
25	0.431	0.446	0.462	0.446	0.345	0.364	0.364	0.364
26	0.462	0.477	0.492	0.446	0.364	0.382	0.364	0.400
27	0.477	0.477	0.492	0.462	0.364	0.400	0.382	0.400
28	0.508	0.477	0.492	0.492	0.382	0.400	0.400	0.400
29	0.523	0.492	0.523	0.492	0.382	0.400	0.400	0.418
30	0.523	0.508	0.538	0.508	0.400	0.419	0.400	0.418
32	0.538	0.508	0.569	0.538	0.400	0.418	0.418	0.419
34	0.569	0.538	0.569	0.538	0.400	0.418	0.418	0.436
36	0.600	0.554	0.600	0.554	0.418	0.419	0.418	0.436
38	0.600	0.569	0.600	0.585	0.436	0.437	0.437	0.455
40	0.615	0.600	0.631	0.600	0.436	0.438	0.437	0.473
42	0.631	0.631	0.631	0.631	0.436	0.455	0.455	0.473
44	0.631	0.631	0.662	0.646	0.455	0.473	0.473	0.509
46	0.662	0.646	0.662	0.662	0.455	0.491	0.473	0.509
48	0.677	0.662	0.677	0.662	0.473	0.491	0.491	0.545
50	0.677	0.662	0.692	0.677	0.491	0.509	0.509	0.545
52	0.692	0.677	0.723	0.708	0.527	0.527	0.509	0.545
54	0.708	0.692	0.723	0.723	0.527	0.546	0.528	0.546
56	0.738	0.723	0.738	0.723	0.545	0.565	0.546	0.564
58	0.769	0.738	0.754	0.723	0.564	0.582	0.582	0.600
60	0.769	0.754	0.754	0.738	0.564	0.582	0.600	0.618
63	0.785	0.769	0.754	0.738	0.600	0.618	0.600	0.655
66	0.785	0.769	0.769	0.754	0.618	0.636	0.637	0.655
69	0.785	0.769	0.769	0.754	0.655	0.655	0.655	0.673
72	0.785	0.769	0.785	0.754	0.655	0.655	0.655	0.691
75	0.785	0.785	0.785	0.769	0.673	0.673	0.691	0.691
78	0.785	0.785	0.785	0.769	0.673	0.673	0.691	0.727
81	0.800	0.785	0.800	0.785	0.673	0.691	0.709	0.728
84	0.800	0.785	0.800	0.785	0.691	0.691	0.727	0.745
87	0.800	0.785	0.815	0.785	0.709	0.727	0.745	0.745
90	0.800	0.800	0.816	0.800	0.727	0.746	0.745	0.745
95	0.815	0.800	0.816	0.800	0.745	0.764	0.745	0.745
100	0.815	0.800	0.816	0.800	0.746	0.764	0.745	0.782
105	0.815	0.800	0.831	0.800	0.764	0.764	0.764	0.782
110	0.816	0.800	0.831	0.800	0.764	0.782	0.782	0.782

115	0.816	0.800	0.831	0.800	0.782	0.782	0.782	0.782
120	0.816	0.800	0.831	0.800	0.782	0.782	0.782	0.782

	Test7_70	Test7_70	Test7_70	Test7_70
	LEFT	LEFT	RIGHT	RIGHT
Time (s)	LV (mm)	LH (mm)	LV (mm)	LH (mm)
0	0.000	0.000	0.000	0.000
1	0.060	0.060	0.020	0.040
2	0.080	0.080	0.040	0.080
3	0.080	0.080	0.080	0.080
4	0.080	0.100	0.080	0.100
5	0.100	0.100	0.080	0.100
6	0.100	0.140	0.080	0.080
7	0.100	0.140	0.100	0.100
8	0.120	0.140	0.120	0.100
9	0.120	0.140	0.160	0.120
10	0.140	0.160	0.180	0.140
11	0.160	0.160	0.200	0.180
12	0.160	0.180	0.200	0.200
13	0.180	0.180	0.220	0.220
14	0.180	0.200	0.220	0.220
15	0.200	0.220	0.240	0.240
16	0.240	0.220	0.240	0.240
17	0.240	0.240	0.240	0.260
18	0.240	0.240	0.260	0.280
19	0.240	0.260	0.260	0.280
20	0.240	0.280	0.260	0.300
21	0.260	0.280	0.280	0.300
22	0.260	0.281	0.300	0.320
23	0.260	0.300	0.320	0.320
24	0.280	0.300	0.340	0.340
25	0.280	0.300	0.340	0.340
26	0.300	0.321	0.360	0.340
27	0.300	0.321	0.360	0.360
28	0.300	0.341	0.360	0.360
29	0.320	0.341	0.380	0.360
30	0.320	0.360	0.380	0.380
32	0.340	0.361	0.380	0.380
34	0.360	0.380	0.400	0.380
36	0.380	0.400	0.400	0.400
38	0.400	0.400	0.400	0.420

40	0.420	0.400	0.420	0.420
42	0.420	0.420	0.420	0.420
44	0.440	0.440	0.440	0.440
46	0.440	0.460	0.440	0.440
48	0.440	0.460	0.460	0.460
50	0.460	0.460	0.460	0.460
52	0.460	0.460	0.480	0.460
54	0.460	0.480	0.480	0.480
56	0.480	0.480	0.500	0.480
58	0.480	0.480	0.500	0.500
60	0.480	0.500	0.520	0.500
63	0.500	0.500	0.520	0.520
66	0.500	0.500	0.540	0.540
69	0.520	0.520	0.540	0.540
72	0.520	0.520	0.540	0.560
75	0.540	0.540	0.560	0.560
78	0.540	0.540	0.560	0.560
81	0.540	0.560	0.560	0.560
84	0.560	0.580	0.580	0.580
87	0.560	0.580	0.580	0.580
90	0.580	0.580	0.580	0.580
95	0.600	0.600	0.600	0.600
100	0.600	0.600	0.620	0.620
105	0.620	0.640	0.640	0.640
110	0.640	0.660	0.660	0.660
115	0.660	0.680	0.680	0.680
120	0.660	0.680	0.700	0.700

	Test1_ 200	Test1_ 200	Test1_ 200	Test1_ 200	Test2_ 200	Test2_ 200	Test2_ 200	Test2_ 200
	LEFT	LEFT	RIGHT	RIGHT	LEFT	LEFT	RIGHT	RIGHT
Time (s)	LV (mm)	LH (mm)	LV (mm)	LH (mm)	LV (mm)	LH (mm)	LV (mm)	LH (mm)
0	0.000	0.000	0.000	0.000	0.000	0.000	0.000	0.000
1	0.017	0.017	0.033	0.017	0.019	0.019	0.038	0.043
2	0.033	0.033	0.050	0.033	0.019	0.019	0.076	0.060
3	0.050	0.050	0.067	0.067	0.038	0.027	0.114	0.079
4	0.067	0.050	0.067	0.067	0.057	0.043	0.133	0.097
5	0.067	0.050	0.083	0.067	0.095	0.114	0.135	0.097
6	0.083	0.067	0.100	0.100	0.116	0.135	0.135	0.135
7	0.100	0.067	0.100	0.100	0.154	0.152	0.154	0.135

8	0.100	0.067	0.117	0.117	0.154	0.154	0.154	0.152
9	0.100	0.067	0.117	0.133	0.154	0.171	0.171	0.152
10	0.133	0.117	0.117	0.133	0.172	0.191	0.171	0.172
11	0.150	0.150	0.133	0.150	0.191	0.210	0.190	0.190
12	0.150	0.150	0.150	0.150	0.210	0.210	0.210	0.210
13	0.183	0.150	0.150	0.150	0.210	0.210	0.229	0.229
14	0.183	0.167	0.150	0.167	0.229	0.229	0.248	0.229
15	0.200	0.183	0.167	0.167	0.229	0.229	0.248	0.248
16	0.217	0.200	0.167	0.167	0.248	0.229	0.248	0.248
17	0.217	0.217	0.183	0.183	0.248	0.248	0.267	0.267
18	0.217	0.217	0.183	0.183	0.267	0.267	0.267	0.267
19	0.217	0.233	0.200	0.183	0.286	0.286	0.286	0.267
20	0.233	0.233	0.200	0.200	0.286	0.286	0.305	0.286
21	0.250	0.250	0.200	0.200	0.305	0.305	0.305	0.286
22	0.267	0.267	0.217	0.200	0.305	0.305	0.324	0.305
23	0.267	0.267	0.217	0.217	0.324	0.324	0.324	0.305
24	0.283	0.267	0.233	0.233	0.324	0.324	0.343	0.324
25	0.283	0.267	0.233	0.233	0.324	0.343	0.343	0.343
26	0.283	0.283	0.250	0.250	0.343	0.362	0.343	0.343
27	0.283	0.283	0.250	0.250	0.343	0.362	0.362	0.343
28	0.300	0.283	0.250	0.267	0.343	0.362	0.362	0.362
29	0.300	0.283	0.250	0.267	0.362	0.381	0.381	0.362
30	0.300	0.300	0.267	0.267	0.362	0.381	0.381	0.362
32	0.333	0.300	0.267	0.267	0.381	0.400	0.400	0.381
34	0.333	0.300	0.283	0.267	0.400	0.400	0.400	0.381
36	0.350	0.317	0.300	0.283	0.400	0.419	0.400	0.381
38	0.350	0.317	0.300	0.300	0.400	0.439	0.419	0.381
40	0.350	0.334	0.317	0.317	0.419	0.458	0.439	0.400
42	0.367	0.350	0.317	0.317	0.439	0.458	0.457	0.419
44	0.383	0.367	0.333	0.333	0.439	0.458	0.457	0.439
46	0.400	0.384	0.333	0.350	0.439	0.477	0.457	0.439
48	0.400	0.384	0.333	0.350	0.457	0.477	0.476	0.458
50	0.417	0.400	0.350	0.367	0.457	0.477	0.496	0.458
52	0.417	0.400	0.350	0.367	0.457	0.477	0.496	0.477
54	0.417	0.417	0.367	0.384	0.476	0.496	0.496	0.495
56	0.433	0.417	0.367	0.400	0.477	0.496	0.514	0.515
58	0.433	0.417	0.383	0.400	0.477	0.496	0.515	0.533
60	0.433	0.433	0.383	0.400	0.495	0.496	0.515	0.533
63	0.433	0.434	0.383	0.417	0.514	0.515	0.533	0.533
66	0.450	0.434	0.400	0.433	0.514	0.515	0.533	0.553
69	0.450	0.450	0.400	0.433	0.533	0.534	0.553	0.553

72	0.467	0.450	0.417	0.433	0.533	0.552	0.553	0.553
75	0.484	0.450	0.417	0.450	0.552	0.552	0.572	0.571
78	0.500	0.450	0.433	0.450	0.553	0.552	0.571	0.571
81	0.517	0.467	0.433	0.467	0.553	0.552	0.591	0.572
84	0.533	0.483	0.450	0.467	0.572	0.572	0.591	0.591
87	0.533	0.500	0.450	0.483	0.572	0.572	0.610	0.591
90	0.533	0.500	0.467	0.483	0.590	0.591	0.610	0.610
95	0.550	0.517	0.467	0.500	0.591	0.591	0.629	0.610
100	0.550	0.533	0.483	0.500	0.610	0.610	0.648	0.629
105	0.567	0.533	0.500	0.500	0.629	0.610	0.648	0.648
110	0.583	0.533	0.500	0.517	0.648	0.629	0.667	0.667
115	0.633	0.550	0.517	0.517	0.667	0.667	0.686	0.686
120	0.650	0.567	0.533	0.533	0.686	0.667	0.705	0.705
125	0.667	0.567	0.533	0.533	0.705	0.686	0.724	0.705
130	0.683	0.584	0.550	0.550	0.724	0.705	0.743	0.724
135	0.717	0.617	0.550	0.550	0.743	0.724	0.743	0.743
140	0.733	0.633	0.550	0.583	0.762	0.724	0.762	0.762
145	0.750	0.667	0.584	0.617	0.781	0.743	0.781	0.762
150	0.767	0.700	0.617	0.633	0.781	0.743	0.800	0.781
155	0.800	0.733	0.633	0.667	0.800	0.762	0.800	0.800
160	0.833	0.750	0.650	0.667	0.800	0.762	0.800	0.800
165	0.833	0.767	0.667	0.667	0.800	0.781	0.800	0.819
170	0.833	0.767	0.683	0.667	0.800	0.781	0.800	0.819
175	0.850	0.767	0.683	0.683	0.800	0.781	0.800	0.819
180	0.850	0.767	0.683	0.683	0.800	0.781	0.800	0.819

	Test3_200	Test3_200	Test3_200	Test3_200
	LEFT	LEFT	RIGHT	RIGHT
Time (s)	LV (mm)	LH (mm)	LV (mm)	LH (mm)
0	0.000	0.000	0.000	0.000
1	0.041	0.045	0.028	0.055
2	0.041	0.055	0.044	0.069
3	0.055	0.055	0.069	0.083
4	0.055	0.070	0.083	0.096
5	0.069	0.070	0.083	0.096
6	0.069	0.083	0.096	0.110
7	0.069	0.083	0.111	0.110
8	0.083	0.096	0.111	0.124
9	0.096	0.124	0.124	0.124
10	0.124	0.139	0.125	0.138
11	0.138	0.152	0.139	0.138

12	0.152	0.165	0.139	0.152
13	0.152	0.165	0.152	0.152
14	0.179	0.179	0.166	0.165
15	0.179	0.193	0.179	0.180
16	0.193	0.193	0.179	0.193
17	0.193	0.193	0.193	0.207
18	0.193	0.207	0.207	0.221
19	0.207	0.207	0.207	0.221
20	0.207	0.221	0.221	0.221
21	0.221	0.221	0.221	0.235
22	0.248	0.249	0.234	0.235
23	0.248	0.249	0.235	0.235
24	0.248	0.262	0.248	0.248
25	0.262	0.262	0.249	0.262
26	0.262	0.262	0.262	0.262
27	0.276	0.276	0.276	0.262
28	0.276	0.276	0.276	0.276
29	0.289	0.276	0.276	0.289
30	0.289	0.289	0.290	0.289
32	0.303	0.295	0.290	0.304
34	0.303	0.303	0.303	0.317
36	0.317	0.303	0.303	0.331
38	0.317	0.303	0.303	0.331
40	0.331	0.331	0.317	0.345
42	0.331	0.358	0.331	0.345
44	0.345	0.358	0.331	0.359
46	0.358	0.372	0.345	0.372
48	0.358	0.372	0.359	0.372
50	0.372	0.400	0.359	0.386
52	0.372	0.400	0.359	0.400
54	0.372	0.400	0.372	0.400
56	0.400	0.400	0.386	0.400
58	0.400	0.400	0.386	0.414
60	0.414	0.414	0.400	0.414
63	0.414	0.414	0.414	0.414
66	0.414	0.414	0.414	0.427
69	0.427	0.428	0.428	0.427
72	0.427	0.441	0.428	0.441
75	0.441	0.455	0.441	0.455
78	0.441	0.469	0.455	0.455
81	0.455	0.469	0.469	0.469

84	0.469	0.482	0.469	0.482
87	0.483	0.497	0.482	0.496
90	0.483	0.510	0.482	0.510
95	0.496	0.524	0.496	0.538
100	0.510	0.538	0.510	0.551
105	0.524	0.552	0.524	0.579
110	0.538	0.552	0.552	0.593
115	0.565	0.565	0.579	0.607
120	0.593	0.593	0.593	0.620
125	0.607	0.607	0.620	0.648
130	0.620	0.620	0.634	0.662
135	0.648	0.648	0.648	0.689
140	0.662	0.663	0.662	0.703
145	0.675	0.675	0.675	0.717
150	0.689	0.689	0.689	0.731
155	0.703	0.703	0.703	0.744
160	0.717	0.731	0.717	0.745
165	0.731	0.744	0.731	0.758
170	0.731	0.759	0.731	0.758
175	0.744	0.759	0.731	0.758
180	0.744	0.759	0.731	0.758

	Test1_ 500	Test1_ 500	Test1_ 500	Test1_ 500	Test2_ 500	Test2_ 500	Test2_ 500	Test2_ 500
	LEFT	LEFT	RIGHT	RIGHT	LEFT	LEFT	RIGHT	RIGHT
Time (s)	LV (mm)	LH (mm)	LV (mm)	LH (mm)	LV (mm)	LH (mm)	LV (mm)	LH (mm)
0	0	0	0	0	0	0	0	0
1	0.036	0.041	0.036	0.057	0.059	0.059	0.074	0.074
2	0.055	0.055	0.055	0.073	0.104	0.104	0.104	0.119
3	0.057	0.055	0.073	0.073	0.133	0.133	0.119	0.133
4	0.073	0.073	0.091	0.091	0.133	0.133	0.133	0.148
5	0.073	0.073	0.111	0.129	0.148	0.148	0.133	0.148
6	0.091	0.073	0.127	0.147	0.163	0.148	0.148	0.163
7	0.127	0.164	0.145	0.147	0.178	0.163	0.163	0.163
8	0.127	0.165	0.145	0.164	0.178	0.178	0.163	0.163
9	0.145	0.183	0.165	0.182	0.178	0.178	0.178	0.178
10	0.164	0.201	0.182	0.200	0.193	0.178	0.178	0.193
11	0.164	0.218	0.200	0.200	0.193	0.193	0.193	0.207
12	0.200	0.218	0.200	0.200	0.193	0.207	0.193	0.207
13	0.200	0.236	0.218	0.218	0.207	0.207	0.207	0.222

14	0.200	0.255	0.236	0.237	0.207	0.207	0.207	0.222
15	0.218	0.255	0.255	0.255	0.222	0.222	0.222	0.237
16	0.236	0.273	0.273	0.273	0.222	0.222	0.222	0.252
17	0.236	0.291	0.273	0.273	0.222	0.222	0.237	0.252
18	0.255	0.291	0.273	0.291	0.237	0.222	0.237	0.252
19	0.255	0.291	0.291	0.291	0.237	0.222	0.252	0.252
20	0.273	0.309	0.309	0.309	0.237	0.237	0.252	0.267
21	0.291	0.310	0.310	0.309	0.237	0.237	0.252	0.267
22	0.291	0.310	0.327	0.309	0.237	0.237	0.267	0.267
23	0.309	0.328	0.327	0.327	0.252	0.252	0.267	0.281
24	0.309	0.345	0.345	0.345	0.252	0.252	0.281	0.281
25	0.309	0.346	0.364	0.364	0.252	0.252	0.281	0.281
26	0.327	0.364	0.364	0.364	0.267	0.267	0.281	0.296
27	0.328	0.364	0.364	0.364	0.267	0.267	0.296	0.296
28	0.328	0.364	0.382	0.382	0.267	0.267	0.296	0.296
29	0.328	0.364	0.382	0.382	0.281	0.267	0.311	0.311
30	0.345	0.382	0.382	0.382	0.281	0.281	0.326	0.326
32	0.364	0.382	0.419	0.400	0.281	0.281	0.341	0.326
34	0.382	0.400	0.436	0.418	0.296	0.296	0.356	0.341
36	0.382	0.400	0.436	0.436	0.296	0.296	0.370	0.341
38	0.382	0.400	0.455	0.436	0.296	0.311	0.385	0.356
40	0.400	0.418	0.455	0.436	0.311	0.311	0.400	0.370
42	0.400	0.436	0.455	0.473	0.311	0.311	0.430	0.370
44	0.400	0.436	0.473	0.509	0.311	0.311	0.444	0.400
46	0.418	0.437	0.491	0.509	0.326	0.326	0.459	0.400
48	0.418	0.450	0.491	0.509	0.326	0.326	0.474	0.400
50	0.418	0.455	0.491	0.527	0.341	0.326	0.489	0.415
52	0.436	0.473	0.509	0.527	0.341	0.341	0.489	0.430
54	0.436	0.473	0.527	0.545	0.341	0.341	0.504	0.430
56	0.455	0.491	0.527	0.545	0.356	0.341	0.519	0.430
58	0.455	0.491	0.527	0.546	0.370	0.356	0.519	0.444
60	0.473	0.509	0.545	0.564	0.370	0.356	0.519	0.444
63	0.491	0.527	0.564	0.564	0.370	0.370	0.533	0.444
66	0.491	0.528	0.582	0.600	0.385	0.370	0.533	0.459
69	0.509	0.564	0.618	0.636	0.400	0.385	0.533	0.474
72	0.564	0.583	0.637	0.655	0.400	0.400	0.548	0.489
75	0.564	0.600	0.636	0.673	0.415	0.415	0.548	0.489
78	0.582	0.636	0.636	0.673	0.415	0.415	0.563	0.504
81	0.600	0.636	0.673	0.673	0.430	0.430	0.578	0.504
84	0.637	0.655	0.673	0.691	0.430	0.444	0.593	0.504
87	0.637	0.655	0.691	0.691	0.444	0.459	0.593	0.519

90	0.637	0.655	0.709	0.709	0.444	0.459	0.607	0.519
95	0.655	0.691	0.745	0.745	0.459	0.459	0.622	0.519
100	0.673	0.709	0.800	0.818	0.459	0.474	0.622	0.533
105	0.691	0.709	0.818	0.837	0.474	0.489	0.637	0.533
110	0.691	0.745	0.836	0.837	0.474	0.489	0.652	0.533
115	0.709	0.764	0.836	0.855	0.489	0.504	0.667	0.533
120	0.709	0.764	0.836	0.873	0.504	0.504	0.681	0.548
125	0.727	0.782	0.855	0.891	0.519	0.519	0.681	0.548
130	0.728	0.782	0.855	0.909	0.533	0.533	0.696	0.563
135	0.746	0.800	0.855	0.909	0.548	0.548	0.711	0.578
140	0.764	0.800	0.873	0.909	0.563	0.563	0.726	0.593
145	0.764	0.800	0.873	0.927	0.578	0.578	0.741	0.593
150	0.764	0.818	0.873	0.927	0.593	0.578	0.756	0.607
155	0.764	0.818	0.891	0.927	0.607	0.593	0.770	0.622
160	0.782	0.836	0.891	0.927	0.607	0.607	0.785	0.637
165	0.782	0.836	0.891	0.927	0.607	0.622	0.785	0.652
170	0.782	0.836	0.891	0.927	0.607	0.622	0.785	0.667
175	0.782	0.855	0.891	0.927	0.607	0.637	0.785	0.681
180	0.782	0.855	0.891	0.927	0.607	0.637	0.785	0.681

	Test3_500	Test3_500	Test3_500	Test3_500
	LEFT	LEFT	RIGHT	RIGHT
Time (s)	LV (mm)	LH (mm)	LV (mm)	LH (mm)
0	0	0	0	0
1	0.024	0.024	0.120	0.118
2	0.188	0.165	0.190	0.165
3	0.188	0.188	0.212	0.188
4	0.212	0.212	0.235	0.188
5	0.282	0.235	0.235	0.212
6	0.306	0.259	0.259	0.212
7	0.306	0.259	0.259	0.235
8	0.308	0.282	0.282	0.259
9	0.329	0.282	0.282	0.259
10	0.329	0.306	0.306	0.259
11	0.353	0.306	0.306	0.282
12	0.353	0.306	0.306	0.282
13	0.353	0.329	0.329	0.282
14	0.376	0.329	0.329	0.306
15	0.376	0.329	0.329	0.306
16	0.376	0.329	0.353	0.329
17	0.376	0.329	0.353	0.329

18	0.376	0.353	0.353	0.329
19	0.376	0.353	0.376	0.353
20	0.400	0.353	0.376	0.353
21	0.400	0.353	0.376	0.353
22	0.400	0.353	0.400	0.376
23	0.400	0.376	0.400	0.376
24	0.400	0.376	0.400	0.376
25	0.424	0.376	0.400	0.376
26	0.424	0.376	0.400	0.376
27	0.424	0.376	0.400	0.400
28	0.447	0.400	0.424	0.400
29	0.447	0.400	0.424	0.424
30	0.447	0.400	0.424	0.424
32	0.447	0.424	0.424	0.424
34	0.471	0.424	0.447	0.447
36	0.471	0.447	0.447	0.447
38	0.471	0.447	0.471	0.471
40	0.471	0.471	0.471	0.471
42	0.495	0.494	0.471	0.495
44	0.518	0.518	0.494	0.495
46	0.518	0.518	0.494	0.495
48	0.541	0.518	0.494	0.495
50	0.541	0.518	0.494	0.518
52	0.565	0.541	0.518	0.518
54	0.565	0.541	0.518	0.518
56	0.565	0.541	0.541	0.541
58	0.588	0.541	0.541	0.565
60	0.588	0.541	0.541	0.588
63	0.612	0.541	0.565	0.588
66	0.612	0.541	0.588	0.588
69	0.612	0.541	0.588	0.588
72	0.635	0.541	0.588	0.612
75	0.635	0.565	0.588	0.612
78	0.635	0.565	0.612	0.635
81	0.659	0.565	0.612	0.659
84	0.659	0.565	0.612	0.659
87	0.659	0.565	0.612	0.659
90	0.659	0.565	0.635	0.682
95	0.682	0.588	0.659	0.706
100	0.682	0.612	0.659	0.706
105	0.706	0.612	0.682	0.729

110	0.706	0.635	0.682	0.753
115	0.706	0.659	0.706	0.753
120	0.729	0.686	0.706	0.776
125	0.729	0.706	0.706	0.777
130	0.753	0.729	0.706	0.800
135	0.777	0.753	0.706	0.800
140	0.800	0.776	0.730	0.824
145	0.824	0.800	0.730	0.824
150	0.847	0.824	0.730	0.824
155	0.871	0.847	0.730	0.824
160	0.894	0.871	0.730	0.824
165	0.894	0.871	0.730	0.824
170	0.894	0.871	0.730	0.847
175	0.894	0.871	0.730	0.847
180	0.894	0.871	0.730	0.847

Normalized data**:**

	Test1_ 70	Test1_ 70	Test1_ 70	Test1_ 70	Test2_ 70	Test2_ 70	Test2_ 70	Test2_ 70
	LEFT	LEFT	RIGHT	RIGHT	LEFT	LEFT	RIGHT	RIGHT
Time (s)	LV/LVM	LH/LHM	LV/LVM	LH/LHM	LV/LVM	LH/LHM	LV/LVM	LH/LHM
0	0	0	0	0	0	0	0	0
1	0.070	0.051	0.073	0.088	0.050	0.000	0.050	0.051
2	0.088	0.118	0.145	0.123	0.100	0.050	0.050	0.077
3	0.193	0.186	0.182	0.140	0.100	0.050	0.125	0.103
4	0.210	0.203	0.200	0.193	0.100	0.050	0.125	0.103
5	0.228	0.271	0.218	0.193	0.100	0.125	0.175	0.154
6	0.263	0.271	0.236	0.228	0.013	0.125	0.175	0.154
7	0.281	0.288	0.255	0.262	0.150	0.175	0.175	0.179
8	0.281	0.305	0.327	0.333	0.175	0.200	0.200	0.179
9	0.298	0.322	0.327	0.368	0.175	0.200	0.225	0.205
10	0.351	0.322	0.327	0.368	0.200	0.250	0.225	0.256
11	0.351	0.339	0.364	0.368	0.200	0.250	0.250	0.256
12	0.351	0.355	0.382	0.386	0.225	0.250	0.275	0.256
13	0.403	0.389	0.382	0.403	0.275	0.275	0.275	0.282
14	0.403	0.389	0.400	0.403	0.300	0.300	0.300	0.308
15	0.421	0.389	0.400	0.421	0.325	0.350	0.325	0.308
16	0.439	0.390	0.436	0.438	0.325	0.350	0.325	0.333
17	0.439	0.440	0.436	0.456	0.350	0.350	0.325	0.333

18	0.456	0.457	0.455	0.473	0.350	0.350	0.350	0.333
19	0.456	0.491	0.455	0.508	0.375	0.375	0.375	0.359
20	0.474	0.508	0.455	0.526	0.375	0.375	0.375	0.359
21	0.474	0.508	0.473	0.544	0.400	0.375	0.375	0.410
22	0.491	0.542	0.473	0.561	0.425	0.400	0.400	0.410
23	0.509	0.525	0.491	0.561	0.450	0.425	0.425	0.462
24	0.509	0.525	0.509	0.579	0.450	0.475	0.425	0.487
25	0.526	0.542	0.509	0.579	0.475	0.475	0.450	0.487
26	0.544	0.559	0.527	0.579	0.475	0.475	0.450	0.487
27	0.544	0.559	0.545	0.596	0.475	0.475	0.450	0.513
28	0.544	0.576	0.545	0.596	0.475	0.501	0.475	0.513
29	0.561	0.576	0.564	0.596	0.500	0.501	0.475	0.513
30	0.579	0.576	0.582	0.631	0.525	0.525	0.500	0.513
32	0.579	0.610	0.582	0.631	0.525	0.525	0.525	0.538
34	0.614	0.610	0.600	0.631	0.525	0.550	0.525	0.564
36	0.649	0.610	0.636	0.649	0.550	0.550	0.525	0.615
38	0.649	0.644	0.655	0.684	0.575	0.600	0.550	0.615
40	0.667	0.660	0.655	0.684	0.600	0.600	0.550	0.615
42	0.667	0.678	0.709	0.702	0.600	0.600	0.575	0.641
44	0.667	0.694	0.709	0.701	0.625	0.625	0.575	0.641
46	0.684	0.694	0.727	0.702	0.625	0.625	0.625	0.667
48	0.719	0.711	0.745	0.719	0.625	0.625	0.625	0.692
50	0.719	0.728	0.764	0.737	0.650	0.650	0.650	0.692
52	0.737	0.745	0.782	0.771	0.650	0.650	0.650	0.718
54	0.754	0.762	0.782	0.772	0.675	0.700	0.675	0.718
56	0.807	0.796	0.818	0.789	0.675	0.675	0.725	0.718
58	0.824	0.813	0.836	0.807	0.675	0.700	0.725	0.770
60	0.842	0.830	0.836	0.824	0.700	0.750	0.750	0.769
63	0.860	0.847	0.873	0.859	0.750	0.800	0.775	0.821
66	0.877	0.863	0.873	0.894	0.775	0.850	0.775	0.872
69	0.895	0.865	0.873	0.912	0.800	0.850	0.800	0.898
72	0.895	0.881	0.891	0.929	0.825	0.875	0.850	0.949
75	0.930	0.898	0.927	0.947	0.850	0.900	0.850	0.949
78	0.947	0.915	0.945	0.964	0.900	0.925	0.875	0.974
81	0.965	0.932	0.945	0.964	0.925	0.925	0.900	0.975
84	0.965	0.949	0.964	0.982	0.950	0.950	0.925	1.000
87	0.965	0.965	0.964	0.982	0.975	0.975	0.950	1.000
90	0.965	0.966	0.982	1.000	0.975	0.975	0.950	1.000
95	1.000	0.966	0.982	1.000	0.975	0.975	0.975	1.000
100	1.000	0.983	0.982	0.999	0.975	0.975	1.000	1.000
105	1.000	0.983	1.000	1.000	0.975	0.975	1.000	1.000

110	1.000	1.000	1.000	1.000	0.975	0.975	1.000	1.000
115	1.000	0.999	1.000	1.000	0.975	1.000	1.000	1.000
120	1.000	1.000	1.000	1.000	1.000	1.000	1.000	1.000

	Test3_ 70	Test3_ 70	Test3_ 70	Test3_ 70	Test4_ 70	Test4_ 70	Test4_ 70	Test4_ 70
	LEFT	LEFT	RIGHT	RIGHT	LEFT	LEFT	RIGHT	RIGHT
Time (s)	LV/LVM	LH/LHM	LV/LVM	LH/LHM	LV/LVM	LH/LHM	LV/LVM	LH/LHM
0	0	0	0	0	0	0	0	0
1	0.087	0.068	0.111	0.111	0.035	0.036	0.017	0.034
2	0.087	0.068	0.133	0.111	0.070	0.036	0.052	0.052
3	0.109	0.091	0.133	0.111	0.088	0.054	0.052	0.052
4	0.130	0.091	0.133	0.156	0.088	0.071	0.069	0.052
5	0.130	0.091	0.156	0.178	0.088	0.071	0.069	0.069
6	0.152	0.114	0.156	0.156	0.105	0.071	0.069	0.069
7	0.152	0.136	0.156	0.156	0.105	0.071	0.086	0.088
8	0.174	0.182	0.178	0.178	0.123	0.089	0.086	0.103
9	0.196	0.205	0.178	0.200	0.123	0.089	0.103	0.103
10	0.217	0.250	0.178	0.200	0.123	0.089	0.105	0.103
11	0.261	0.250	0.200	0.200	0.140	0.107	0.105	0.121
12	0.261	0.250	0.200	0.200	0.140	0.107	0.122	0.121
13	0.304	0.295	0.244	0.244	0.140	0.143	0.155	0.155
14	0.326	0.318	0.289	0.289	0.159	0.161	0.155	0.155
15	0.369	0.341	0.311	0.333	0.175	0.179	0.173	0.172
16	0.369	0.364	0.356	0.333	0.175	0.179	0.173	0.190
17	0.391	0.364	0.356	0.333	0.211	0.196	0.190	0.207
18	0.413	0.409	0.356	0.378	0.211	0.232	0.190	0.224
19	0.413	0.432	0.378	0.378	0.246	0.250	0.225	0.241
20	0.435	0.432	0.400	0.400	0.246	0.250	0.225	0.259
21	0.435	0.432	0.422	0.422	0.263	0.268	0.242	0.276
22	0.456	0.477	0.444	0.422	0.263	0.304	0.259	0.293
23	0.478	0.477	0.444	0.444	0.298	0.304	0.294	0.310
24	0.500	0.477	0.467	0.467	0.316	0.304	0.311	0.310
25	0.522	0.501	0.467	0.467	0.316	0.339	0.328	0.328
26	0.522	0.523	0.489	0.489	0.333	0.340	0.328	0.328
27	0.543	0.523	0.489	0.489	0.368	0.358	0.362	0.362
28	0.565	0.545	0.511	0.533	0.386	0.411	0.362	0.379
29	0.565	0.568	0.511	0.556	0.386	0.429	0.397	0.414

30	0.565	0.568	0.533	0.578	0.404	0.429	0.397	0.414
32	0.609	0.614	0.578	0.578	0.404	0.446	0.414	0.431
34	0.609	0.614	0.578	0.578	0.439	0.482	0.448	0.449
36	0.609	0.614	0.600	0.600	0.474	0.482	0.448	0.448
38	0.630	0.614	0.600	0.600	0.492	0.500	0.483	0.466
40	0.652	0.637	0.622	0.644	0.509	0.518	0.517	0.517
42	0.674	0.659	0.644	0.667	0.544	0.536	0.552	0.534
44	0.674	0.659	0.644	0.667	0.561	0.571	0.569	0.535
46	0.695	0.659	0.667	0.667	0.596	0.571	0.569	0.569
48	0.695	0.682	0.667	0.667	0.597	0.589	0.603	0.586
50	0.717	0.705	0.689	0.689	0.649	0.607	0.621	0.603
52	0.717	0.705	0.689	0.689	0.649	0.625	0.638	0.638
54	0.761	0.705	0.689	0.711	0.684	0.643	0.672	0.672
56	0.761	0.727	0.733	0.733	0.719	0.679	0.707	0.707
58	0.782	0.727	0.733	0.733	0.754	0.732	0.724	0.707
60	0.783	0.750	0.756	0.756	0.754	0.750	0.741	0.724
63	0.783	0.773	0.778	0.756	0.772	0.750	0.776	0.759
66	0.804	0.795	0.800	0.778	0.789	0.768	0.828	0.759
69	0.826	0.818	0.822	0.800	0.825	0.804	0.845	0.776
72	0.848	0.841	0.822	0.822	0.842	0.839	0.845	0.793
75	0.848	0.886	0.844	0.822	0.877	0.893	0.862	0.810
78	0.870	0.909	0.844	0.845	0.895	0.893	0.879	0.862
81	0.913	0.909	0.889	0.889	0.912	0.911	0.931	0.879
84	0.956	0.909	0.911	0.911	0.947	0.929	0.948	0.914
87	1.000	0.932	0.956	0.933	0.965	0.964	0.948	0.931
90	1.000	0.978	0.978	0.956	0.965	0.964	0.983	0.948
95	1.000	0.978	0.978	0.978	0.983	0.982	0.983	0.948
100	1.000	1.000	1.000	1.000	1.000	1.000	1.000	0.983
105	1.000	1.000	1.000	1.000	1.000	1.000	1.000	0.983
110	1.000	1.000	1.000	1.000	1.000	1.000	1.000	0.983
115	1.000	1.000	1.000	1.000	1.000	1.000	1.000	1.000
120	1.000	1.000	1.000	1.000	1.000	1.000	1.000	1.000

	Test5_70	Test5_70	Test5_70	Test5_70	Test6_70	Test6_70	Test6_70	Test6_70
	LEFT	LEFT	RIGHT	RIGHT	LEFT	LEFT	RIGHT	RIGHT
Time (s)	LV/LVM	LH /LHM	LV/LVM	LH/LHM	LV/LVM	LH/LHM	LV/LVM	LH/LHM
0	0	0	0	0	0	0	0	0
1	0.019	0.058	0.037	0.019	0.023	0.023	0.000	0.000
2	0.057	0.058	0.056	0.038	0.046	0.023	0.023	0.023

3	0.075	0.058	0.056	0.038	0.074	0.052	0.023	0.023
4	0.094	0.077	0.093	0.077	0.074	0.074	0.023	0.023
5	0.113	0.096	0.130	0.096	0.093	0.093	0.047	0.047
6	0.132	0.115	0.130	0.096	0.096	0.093	0.070	0.070
7	0.151	0.154	0.148	0.115	0.116	0.093	0.096	0.093
8	0.151	0.154	0.148	0.154	0.141	0.141	0.141	0.140
9	0.189	0.173	0.167	0.173	0.163	0.163	0.163	0.163
10	0.226	0.211	0.185	0.192	0.163	0.164	0.186	0.163
11	0.226	0.231	0.222	0.231	0.163	0.187	0.211	0.209
12	0.264	0.250	0.259	0.250	0.187	0.209	0.233	0.234
13	0.302	0.288	0.278	0.288	0.211	0.234	0.279	0.280
14	0.340	0.308	0.315	0.308	0.232	0.257	0.279	0.280
15	0.358	0.327	0.352	0.346	0.256	0.257	0.303	0.303
16	0.377	0.346	0.370	0.365	0.279	0.280	0.326	0.326
17	0.377	0.385	0.407	0.404	0.303	0.303	0.350	0.350
18	0.396	0.404	0.426	0.423	0.303	0.326	0.372	0.373
19	0.415	0.443	0.463	0.461	0.325	0.325	0.395	0.396
20	0.434	0.461	0.463	0.461	0.349	0.372	0.395	0.396
21	0.472	0.481	0.481	0.461	0.349	0.372	0.419	0.419
22	0.490	0.519	0.519	0.481	0.350	0.395	0.419	0.419
23	0.490	0.519	0.519	0.500	0.395	0.418	0.442	0.442
24	0.509	0.538	0.537	0.538	0.418	0.442	0.442	0.465
25	0.528	0.558	0.556	0.558	0.442	0.465	0.465	0.465
26	0.566	0.596	0.593	0.558	0.465	0.489	0.465	0.512
27	0.585	0.596	0.593	0.577	0.466	0.512	0.488	0.512
28	0.623	0.596	0.593	0.615	0.488	0.512	0.512	0.512
29	0.641	0.615	0.630	0.615	0.488	0.512	0.512	0.535
30	0.641	0.634	0.648	0.634	0.511	0.535	0.512	0.535
32	0.660	0.634	0.685	0.673	0.511	0.535	0.535	0.535
34	0.698	0.673	0.685	0.673	0.511	0.535	0.535	0.558
36	0.736	0.692	0.722	0.692	0.535	0.535	0.535	0.558
38	0.736	0.712	0.722	0.731	0.558	0.558	0.559	0.582
40	0.755	0.750	0.759	0.750	0.558	0.560	0.559	0.605
42	0.773	0.788	0.759	0.788	0.558	0.581	0.581	0.605
44	0.773	0.788	0.796	0.808	0.581	0.605	0.605	0.651
46	0.811	0.808	0.796	0.827	0.581	0.628	0.605	0.651
48	0.830	0.827	0.815	0.827	0.605	0.628	0.628	0.698
50	0.830	0.827	0.834	0.846	0.628	0.651	0.651	0.698
52	0.849	0.846	0.870	0.885	0.674	0.674	0.652	0.698
54	0.868	0.865	0.871	0.904	0.674	0.698	0.675	0.698
56	0.905	0.904	0.889	0.904	0.697	0.722	0.698	0.721

58	0.943	0.923	0.907	0.904	0.721	0.744	0.745	0.768
60	0.943	0.942	0.908	0.923	0.721	0.744	0.767	0.791
63	0.962	0.961	0.908	0.923	0.768	0.790	0.767	0.837
66	0.962	0.962	0.926	0.942	0.790	0.814	0.814	0.838
69	0.962	0.962	0.926	0.942	0.837	0.837	0.838	0.860
72	0.962	0.962	0.945	0.942	0.837	0.837	0.837	0.884
75	0.962	0.981	0.945	0.961	0.860	0.860	0.884	0.884
78	0.962	0.981	0.945	0.961	0.861	0.860	0.884	0.930
81	0.981	0.981	0.963	0.981	0.861	0.884	0.907	0.931
84	0.981	0.981	0.963	0.981	0.884	0.884	0.930	0.953
87	0.981	0.981	0.981	0.981	0.907	0.930	0.953	0.953
90	0.981	1.000	0.982	1.000	0.930	0.954	0.953	0.953
95	1.000	1.000	0.982	1.000	0.953	0.976	0.953	0.953
100	1.000	1.000	0.982	1.000	0.954	0.976	0.953	1.000
105	1.000	1.000	1.000	1.000	0.976	0.976	0.977	1.000
110	1.000	1.000	1.000	1.000	0.976	1.000	1.000	1.000
115	1.000	1.000	1.000	1.000	1.000	1.000	1.000	1.000
120	1.000	1.000	1.000	1.000	1.000	1.000	1.000	1.000

	0.660	0.680	0.700	0.700
	Test7_70	Test7_70	Test7_70	Test7_70
	LEFT	LEFT	RIGHT	RIGHT
Time (s)	LV/LVM	LH/LHM	LV/LVM	LH/LHM
0	0	0	0	0
1	0.091	0.088	0.029	0.057
2	0.121	0.118	0.057	0.114
3	0.121	0.118	0.114	0.114
4	0.121	0.147	0.114	0.143
5	0.152	0.147	0.114	0.143
6	0.152	0.206	0.114	0.114
7	0.152	0.206	0.143	0.143
8	0.182	0.206	0.171	0.143
9	0.182	0.206	0.229	0.171
10	0.212	0.235	0.257	0.200
11	0.242	0.235	0.286	0.257
12	0.242	0.265	0.286	0.286
13	0.273	0.265	0.314	0.314
14	0.273	0.294	0.314	0.314
15	0.303	0.323	0.343	0.343
16	0.364	0.323	0.343	0.343
17	0.364	0.353	0.343	0.371

18	0.364	0.353	0.371	0.400
19	0.364	0.382	0.371	0.400
20	0.364	0.412	0.371	0.429
21	0.394	0.412	0.400	0.429
22	0.394	0.413	0.429	0.457
23	0.394	0.441	0.457	0.457
24	0.424	0.441	0.486	0.486
25	0.424	0.441	0.486	0.486
26	0.455	0.471	0.514	0.486
27	0.455	0.471	0.514	0.514
28	0.455	0.501	0.514	0.514
29	0.485	0.501	0.543	0.514
30	0.485	0.529	0.543	0.543
32	0.515	0.530	0.543	0.543
34	0.545	0.559	0.571	0.543
36	0.576	0.588	0.571	0.571
38	0.606	0.588	0.571	0.600
40	0.636	0.589	0.600	0.600
42	0.636	0.617	0.600	0.600
44	0.667	0.647	0.629	0.629
46	0.667	0.676	0.629	0.629
48	0.667	0.676	0.657	0.657
50	0.697	0.676	0.657	0.657
52	0.697	0.676	0.686	0.657
54	0.697	0.706	0.686	0.686
56	0.727	0.706	0.714	0.686
58	0.727	0.706	0.714	0.714
60	0.727	0.736	0.743	0.714
63	0.758	0.736	0.743	0.743
66	0.758	0.736	0.771	0.771
69	0.788	0.765	0.771	0.771
72	0.788	0.765	0.771	0.800
75	0.818	0.794	0.800	0.800
78	0.818	0.794	0.800	0.800
81	0.818	0.823	0.800	0.800
84	0.848	0.853	0.829	0.829
87	0.848	0.853	0.829	0.829
90	0.879	0.853	0.829	0.829
95	0.909	0.882	0.857	0.857
100	0.909	0.882	0.886	0.886
105	0.939	0.941	0.914	0.914

110	0.970	0.970	0.943	0.943
115	1.000	1.000	0.971	0.971
120	1.000	1.000	1.000	1.000

	Test1_ 200	Test1_ 200	Test1_ 200	Test1_ 200	Test2_ 200	Test2_ 200	Test2_ 200	Test2_ 200
	LEFT	LEFT	RIGHT	RIGHT	LEFT	LEFT	RIGHT	RIGHT
Time (s)	LV/LVM	LH/LHM	LV/LVM	LH/LHM	LV/LVM	LH/LHM	LV/LVM	LH/LHM
0	0.000	0.000	0.000	0.000	0.000	0.000	0.000	0.000
1	0.020	0.022	0.049	0.024	0.024	0.024	0.048	0.052
2	0.039	0.043	0.073	0.049	0.024	0.024	0.095	0.074
3	0.059	0.065	0.098	0.098	0.048	0.034	0.143	0.096
4	0.078	0.065	0.098	0.098	0.071	0.055	0.167	0.119
5	0.078	0.065	0.122	0.098	0.119	0.146	0.168	0.119
6	0.098	0.087	0.146	0.146	0.145	0.172	0.168	0.164
7	0.118	0.087	0.146	0.146	0.192	0.195	0.192	0.164
8	0.118	0.087	0.171	0.171	0.192	0.197	0.192	0.186
9	0.118	0.087	0.171	0.195	0.192	0.219	0.214	0.186
10	0.157	0.152	0.171	0.195	0.216	0.245	0.214	0.211
11	0.176	0.196	0.195	0.220	0.239	0.268	0.238	0.232
12	0.176	0.196	0.220	0.220	0.262	0.269	0.263	0.257
13	0.216	0.196	0.220	0.220	0.262	0.269	0.287	0.280
14	0.216	0.217	0.220	0.244	0.287	0.294	0.309	0.280
15	0.235	0.239	0.244	0.244	0.287	0.294	0.309	0.303
16	0.255	0.261	0.244	0.244	0.310	0.294	0.309	0.303
17	0.255	0.283	0.268	0.268	0.310	0.318	0.333	0.326
18	0.255	0.283	0.268	0.268	0.333	0.342	0.333	0.326
19	0.255	0.304	0.293	0.268	0.357	0.366	0.358	0.326
20	0.275	0.304	0.293	0.293	0.358	0.367	0.381	0.350
21	0.294	0.326	0.293	0.293	0.382	0.391	0.382	0.350
22	0.314	0.348	0.317	0.293	0.382	0.391	0.405	0.373
23	0.314	0.348	0.317	0.317	0.405	0.415	0.405	0.373
24	0.333	0.348	0.341	0.341	0.405	0.415	0.428	0.396
25	0.333	0.348	0.341	0.341	0.405	0.440	0.428	0.419
26	0.333	0.370	0.366	0.366	0.429	0.464	0.428	0.419
27	0.333	0.370	0.366	0.366	0.429	0.464	0.453	0.419
28	0.353	0.370	0.366	0.390	0.429	0.464	0.453	0.442
29	0.353	0.370	0.366	0.390	0.453	0.488	0.477	0.442
30	0.353	0.392	0.390	0.390	0.453	0.488	0.477	0.442
32	0.392	0.392	0.390	0.390	0.477	0.513	0.500	0.465

34	0.392	0.392	0.415	0.390	0.500	0.513	0.500	0.465
36	0.412	0.413	0.439	0.415	0.501	0.537	0.500	0.466
38	0.412	0.413	0.439	0.439	0.501	0.561	0.524	0.466
40	0.412	0.435	0.463	0.463	0.524	0.586	0.548	0.489
42	0.431	0.457	0.463	0.463	0.548	0.586	0.571	0.512
44	0.451	0.479	0.488	0.488	0.548	0.586	0.571	0.535
46	0.471	0.500	0.488	0.512	0.548	0.610	0.571	0.535
48	0.471	0.500	0.488	0.512	0.571	0.610	0.595	0.558
50	0.490	0.522	0.512	0.537	0.571	0.610	0.619	0.558
52	0.490	0.522	0.512	0.537	0.571	0.610	0.619	0.582
54	0.490	0.543	0.537	0.562	0.595	0.634	0.619	0.604
56	0.510	0.543	0.537	0.585	0.596	0.634	0.643	0.628
58	0.510	0.544	0.561	0.585	0.596	0.634	0.643	0.651
60	0.510	0.565	0.561	0.585	0.619	0.634	0.643	0.651
63	0.510	0.566	0.561	0.610	0.643	0.659	0.666	0.651
66	0.529	0.566	0.585	0.634	0.643	0.659	0.666	0.675
69	0.529	0.587	0.585	0.634	0.667	0.683	0.691	0.675
72	0.549	0.587	0.610	0.634	0.667	0.707	0.691	0.675
75	0.569	0.587	0.610	0.659	0.690	0.707	0.714	0.697
78	0.588	0.587	0.634	0.659	0.691	0.707	0.714	0.697
81	0.608	0.609	0.634	0.683	0.691	0.707	0.738	0.698
84	0.627	0.630	0.659	0.683	0.715	0.732	0.738	0.721
87	0.627	0.653	0.659	0.707	0.715	0.732	0.762	0.721
90	0.627	0.653	0.683	0.707	0.738	0.756	0.762	0.744
95	0.647	0.674	0.683	0.732	0.738	0.756	0.785	0.744
100	0.647	0.696	0.707	0.732	0.762	0.781	0.810	0.768
105	0.667	0.696	0.732	0.732	0.786	0.781	0.810	0.791
110	0.686	0.696	0.732	0.756	0.810	0.805	0.833	0.814
115	0.745	0.718	0.756	0.756	0.833	0.853	0.857	0.837
120	0.765	0.739	0.780	0.780	0.857	0.854	0.881	0.861
125	0.784	0.739	0.780	0.780	0.881	0.878	0.905	0.861
130	0.804	0.761	0.805	0.805	0.905	0.903	0.928	0.884
135	0.843	0.804	0.805	0.805	0.929	0.927	0.928	0.907
140	0.863	0.826	0.805	0.854	0.952	0.927	0.952	0.930
145	0.882	0.870	0.854	0.902	0.976	0.951	0.976	0.930
150	0.902	0.913	0.902	0.927	0.976	0.951	1.000	0.953
155	0.941	0.957	0.927	0.976	1.000	0.975	1.000	0.976
160	0.980	0.979	0.951	0.976	1.000	0.976	1.000	0.976
165	0.980	1.000	0.976	0.976	1.000	1.000	1.000	1.000
170	0.980	1.000	1.000	0.976	1.000	1.000	1.000	1.000
175	1.000	1.000	1.000	1.000	1.000	1.000	1.000	1.000

180	1.000	1.000	1.000	1.000	1.000	1.000	1.000	1.000

	Test3_200	Test3_200	Test3_200	Test3_200
	LEFT	LEFT	RIGHT	RIGHT
Time (s)	LV/LVM	LH/LHM	LV/LVM	LH/LHM
0	0.000	0.000	0.000	0.000
1	0.056	0.060	0.038	0.073
2	0.056	0.073	0.060	0.091
3	0.074	0.073	0.094	0.109
4	0.074	0.093	0.113	0.127
5	0.093	0.093	0.113	0.127
6	0.093	0.109	0.132	0.145
7	0.093	0.109	0.152	0.145
8	0.111	0.127	0.152	0.164
9	0.130	0.164	0.170	0.164
10	0.167	0.183	0.171	0.182
11	0.185	0.201	0.190	0.182
12	0.204	0.218	0.190	0.201
13	0.204	0.218	0.208	0.201
14	0.241	0.236	0.227	0.218
15	0.241	0.254	0.245	0.237
16	0.259	0.254	0.245	0.255
17	0.259	0.255	0.264	0.273
18	0.259	0.273	0.284	0.291
19	0.278	0.273	0.284	0.291
20	0.278	0.291	0.302	0.291
21	0.296	0.291	0.302	0.310
22	0.333	0.328	0.321	0.310
23	0.333	0.328	0.321	0.310
24	0.333	0.345	0.340	0.327
25	0.352	0.345	0.340	0.346
26	0.352	0.345	0.358	0.345
27	0.370	0.363	0.377	0.345
28	0.370	0.363	0.378	0.364
29	0.389	0.363	0.378	0.382
30	0.389	0.382	0.397	0.382
32	0.407	0.389	0.397	0.400
34	0.407	0.400	0.415	0.418
36	0.426	0.400	0.415	0.436
38	0.426	0.400	0.415	0.436
40	0.445	0.436	0.434	0.455

42	0.445	0.472	0.453	0.455
44	0.463	0.472	0.453	0.473
46	0.481	0.491	0.472	0.491
48	0.481	0.491	0.491	0.491
50	0.500	0.527	0.491	0.509
52	0.500	0.527	0.491	0.527
54	0.500	0.527	0.510	0.527
56	0.537	0.527	0.529	0.527
58	0.537	0.527	0.529	0.546
60	0.556	0.545	0.547	0.546
63	0.556	0.545	0.566	0.546
66	0.556	0.546	0.566	0.564
69	0.574	0.564	0.585	0.564
72	0.574	0.581	0.585	0.582
75	0.593	0.600	0.604	0.600
78	0.593	0.618	0.623	0.600
81	0.611	0.618	0.642	0.618
84	0.630	0.636	0.642	0.636
87	0.648	0.655	0.660	0.654
90	0.648	0.673	0.660	0.673
95	0.667	0.690	0.680	0.709
100	0.685	0.709	0.698	0.727
105	0.704	0.728	0.717	0.764
110	0.722	0.728	0.755	0.782
115	0.759	0.745	0.792	0.800
120	0.796	0.782	0.811	0.818
125	0.815	0.800	0.849	0.855
130	0.833	0.818	0.868	0.873
135	0.871	0.854	0.887	0.909
140	0.889	0.873	0.906	0.927
145	0.907	0.890	0.925	0.945
150	0.926	0.909	0.943	0.964
155	0.944	0.927	0.962	0.982
160	0.963	0.963	0.981	0.982
165	0.981	0.981	1.000	1.000
170	0.982	1.000	1.000	1.000
175	1.000	1.000	1.000	1.000
180	1.000	1.000	1.000	1.000

	Test1_ 500	Test1_ 500	Test1_ 500	Test1_ 500	Test2_ 500	Test2_ 500	Test2_ 500	Test2_ 500

	LEFT	LEFT	RIGHT	RIGHT	LEFT	LEFT	RIGHT	RIGHT
Time (s)	LV/LVM	LH/LHM	LV/LVM	LH/LHM	LV/LVM	LH/LHM	LV/LVM	LH/LHM
0	0.000	0.000	0.000	0.000	0.000	0.000	0.000	0.000
1	0.047	0.048	0.041	0.062	0.098	0.093	0.094	0.109
2	0.070	0.064	0.061	0.078	0.171	0.163	0.132	0.174
3	0.074	0.064	0.082	0.078	0.220	0.209	0.151	0.196
4	0.093	0.085	0.102	0.098	0.220	0.209	0.170	0.217
5	0.093	0.085	0.124	0.139	0.244	0.233	0.170	0.217
6	0.116	0.085	0.143	0.158	0.268	0.233	0.189	0.239
7	0.163	0.191	0.163	0.158	0.293	0.256	0.208	0.239
8	0.163	0.193	0.163	0.176	0.293	0.279	0.208	0.239
9	0.186	0.214	0.185	0.196	0.293	0.279	0.226	0.261
10	0.209	0.235	0.204	0.216	0.317	0.279	0.226	0.283
11	0.209	0.255	0.224	0.216	0.317	0.302	0.245	0.304
12	0.256	0.255	0.224	0.216	0.317	0.326	0.245	0.304
13	0.256	0.277	0.245	0.235	0.341	0.326	0.264	0.326
14	0.256	0.299	0.265	0.256	0.341	0.326	0.264	0.326
15	0.279	0.299	0.286	0.275	0.366	0.349	0.283	0.348
16	0.302	0.319	0.307	0.294	0.366	0.349	0.283	0.370
17	0.302	0.341	0.307	0.295	0.366	0.349	0.302	0.370
18	0.326	0.341	0.307	0.314	0.390	0.349	0.302	0.370
19	0.326	0.341	0.327	0.314	0.390	0.349	0.321	0.370
20	0.349	0.362	0.347	0.333	0.390	0.372	0.321	0.391
21	0.372	0.362	0.348	0.333	0.390	0.372	0.321	0.391
22	0.372	0.362	0.367	0.333	0.390	0.372	0.340	0.391
23	0.395	0.384	0.367	0.353	0.415	0.395	0.340	0.413
24	0.395	0.404	0.388	0.373	0.415	0.395	0.358	0.413
25	0.395	0.405	0.408	0.392	0.415	0.395	0.358	0.413
26	0.419	0.426	0.408	0.392	0.439	0.419	0.358	0.435
27	0.419	0.426	0.408	0.393	0.439	0.419	0.377	0.435
28	0.419	0.426	0.429	0.412	0.439	0.419	0.377	0.435
29	0.419	0.426	0.429	0.412	0.463	0.419	0.396	0.457
30	0.442	0.447	0.429	0.412	0.463	0.442	0.415	0.478
32	0.465	0.447	0.470	0.431	0.463	0.442	0.434	0.478
34	0.489	0.468	0.490	0.451	0.488	0.465	0.453	0.500
36	0.489	0.469	0.490	0.471	0.488	0.465	0.472	0.500
38	0.489	0.469	0.510	0.471	0.488	0.488	0.491	0.522
40	0.512	0.489	0.510	0.471	0.512	0.488	0.509	0.543
42	0.512	0.511	0.511	0.510	0.512	0.488	0.547	0.543
44	0.512	0.511	0.531	0.549	0.512	0.488	0.566	0.587
46	0.535	0.511	0.551	0.549	0.537	0.512	0.585	0.587

48	0.535	0.527	0.551	0.549	0.537	0.512	0.604	0.587
50	0.535	0.532	0.551	0.569	0.561	0.512	0.623	0.609
52	0.558	0.554	0.572	0.569	0.561	0.535	0.623	0.630
54	0.558	0.554	0.592	0.588	0.561	0.535	0.642	0.630
56	0.581	0.575	0.592	0.588	0.585	0.535	0.660	0.630
58	0.581	0.575	0.592	0.589	0.610	0.558	0.660	0.652
60	0.605	0.596	0.612	0.608	0.610	0.558	0.660	0.652
63	0.628	0.617	0.633	0.608	0.610	0.581	0.679	0.652
66	0.628	0.617	0.653	0.647	0.634	0.581	0.679	0.674
69	0.651	0.660	0.694	0.686	0.659	0.605	0.679	0.696
72	0.721	0.682	0.715	0.706	0.659	0.628	0.698	0.717
75	0.721	0.702	0.714	0.725	0.683	0.651	0.698	0.717
78	0.744	0.745	0.714	0.725	0.683	0.651	0.717	0.739
81	0.768	0.745	0.755	0.725	0.707	0.674	0.736	0.739
84	0.814	0.766	0.755	0.745	0.707	0.698	0.755	0.739
87	0.814	0.766	0.776	0.745	0.732	0.721	0.755	0.761
90	0.814	0.766	0.796	0.765	0.732	0.721	0.774	0.761
95	0.838	0.809	0.837	0.804	0.756	0.721	0.792	0.761
100	0.860	0.830	0.898	0.883	0.756	0.744	0.792	0.783
105	0.884	0.830	0.918	0.902	0.780	0.767	0.812	0.783
110	0.884	0.872	0.939	0.902	0.780	0.767	0.830	0.783
115	0.907	0.894	0.939	0.922	0.805	0.791	0.849	0.783
120	0.907	0.894	0.939	0.941	0.829	0.791	0.868	0.805
125	0.930	0.915	0.959	0.961	0.854	0.814	0.868	0.804
130	0.931	0.915	0.959	0.981	0.878	0.837	0.887	0.826
135	0.954	0.936	0.959	0.981	0.902	0.860	0.906	0.848
140	0.977	0.936	0.980	0.981	0.927	0.884	0.925	0.870
145	0.977	0.936	0.980	1.000	0.951	0.907	0.943	0.870
150	0.977	0.957	0.980	1.000	0.976	0.907	0.962	0.891
155	0.977	0.957	1.000	1.000	1.000	0.930	0.981	0.913
160	1.000	0.979	1.000	1.000	1.000	0.953	1.000	0.935
165	1.000	0.979	1.000	1.000	1.000	0.977	1.000	0.957
170	1.000	0.979	1.000	1.000	1.000	0.977	1.000	0.978
175	1.000	1.000	1.000	1.000	1.000	1.000	1.000	1.000
180	1.000	1.000	1.000	1.000	1.000	1.000	1.000	1.000

	Test3_500	Test3_500	Test3_500	Test3_500
	LEFT	LEFT	RIGHT	RIGHT
Time (s)	LV/LVM	LH/LHM	LV/LVM	LH/LHM
0	0.000	0.000	0.000	0.000
1	0.026	0.027	0.164	0.139

2	0.211	0.189	0.260	0.194
3	0.211	0.216	0.290	0.222
4	0.237	0.243	0.322	0.222
5	0.316	0.270	0.322	0.250
6	0.342	0.297	0.355	0.250
7	0.342	0.297	0.355	0.278
8	0.344	0.324	0.387	0.305
9	0.368	0.324	0.387	0.305
10	0.368	0.351	0.419	0.305
11	0.395	0.351	0.419	0.333
12	0.395	0.351	0.419	0.333
13	0.395	0.378	0.451	0.333
14	0.421	0.378	0.451	0.361
15	0.421	0.378	0.451	0.361
16	0.421	0.378	0.484	0.389
17	0.421	0.378	0.484	0.389
18	0.421	0.405	0.484	0.389
19	0.421	0.405	0.516	0.417
20	0.447	0.405	0.516	0.417
21	0.447	0.405	0.516	0.417
22	0.447	0.405	0.548	0.444
23	0.447	0.432	0.548	0.444
24	0.447	0.432	0.548	0.444
25	0.474	0.432	0.548	0.444
26	0.474	0.432	0.548	0.444
27	0.474	0.432	0.548	0.472
28	0.500	0.459	0.580	0.472
29	0.500	0.459	0.580	0.500
30	0.500	0.459	0.580	0.500
32	0.500	0.486	0.580	0.500
34	0.526	0.486	0.613	0.528
36	0.526	0.514	0.613	0.528
38	0.526	0.514	0.645	0.555
40	0.526	0.541	0.645	0.555
42	0.553	0.568	0.645	0.584
44	0.579	0.595	0.677	0.584
46	0.579	0.595	0.677	0.584
48	0.605	0.595	0.677	0.584
50	0.605	0.595	0.677	0.611
52	0.632	0.622	0.709	0.612
54	0.632	0.622	0.709	0.612

56	0.632	0.622	0.742	0.639
58	0.658	0.622	0.742	0.666
60	0.658	0.622	0.742	0.694
63	0.684	0.622	0.774	0.694
66	0.684	0.622	0.806	0.694
69	0.684	0.622	0.806	0.694
72	0.711	0.622	0.806	0.722
75	0.711	0.649	0.806	0.722
78	0.711	0.649	0.839	0.750
81	0.737	0.649	0.838	0.777
84	0.737	0.649	0.838	0.777
87	0.737	0.649	0.838	0.777
90	0.737	0.649	0.871	0.805
95	0.763	0.676	0.903	0.833
100	0.763	0.703	0.903	0.833
105	0.789	0.703	0.935	0.861
110	0.789	0.730	0.935	0.889
115	0.789	0.757	0.967	0.889
120	0.816	0.788	0.967	0.916
125	0.816	0.811	0.967	0.917
130	0.843	0.838	0.967	0.944
135	0.869	0.865	0.967	0.944
140	0.895	0.892	1.000	0.972
145	0.921	0.919	1.000	0.972
150	0.947	0.946	1.000	0.972
155	0.974	0.973	1.000	0.972
160	1.000	1.000	1.000	0.972
165	1.000	1.000	1.000	0.972
170	1.000	1.000	1.000	1.000
175	1.000	1.000	1.000	1.000
180	1.000	1.000	1.000	1.000

REFERENCES

1. E.A. Starke Jr., J.T. Staley, Application of modern aluminum alloys to aircraft, Progress in Aerospace Science, Vol. 32, Issue 2-3, pp. 131-172, 1996.
2. R.K. Shah, D.P. Sekulic, Fundamentals of Heat Exchanger Design, Wiley, New York, 2003.
3. D.P. Sekulic, Wetting and Spreading Of Liquid Metals Through Open Microgrooves and Surface Alterations, Heat Transfer Engineering, Vol. 32, Issue 7-8, pp. 648-657, 2011.
4. P.G. De Gennes, Wetting: statics and dynamics. Reviews of Modern Physics, Vol. 57, No. 3, pp. 827-863.
5. D. Bonn; J. Egger; J. Indekeu; J. Meunier and E. Rolley, Wetting and spreading, Review of Modern Physics, Vol. 81, pp. 739-805, 2009.
6. E.W. Washburn, The dynamics of capillary flow, Physical Review, Vol. 17, pp. 273-283, 1921.
7. W. Liu and D.P. Sekulic, Capillary Driven Molten Metal Flow over Topographically Complex Substrates, Langmuir, Vol. 27, pp. 6720-6730, 2011.
8. W. Liu, Y. Li, Y. Cai and D.P. Sekulic, Capillary Rise of Liquids over a Microstructured Solid Surface, Langmuir, Vol. 27, pp. 14260-14266, 2011.
9. C-N. Yu, D. Hawksworth, W. Liu, and D.P. Sekulic, Al Brazing Under Severe Alternations of the Background Atmosphere: A New vs. Traditional Brazing Sheet, 5th International Brazing and Soldering Conference, April, 2012
10. J. Bico, C. Tordeux, D. Quere, Rough wetting, Europhys Lett., Vol.55, pp.214-220, 2001.
11. K.M. Hay, M.I. Dragila, J. Liburdy, Theoretical model for the wetting of rough surface, J. Colloid Interface Sci, Vol.325, pp.472-477, 2008.
12. C. Ishino, M. Reyssat, E. Reyssat, K. Okumura, D. Quere, Wicking within forests of micropillars, Europhys. Lett. 79, 56005, 2007.

13. Y.K. Chen, L.S. Melvin, S. Rodriguez, D. Bell, M.M. Weislogel, Capillary driven flow in micro scale surface structure, Microelectron. Eng. Vol.86, pp.1317-1320, 2009.
14. G.W. Gokel, J.A. Dean, Deans Handbook of Organic Chemistry, 2nd ed,; McGraw-Hill: New York, 2004.
15. F. Delannay, L. Froyen, A. Deruyttere, The wetting of solids by molten metals and its relation to the preparation of metal-matrix composite, J Mater Sci, Vol.22, pp.1-16, 1987.
16. E. Saiz, A.P. Tomisa, N. Rauch, C. Schen, M. Ruchle, M. Benassine, D. Seveno, J. de Conink, S. Lopez-Esteban, Nonreactive spreading at high temperature, Molten metals and oxides on molybdenum, Phys. Rev. E, 76, 041602, 2007.
17. H. Zhao, H. Wang, D.P. Sekulic, Y. Qian, Spreading Kinetics of Liquid Solders over an intermetallic solid surface, Part 1., J. Electron. Mater, Vol.38, pp.1838-1845, 2009a.
18. A.L. Biance, C. Clanet, D. Quere, First steps in the spreading of a liquid droplet. Phy. Rev. E, 69, 016301, 2004.
19. D. Seveno, A. Vaillant, R. Rioboo, H. Adao, J. Conti & J. De Coninck, Dynamics of wetting revisited. Langmuir, *25*(22), 13034-13044, 2009.
20. A. Bejan, Convection Heat Transfer, John Wiley & Sons: New York, 2004.
21. Flow through Porous Media, American Chemical Society: Washington, DC, 1970.
22. D.P. Sekulic, Scaling of Molten Metal Brazing Phenomena: Prolegomena for Model Formulation, Progress in Scale Modeling, pp. 391-402, 2008.
23. P. Ehrhard, & S.H. Davis, Non-isothermal spreading of liquid drops on horizontal plates. Journal of Fluid Mechanics, *229*(1), 365-388, 1991.
24. F. Delannay, L. Froyen, A. Deruyttere, The wetting of solids by molten metals and its relation to the preparation of metal-matrix composite, J Mater Sci, Vol.22, pp.1-16, 1987.
25. N. Eustathopoulos, MG. Nicholas, B. Drevet, Wettability at high-temperature, Amsterdam, New York, Pergamon, 1999.

26. RE. Loehman, AP. Tomsia, Joining of ceramics, Am Ceram Soc Bull, Vol.67, pp.375-380, 1988.
27. E. Saiz, A.P. Tomsia, Kinetics of high-temperature spreading, Current Opinion in Solid State and Materials Science, Vol.9, pp.167-173, 2005.
28. H.W. Swidersky, Aluminium brazing with non-corrosive fluxes-state of the art and trends in NOCOLOK® flux technology. *DVS BERICHTE*, *212*, 164-169, 2001.
29. R.L. Peaslee, Brazing Footprints – Case Studies in High-Temperature Brazing, Wall Colmonoy Corporation, Madison Heights, Michigan, 2003.
30. M.M. Schwartz, Fundamental of brazing, Welding, Brazing, and Soldering, ASM Handbook, Metals Park, OH: ASM International, 1993.
31. G. Humpston and D.M. Jacobson, Principles of Soldering and Brazing, Metals Park, OH: ASM International, 1993.
32. B.P. Zellmer, N. Nigro, D.P. Sekulic, Numerical modeling and experimental verification of the formation of 2D and 3D brazed joints, Modelling Simul. Mater. Sci. Eng., 9, 339-355, 2001.
33. D.P. Sekulic, B.P. Zellmer, N. Nigro, Influence of joint topology on the formation of brazed joints, Modelling Simul. Mater. Sci. Eng., 9, 357-369, 2001.
34. N.J. Nigro, S.M. Heinrich, A.F.Elkouh, X. Zhou, R. Fournelle, P.S. Lee, J. Electron. Packaging, Vol.115, pp.141, 1993.
35. R. Hooke & T.A. Jeeves, Solution of Numerical and Statistical Problems. Journal of the ACM (JACM), *8*(2), 212-229, 1961.
36. D.P. Sekulic, F. Gao, H. Zhao, B. Zellmer and Y.Y. Qian, Prediction of the Fillet Mass and Topology of Aluminum Brazed Joints, Welding Journal – Welding Research Supplement, vol. 83(3): 102s – 110s.
37. D.P. Sekulic, A.T. Male, C. Pan and F. Gao, Modeling of molten clad flow and diffusion of Si across a clad-core interface of an aluminum brazing sheet, DVS – Berichte, Vol. 212, pp.204-209.

38. R.J. Braun, B.T. Murray, W.J. Boettinger and G.B. McFadden, Lubrication theory for reactive spreading of a thin drop, Phys. Fluids, Vol.7, Issue. 8, pp.1797-1809, 1995.
39. F. Gao, D.P. Sekulic, Y.Y. Qian, X. Ma, Residual clad formation and aluminum brazed joint topology prediction, Materials Letters, Vol. 57, pp. 4592-4596, 2003.
40. G.J., Marshall, R.K., Bolingbroke & A. Gray, Microstructural control in an aluminum core alloy for brazing sheet applications. Metallurgical and Materials Transactions A, *24*(9), 1935-1942, 1993.
41. D.P. Sekulic, in: Proceedings of the International Conference on Heat Exchangers for Sustainable Development, IST, Lisbon, pp. 377, 1998.
42. D.P. Sekulic, Molten aluminum equilibrium membrane formed during controlled atmosphere brazing, International Journal of Engineering Science, Vol. 39, pp.229-241, 2001.
43. Aluminum brazing handbook. 3rd ed. Washington (DC): Aluminum Association; 1979.
44. J. Lacaze, S. Tierce, M.C. Lafont, Y. Thebault, N. Pébère, G. Mankowski & D. Daloz, Study of the microstructure resulting from brazed aluminium materials used in heat exchangers. Materials Science and Engineering: *A*, *413*, 317-321, 2005.
45. W.S., Miller, L. Zhuang, J. Bottema, A. Wittebrood, P. De Smet, A. Haszler & A. Vieregge, Recent development in aluminium alloys for the automotive industry. Materials Science and Engineering: *A*, *280*(1), 37-49, 2000.
46. A. Wittebrood, C.J. Kooij, & K. Vieregge, Grain boundary melting or liquid film migration in brazing sheet. In Materials science forum, Vol. 331, pp. 1743-1750, 2002.
47. D.M. Turriff, S.F. Corbin, M. Kozdras, Diffusional solidification phenomena in clad aluminum automotive braze sheet, Acta Materialia, Vol. 58, pp. 1332-1341.
48. H. Zhao, D.P. Sekulic, Diffusion-controlled melting and re-solidification of metal micro layers on a reactive substrate, Heat Mass Transfer, Vol. 42, pp.464-469, 2006.

49. J.R. Terrill, Diffusion of silicon in aluminum brazing sheet, Welding J Res Suppl, Vol. 45, Issue 5, pp.202-S-209-S.
50. F. Gao, H. Zhao, D.P. Sekulic, Y. Qian, L. Walker, Solid state Si diffusion and joint formation involving aluminum brazing sheet, Materials Science and Engineering A, Vol.337, pp.228-235, 2002.
51. http://www.dataphysics.de//?cat_id=267
52. F.P. Incropera, D.P. DeWitt, Appendix A, Table A.3, Heat and Mass Transfer, Fifth Edition
53. http://www.makeitfrom.com/material-data/?for=96-Percent-Purity-Alumina
54. Chapter 1, Trace Oxygen Analyzer Operation Menu, Teledyne Analytical Instruments.
55. http://s3.amazonaws.com/purityplus/catalog_items/4/attachment/puregases_air.pdf, PurityPlus Specialty Gases, Air
56. American Limits of Error ASTM E230-ANSI MC 96.1.
57. Typical OMEGACLAD XL Type K Performance, http://www.omega.com/ppt/pptsc.asp?ref=KMQXL_NMQXL
58. http://www.virtualdub.org/
59. http://www.mediacy.com/index.aspx?page=Image_Pro_Software&gclid=CO62rdjm7bUCFY6e4AodiEwAeA
60. R.B. Abernethy, R.P. Benedict & R.B. Dowdell, ASME measurement uncertainty. Journal of Fluids Engineering, *107*(2), 161-163, 1985.
61. http://www.originlab.com/index.aspx?go=Products/OriginPro
62. D.P. Sekulic, P.K. Galenko, M.D. Krivilyov, L. Walker, F. Gao, Dendritic growth in Al-Si alloys during brazing. Part 1: Experimental evidence and kinetics, International Journal of Heat and Mass Transfer, Vol. 48, 2005, pp. 2372-2384.
63. C-N. Yu, Personal Communication, March, 2013.
64. H. Fu, Personal Communication, March, 2013.

65. C-N. Yu, 2013, Joint Formation under Severely Altered Background Atmosphere in Controlled Atmosphere Brazing of Aluminum, MS Thesis, University of Kentucky.

VITA

Name

Fangxiao Dong

Place of Birth

Shanghai, China

Education

B.E. in Thermal and Power Engineering (09/2003 – 07/2007), Shanghai University of Electric Power, Shanghai, China

Experience

- Research and Teaching Assistant (08/2010 – 05/2013), Brazing Laboratory, Institute for Sustainable Manufacturing, Department of Mechanical Engineering, University of Kentucky

Publications

H. Fu, F. Dong, D.P. Sekulic, S.Dj. Mesarovic, M. Krivilyov. "Surface Tension Driven Kinetics of the Triple Line of a Liquid Metal Free Surface", IMECE2013, November 13-21, San Diego, California, USA, 2013 (Submitted)